FAIR- TAC: Keyword Super-FRS

Technical Report on the Design, Construction, Commissioning and Operation of the Super-FRS of FAIR

NUSTAR Collaboration

www.gsi.de/nustar

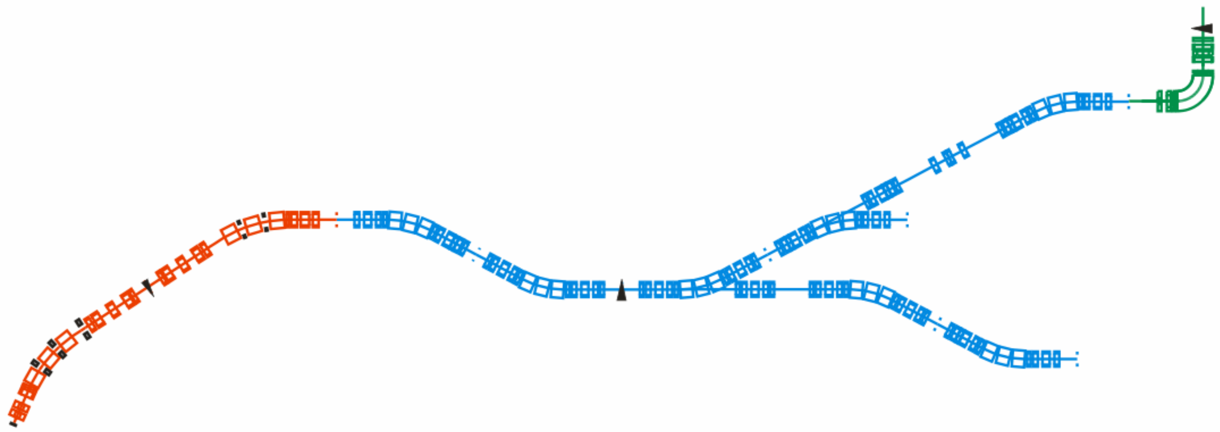

The following colleagues have contributed to this report:

H. Geissel, M. Winkler, H. Weick, K.-H. Behr, G. Münzenberg, H. Simon, K. Sümmerer, B. Achenbach, L. Ahle, T. Aumann, A. Bleile, G. Breitenberger, A. Brünle, H. Emling, G. Fehrenbacher, M. Gleim, W. Hüller, H. Iwase, C. Karagiannis, R. Kaiser, A. Kelic, B. Kindler, G. Klappich, T. Kubo, N. Kurz, K. Kusaka, J. Lettry, B. Lommel, G. Moritz, D. Morrissey, C. Mühle, J. A. Nolen, I. Pschorn, T. Radon, R. Ronningen, G. Savard, C. Scheidenberger, Y. Shatunov, B.M. Sherrill, N.A. Tahir, M. Yavor, A. Yoshida, X. Yu, A.F. Zeller

FAIR- TAC: Keyword Super-FRS

Date: 4.02.2005

Technical Report on the Design, Construction, Commissioning and Operation of the Super-FRS of FAIR

Super-FRS / NUSTAR Collaboration, www.gsi.de/nustar

Spokesperson: H. Geissel, GSI, KP2, +49 6159 71 2740, H.Geissel@gsi.de

Deputy: M. Winkler, GSI, KP2, +49 6159 71 2468, M.Winkler@gsi.de

for the NUSTAR Collaboration

Table of Contents

1 Description of the Super-FRS project

Role in the FAIR Project, tasks and requirements

The Super-FRS will be the most powerful in-flight separator for exotic nuclei up to relativistic energies. Rare isotopes of all elements up to uranium can be produced and spatially separated within some hundred nanoseconds, thus very short-lived nuclei can be studied efficiently. The Super-FRS is a large-acceptance superconducting fragment separator with three branches serving different experimental areas including a new storage ring complex. The new rare-isotope facility is based on the experience and successful experimental program with the present FRS [1].

The Super-FRS magnetic system will consist of three branches connecting different experimental areas, see Figure 1. Reaction studies under complete kinematics, similar to the present ALADIN-LAND setup, will be performed at the High-Energy Branch. Unique studies will be performed in the Ring Branch consisting mainly of a collector ring CR, the NESR, RESR and an electron nucleon collider (eA). Precision experiments with a brilliant electron-cooled exotic beam including reaction studies with the atoms of an internal target will be done in the NESR. A novelty will be electron scattering from exotic nuclei in the eA collider section. The Low-Energy Branch of the Super-FRS is mainly dedicated to precision experiments with energy-bunched beams stopped in a gas cell. This branch is complementary to ISOL facilities since all elements and short-lived isotopes can be studied.

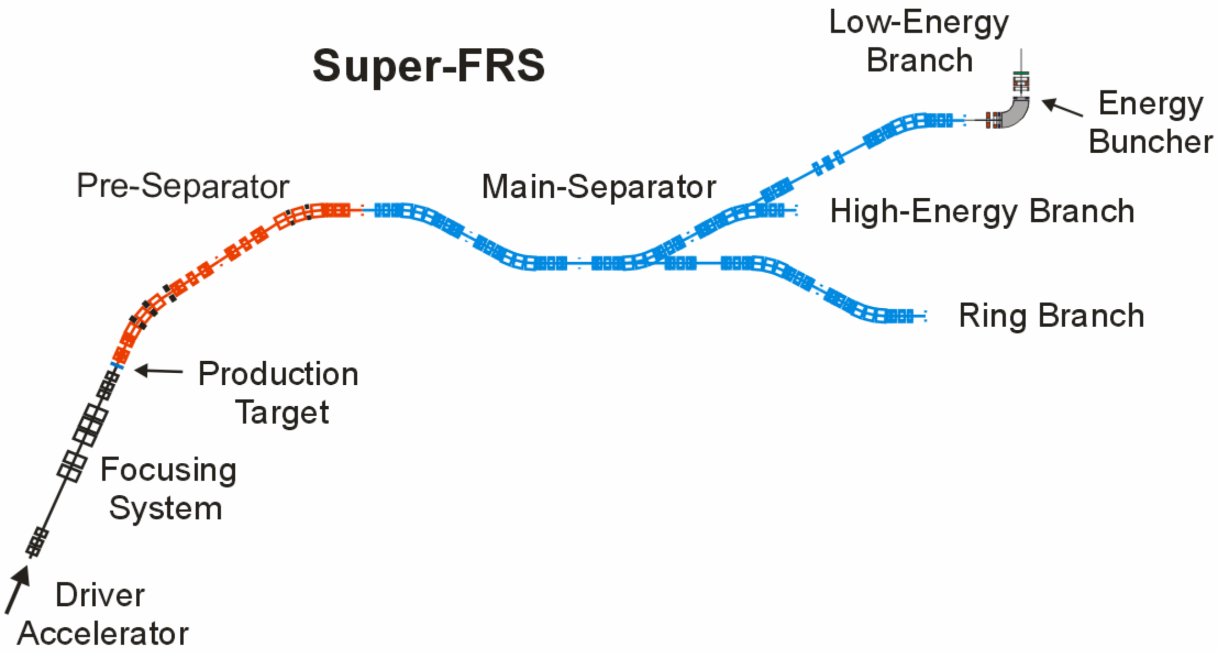

Figure 1: *Layout of the proposed superconducting fragment separator Super-FRS for the production, separation, and investigation of exotic nuclei. Spatially separated rare-isotope beams are delivered to the experimental areas via three different branches.*

Table 1 Parameters of the Super-FRS compared with the FRS.

Facility	Max. Magnetic Rigidity $B\rho_{max}$ / [Tm]	Momentum Acceptance $\Delta p/p$	Angular Acceptance		Momentum Resolution
			ϕ_y / [mrad]	ϕ_x / [mrad]	
FRS	18	±1 %	±7.5	±7.5	1500 ($\varepsilon=20\pi$ mm mrad)
Super-FRS	20	±2.5 %	±40	±20	1500 ($\varepsilon=40\pi$ mm mrad)

The layout of the Super-FRS consists of magnets with $B\rho_{max}$ of 20 Tm whereas the CR is restricted to 13 Tm and the energy buncher to 10 Tm. This follows from the consideration to be cost effective with the same type of magnetic elements throughout the separator and allows in addition to use a degrader at the final achromatic focal plane, an option which is successfully applied at the present FRS.

2 Technical Layout

Structure of the Super-FRS, description of work packages

The Super-FRS has to efficiently separate in-flight rare isotopes produced via projectile fragmentation of all primary beams up to ^{238}U and via fission of ^{238}U beams. The latter reaction is a prolific source of very neutron-rich nuclei of medium mass. However, due to the relatively large amount of kinetic energy released in the fission reaction, the products populate a large phase space and thus determine the need for a much larger acceptance for the Super-FRS compared with the FRS, see Table 1. The gain in transmission for uranium fission products at the Super-FRS is more than an order of magnitude compared to the FRS.

Besides the fragment intensities, the selectivity and sensitivity are crucial parameters that strongly influence the success of an experiment with very rare nuclei. A prerequisite for a clean isotopic separation is that the fragments have to be fully ionized to avoid cross contamination from different ionic charge states. Multiple separation stages are necessary to efficiently reduce the background from such contaminants. Based on the experience of successful spatial isotopic separation with the FRS, the Super-FRS also uses the $B\rho$-ΔE-$B\rho$ method, where a two-fold magnetic rigidity analysis is applied in front of and behind a specially shaped energy degrader. The strong enhancement of the primary beam intensity expected with the SIS100/300 synchrotron requires additional measures to achieve the required separation quality. A solution is an additional degrader stage which provides an effective pre-selection before the fragment beam impinges onto the main degrader. A straight forward consequence is that the Super-FRS consists of a two-stage magnetic system, the Pre- and the Main-Separator, each equipped with a degrader.

The condition mentioned above for fully stripped fragments requires a high-energy operating domain. On the other hand, the thicknesses of the production target and degraders have to be optimized to prevent substantial losses due to secondary nuclear reactions. The selection of the maximum magnetic rigidity of 20 Tm results from these physical criteria and the optimization of the performance and costs of the magnetic elements and their dynamic range.

2.1 Ion-optical layout

The ion-optical layout of the Super-FRS (High-Energy Branch) and its imaging conditions are presented in Figure 2. The envelopes and the dispersion line are plotted for primary-beam emittances of 40 π mm mrad and Δp/p of 2.5 %, respectively. The target spot size is assumed to be ±1 mm and ±2 mm in the x- and y-direction, respectively. The magnet system consists of the Pre-Separator and the Main-Separator, each equipped with an energy degrader stage. The pre- and Main-Separator are both achromatic systems, hence the complete system is also achromatic. This means the image size at the final focal plane is independent of the momentum spread of the fragments at the entrance of the system and thus guarantees the best spatial isotopic separation.

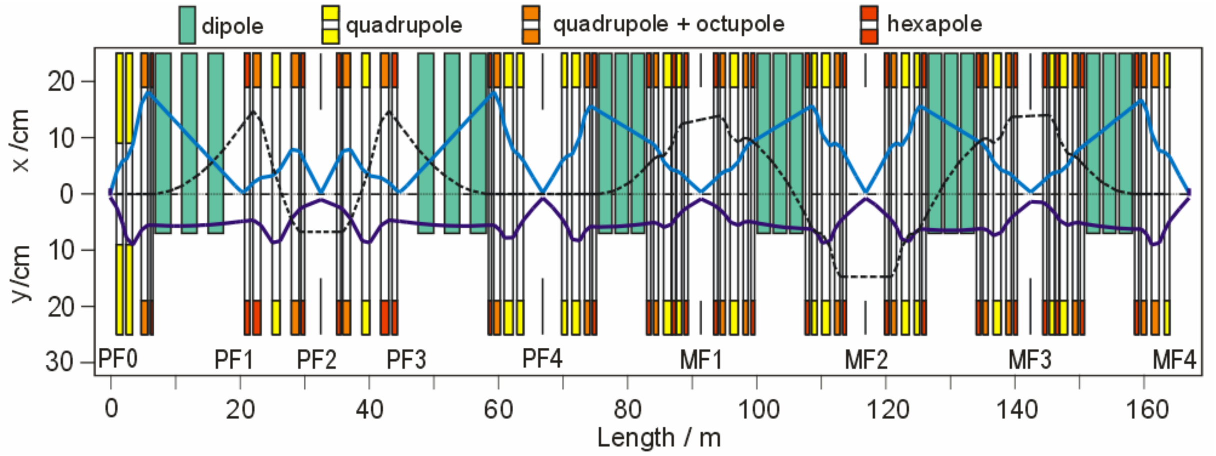

Figure 2: Ion-optical elements, beam envelopes (full lines) and the dispersion line for 2.5 % momentum deviation (dashed line) are shown in the lattice of the Super-FRS. Here the high-energy branch (HEB) is presented. The envelopes result from an emittance of 40 π mm mrad in x and y direction. The different focal planes of the Pre-Separator (P) and the Main-Separator (M) are indicated by (P,M)$F_1 – F_4$. Quadrupole triplets are placed in front of and behind the dipole magnets to achieve the desired ion-optical conditions at the focal planes and to properly illuminate the dipole magnets to achieve the required optical resolving power. Hexapole and octupole magnets are applied to correct image aberrations, especially at the degrader positions and the achromatic focal planes.

2.1.1 Beam parameters from SIS-18 / 100 / 300

The main parameters of the accelerators relevant for the Super-FRS are presented in Table 2. The values for the emittance and momentum spread correspond to two standard deviations.

Table 2: Accelerator Parameters

Driver Accelerator	$B\rho_{max}$ (Tm)	Reference Energy (MeV / u)	Emittance ε_h , ε_v (mm mrad)	Repetition Rate (s^{-1})	Momentum Spread	*Intensity* (*spill*$^{-1}$)
SIS 12	12	92	52(h) * 17(v)	4	$5 * 10^{-4}$	$2 * 10^{11}$
SIS 18	18	1000	13(h) * 4(v)	1	$5 * 10^{-4}$	$4 * 10^{10}$
SIS 100	100	1500	12(h) * 4(v)	fast extr.	$1 * 10^{-2}$	$1 * 10^{12}$
SIS 300	300	1000	3(h) * 4(v)	d.c.	$2 * 10^{-4}$	$1 * 10^{12}$

2.1.2 Ion optics from SIS to the production target

The ion-optical momentum resolution determines the separation power of the Super-FRS for the spatially separated fragment beams. Therefore, a small and constant beam spot at the target position is essential, typically 1 and 2 mm in x- and y-direction, respectively. Only an excellent achromatic focus corrected for higher-order aberration can fulfill this necessary condition at the entrance of the Super-FRS. The achromatic condition is especially indispensable for the fast extracted projectile beam which is characterized by the large momentum spread of 1%, which even exceeds for some fragments the spread due to the nuclear creation process.

This has two consequences:

- The magnetic system from the accelerator to the production target has to be an achromatic system corrected with higher-order multipole fields.
- A special focusing system subsequent to the achromate will be applied to reach the required spot size at the production target.

The achromatic beam transport is described in a separate report (S. Ratschow et al.). Presently, there are two ion-optical options for the fine-focusing system positioned directly in front of the target area. A layout of a split-lens optics for low (10Tm) and high (100 Tm) magnetic rigidities is presented in Figure 3. The focusing system must handle the beam from SIS-100/300 or from SIS-18. The quadrupole lenses in the multiplet are split into several parts corresponding to the operating domain. This option has the advantage to apply the super-ferric magnet type as suggested for the Super-FRS. The magnetic system is characterized by a length of 25m. Operating experience for this type of magnets exists in several laboratories. A more compact system can be used if quadrupole magnets of the cos(2θ)-type are applied, see Figure 4. This system would be 10m shorter and more versatile over a large Bρ-range. Although this option requires a new magnet research and development program it can be applied also for other experimental areas, e.g. for the setup of plasma research, within the FAIR project (synergetics).

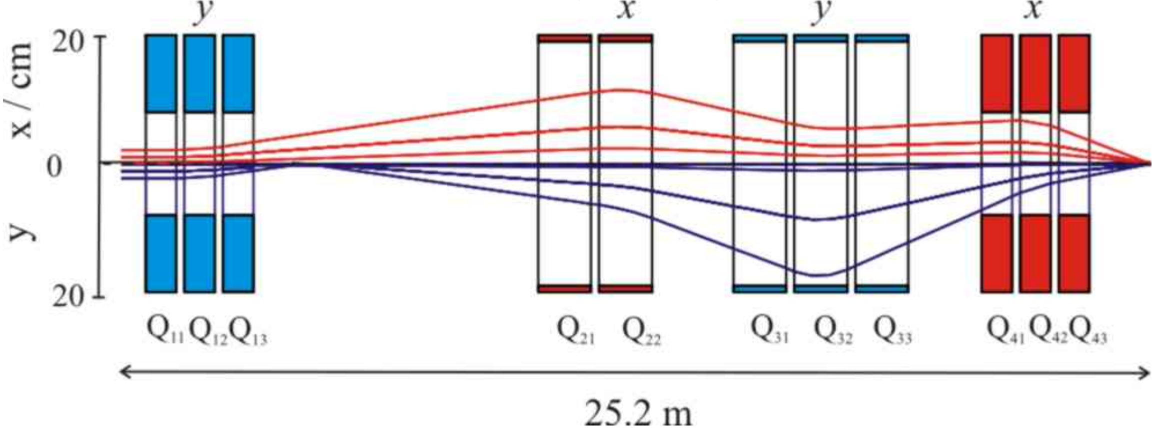

Figure 3: Ion-optical layout of the split-quadrupole fine-focusing system to be positioned directly in front of the production target. The operating range is determined by the option that projectile beams from SIS-18 or SIS-100/300 are applied for experiments at the Super-FRS.

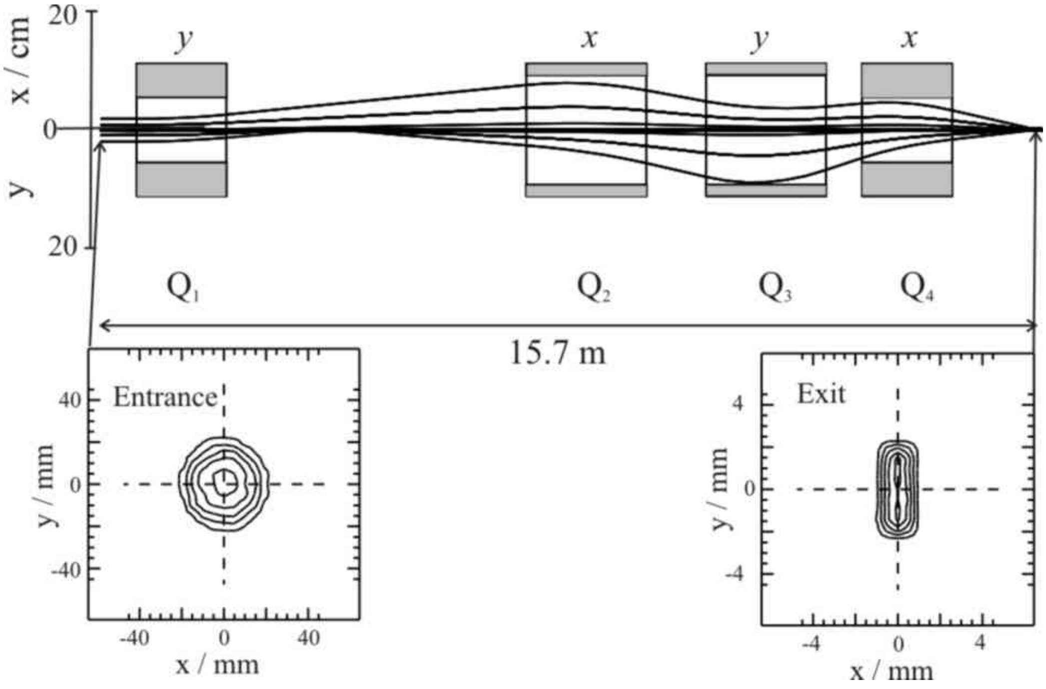

Figure 4: Ion-optical layout of the fine-focusing system using superconducting cos(2θ)-type quadrupole lenses. An example of the calculated focusing result is presented in the lower part of the ion-optical plot. Note that the scale on right hand axis is reduced by a factor 10.

2.1.3 Pre-Separator

In order to access the most neutron-rich nuclei created via fission a high-energy separator with substantially increased acceptance, compared to the FRS, is required. The design of the Super-FRS has been based upon this criterion. In Table 1, the main parameters of the FRS and the Super-FRS are compared. The phase-space acceptance of the Super-FRS has been substantially increased by means of larger apertures and fields in the magnets. Besides the technical layout of the production target, the separation and dump of the primary beam are major technical challenges to be solved in the Pre-Separator. The projectile beam emerging from the production target has to be separated from the selected fragments and dumped in a special catcher system, see dedicated section in this report. One major requirement is that the high-intensity primary beam should not impinge on the first degrader to maintain the high-quality separation power of the two achromatic degrader stages. Keeping in mind that the intensity and such the energy deposition of the primary beam is about two orders of magnitude larger than the fragments the conditions and properties for the material and the high radiation field require special considerations implemented in the optical layout.

This means the technical realization of the target and beam dump areas requires some modifications of the ion-optical layout of the Pre-Separator compared to the earlier description of the Super-FRS in reference [2]:

The dipole magnets have been divided into three 11-degree parts. The space in between these different dipole magnets (1.7 m) accommodates position-sensitive detectors and primary beam catchers, i.e. the primary beam will not be dumped inside any magnet but only in localized external beam catchers (dumps). An extra dispersive focus is required directly behind the first dipole magnet system, i.e. in total the Pre-Separator has 3 dispersive focal planes to form an overall achromatic system.

The division into three parts of the previously 6 m long dipole magnets gives also advantages for the technical production which certainly reduces the costs of the magnets. The 6 beam catchers positioned on both sides of the optical axis will stop the primary beam completely. In the target and in these beam catchers the primary beam will be slowed down by atomic interaction and will be partially converted into heavier fragments and light particles, like protons and neutrons which will even penetrate through the 1 m thick material used for the beam catchers. Therefore, one has in principle to consider if the superconducting magnets right after an interaction zone (target, beam catcher) can survive the high radiation field and how much temperature rise is acceptable to avoid quenching of a superconducting magnet. From detailed Monte Carlo simulations using the PHITS code [31] we can conclude that in principle all superconducting magnets stay below the quench limit. However, due to high radiation load the cryogenic power exceeds the practical limits. Taken this into account and to have a long term save and reliable operation we consider presently the option that the first quadrupole and dipole magnets including the hexapole magnet directly behind the focal plane PF1 are produced as normal conducting systems with radiation-hard insulation. The Pre-Separator is presently designed and optimized such that we can select both, the normal or superconducting options.

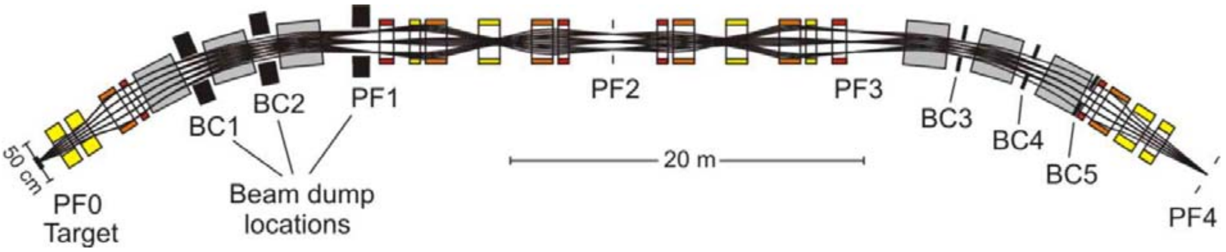

Figure 5: Layout of the Pre-Separator. The focal planes (PF1-PF4) and beam dump position (BC1-BC5) are indicated. Note that also at PF1a beam dump system will be installed.

The standard ion-optical layout of the Pre-Separator is presented in Figure 5. The most relevant first order matrix elements are given in Table 3**.** In the first focal plane only in x-direction a focus is realized whereas in the symmetrical mid plane, the position of the first degrader system, in both coordinates foci are required and a parallel dispersion line. The system is mirror symmetric with respect to PF2, firstly to have the necessary three foci to achieve the achromatic condition at PF4, secondly to minimize the geometrical image aberrations. Furthermore, one has to consider the case that a relatively high intensity component of the primary beam, for example uranium ions in the Li-like charge state impinge on the degrader. This contamination can then be removed in the corresponding slit system mounted within the second dipole magnet system of the Pre-Separator.

Table 3: *Calculated first-order transfer matrix elements at the focal planes PF1-PF4. The linear dimensions x and y are given in m, a and b in rad and the momentum deviation δ in parts of the nominal value.*

Matrix element	PF1	PF2	PF3	PF4
(x,x)	-3.19	1.74	-3.19	*2.00*
(x,a)	0	0	0	*0*
(x,δ)	4.78	-2.61	4.78	*0*
(a,a)	-0.31	0.57	-0.31	*0.5*
(a,δ)	0.58	0	-0.58	*0*
(y,y)	-4.81	-3.00	0.55	*1.54*
(y,b)	2.14	0	-2.19	*0*
(b,b)	-0.07	-0.33	-0.06	*0.65*
drift length	3.3	5.0	3.3	*6.0*

The drift lengths between the magnetic elements and particular at the focal planes are taking into account the technical layout of the magnet system and accommodate the diagnostic elements.

The benefit of the design is that the higher-order aberrations are small except for the chromatic contributions, especially (x,aδ) which is responsible for an enormous focal plane tilt. The tilt angle at PF2 would be about 7 degrees (required are 90 degrees) without second-order corrections by means of hexapole magnets. Such a tilt would make a high-resolution degrader operation very difficult or even impossible. Therefore, hexapole magnets are used to correct this deficiency. However, soon as this correction is done, induced higher-order aberrations become a major challenge. Our procedure is to find an optimal position for the hexapoles where the required field strengths are minimal by means of calculated hexapole coupling coefficients along the separator. It is a necessary condition that the induced aberrations are small. This procedure was also successfully applied at the present FRS and is based on suggestions by K. Brown [3] some decades ago. An example, of such a system of coupling coefficients is given in Figure 6**.** Applying hexapole and octupole corrections we succeeded to regain about 80% of the first-order momentum resolving power at the central plane of the Pre-Separator.

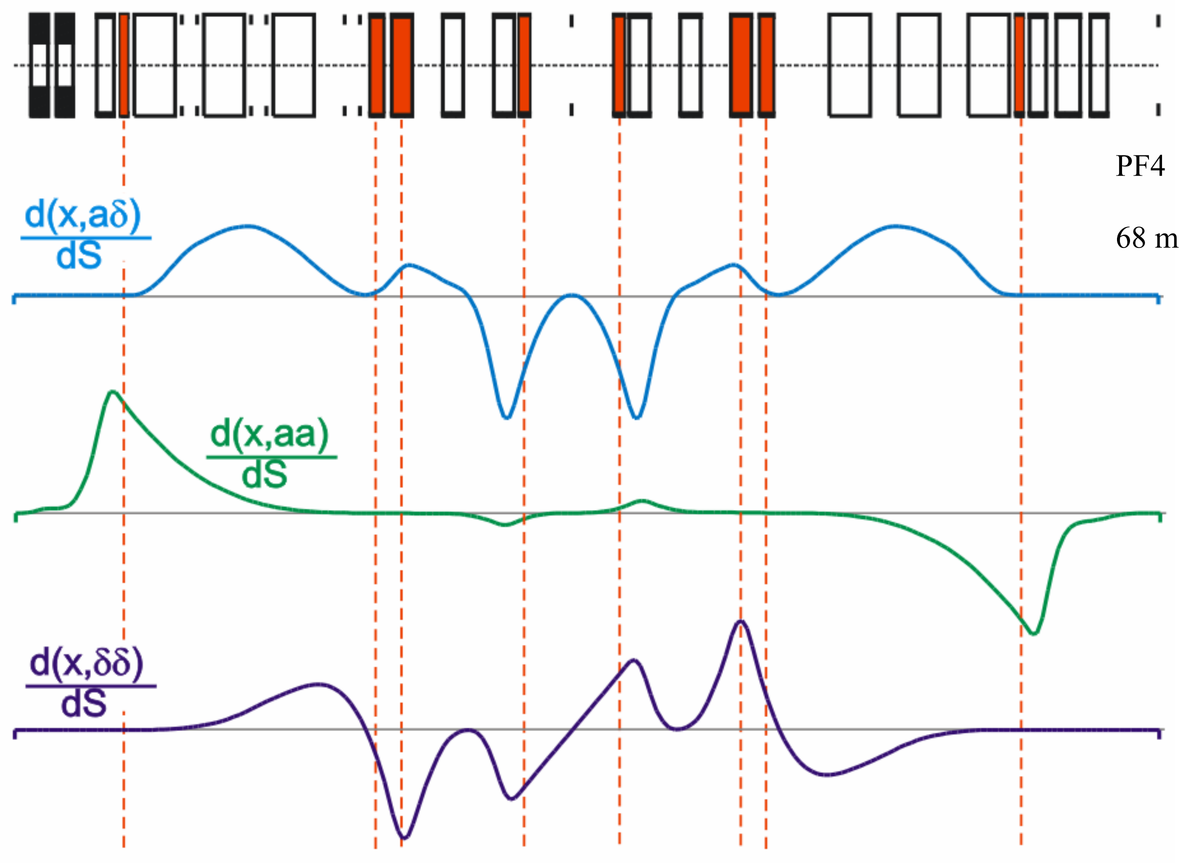

Figure 6: Example of important hexapole coupling coefficients (x,aa, x,aδ, x,δδ) calculated along the Pre-Separator. The magnetic elements of the Pre-Separator are schematically shown in the upper part of the plot. The hexapole magnets are marked in red colour.

The additional foci at PF1 and PF3 can of course be shifted more towards the middle of the drift lengths between the subsequent dipole and hexapole magnets to improve the spatial separation of the primary beam and the selected fragments. However, this would reduce the optical resolving power at PF2 for the overall fragment separation power. In case, the magnetic rigidity difference between the primary beam and the fragments is very large, such that the first two beam catchers are doing the job, the Pre-Separator can also be operated with one intermediate focal plane only. In principle, one can achieve with this mode the highest resolution due to the larger illumination of the field volume in the dipole magnets and the easier correction of the image aberration.

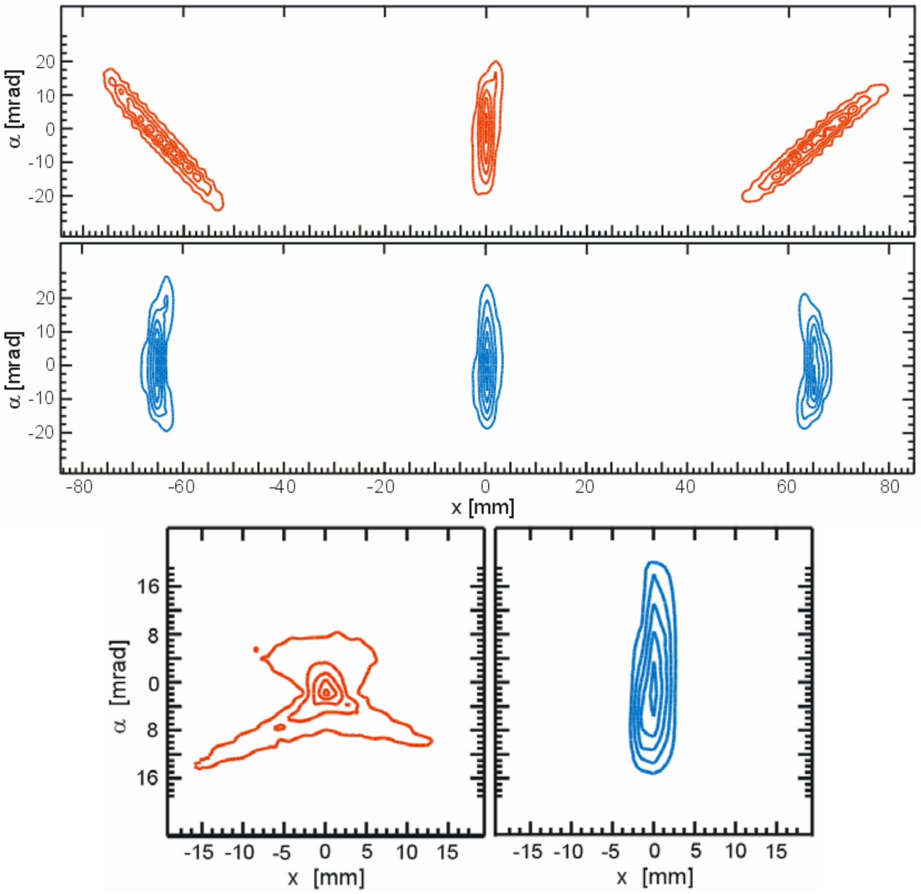

Figure 7 Upper pannel: Calculated phase space in the dispersive focal plane PF2 for a beam of 40 mm mrad and three different momenta of Δp/p= ±2.5% with (blue distributions) and without (red distributions) correction of image aberrations. Lower panel: Corresponding phase space in the achromatic focal plane PF4.

2.1.4 Main-Separator

The Main-Separator consists of 4 dipole stages with focusing elements in front and behind each dipole magnet system. The 28-degree dipole magnets are divided in 3 parts to facilitate the production of the iron-dominated superconducting magnets. The ion-optical design of the Main-Separator closely follows the concept applied for the Pre-Separator. However, the radiation level in this part of the Super-FRS is about two orders of magnitude lower because the primary beam and the non-desired fragments are deposited in the Pre-Separator. The Main-Separator has also 4 focal planes to accommodate an achromatic system with a degrader station in the central focal plane. The Main-Separator has 3 experimental branches to different experimental areas.

Modifications of the ion-optical layout of the Main-Separator compared to the earlier description of the Super-FRS in reference [2]:

- The dipole magnets have been divided into three 9.3-degree parts,
- external hexapole magnets,
- all quadrupole magnets have the same apertures

The characteristic features are outlined for the example of the high-energy branch. This branch has the advantage of a symmetrical geometry and therefore the potential for the highest ion-optical resolution and transmission. The most relevant ion-optical properties can be deduced from the first-order ion-optical matrix elements presented in Table 4.

Table 4: First-order matrix elements of the Main-Separator. The linear dimensions for x and y are in m, the angles a and b in rad and the momentum deviation in parts of the nominal value (δ).

Matrix Element	MF1	MF2	MF3	MF4
(x,x)	-3.33	1.86	-3.50	1.80
(x,a)	0	0	0	0
(x,δ)	5.10	-5.70	5.36	0
(a,a)	-0.30	0.54	-0.29	0.56
(a,δ)	0.09	0	0.02	0
(y,y)	-2.50	1.98	-3.32	1.51
(y,b)	0	0	0.34	0
(b,b)	-0.4	0.50	-0.45	0.66
drift length	4.0	6.0	4.0	6.0

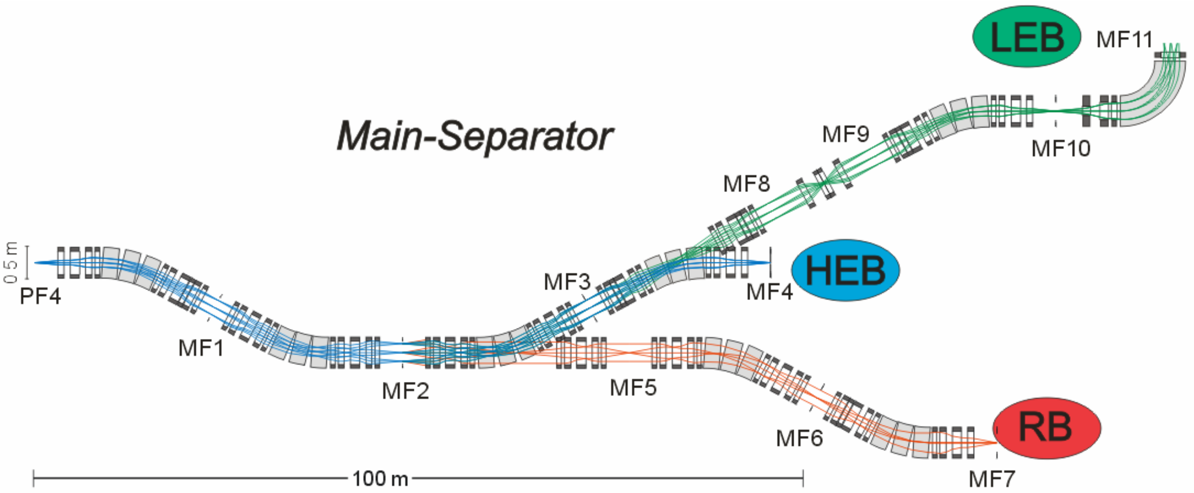

Figure 8: System plot of the Main-Separator with its branches to the different experimental areas. (LEB: Low-Energy Branch, HEB: High-Energy Branch, RB: Ring Branch). The different focal planes along the magnet system are indicated (MF1-MF11).

Separation performance with two degrader stages

The two-stage system has several novel functions and features:

- reduction of the contaminants from fragments produced in the first degrader;
- optimization of the fragment rate on the detectors in the Main-Separator;
- introduction of another separation cut in the A-Z plane of the separated isotopes; and
- Pre- and Main-Separator can ideally be used for secondary reaction studies if the separation of the Pre-Separator is already sufficient.

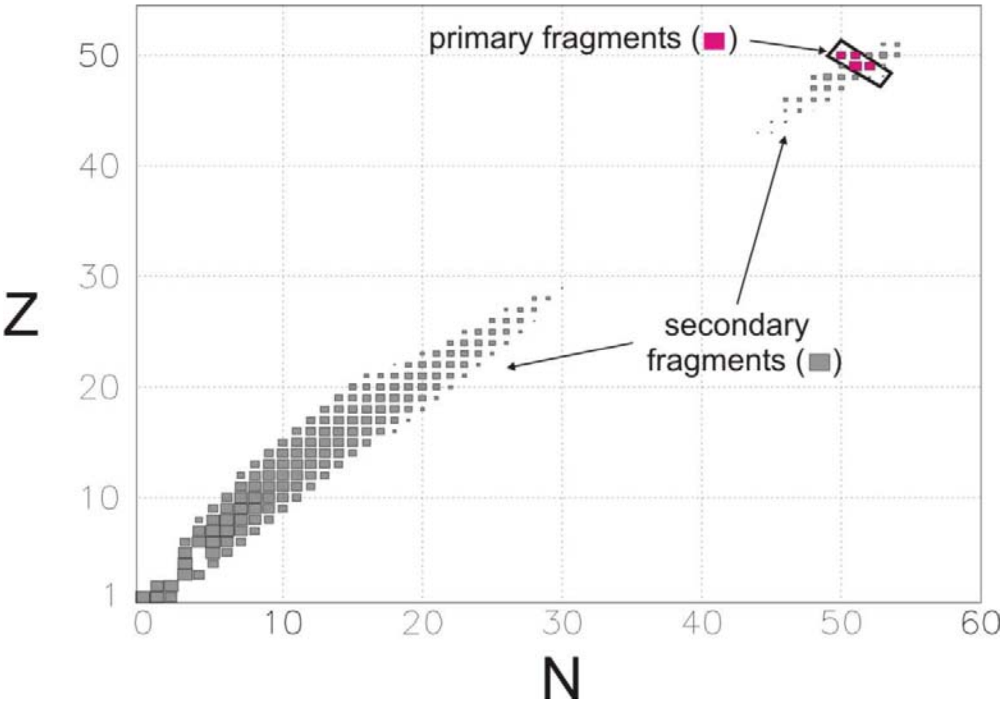

Figure 9: Separation performance of the two-degrader method compared with a one-degrader setup, ^{100}Sn example, taken from ref[2].

The example shows the separation of ^{100}Sn produced by fragmentation of ^{124}Xe at 1000 MeV/u. The large number of secondary fragments for a single degrader stage is illustrated by using the Main-Separator only (open boxes). The total amount of secondary fragments exceeds the separated ^{100}Sn rate by a factor of 10^4. In case the Pre-Separator is used in addition, only the few primary fragments, marked with red boxes, are transported to the final focal plane.

The resulting Super-FRS system will be a powerful isotope separator and in addition a **versatile high-resolution spectrometer**. This operation mode has been very successfully applied also in several categories of experiments at the present FRS [1]. Several basic discoveries have been made with the FRS as spectrometer, e.g., new halo properties, deeply pionic states in heavy atoms, relation of fragmentation and EOS, new atomic collision properties at relativistic energies etc.. Such achromatic systems are ideally suited for high-resolution studies independent of possible energy fluctuations of the primary beam.

2.1.4.1 Coupling to the high-energy experimental area

The high-energy branch allows experiments with fast secondary beams up to $B\rho_{max}$ of 20 Tm. It combines the in-flight separator with an efficient reaction setup, see Figure 2 and Figure 8. The compact setup will overcome the problem of low transmission of the present FRS to the experimental areas caused by long transport lines of more than 100 m and beam-line magnets designed only for primary beams with small emittances.

2.1.4.2 Coupling to the storage rings

Of special importance is the ring branch which consists of a storage-cooler ring system. Fragment pulses as short as 50 ns are injected into the collector ring CR with rigidities of up to 13 Tm. The main task of the CR is to efficiently collect and stochastically precool the hot fragment beams.

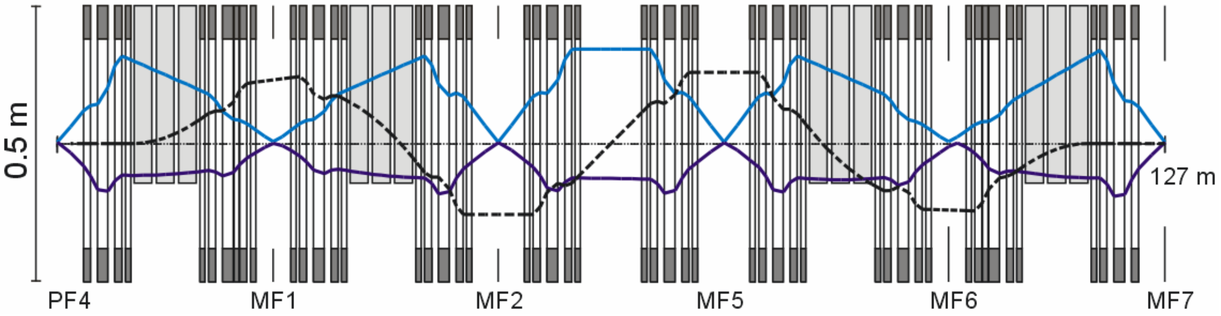

Figure 10: Ion optical layout of the Ring-Branch. Shown are the envelopes of a 40 π mm mrad beam in x direction (upper half), y direction (lower half) and the dispersion for a 2.5% momentum deviation (dashed line).

The transmission of separated fragments from the Super-FRS is an important issue. For characteristic examples the fragment production, separation and transport into the collector ring have been simulated with the MOCADI code [4]. The transmission (T) was calculated in two parts: until the exit of the Super-FRS (MF7) and stored in the CR. Realistic target and degrader thicknesses optimized for rate were used for separation and slowing-down to 740 MeV/u. After this separation the beam still is not completely monoisotopic but will be with the additional m/q-separation of the CR. Four cases were selected to give a representative overview. Table 5 shows the emittance of the fragment beams after separation at MF7. The values are defined by two sigma values of the position and angular distribution. The transverse emittance is much increased due to the slowing-down and straggling in the degraders whereas the momentum spread stays about the same. The fragment beam was matched to the foreseen acceptance of the CR ($\Delta p/p=\pm1.75\%$, $\varepsilon_x = \varepsilon_y = 200$ mm mrad).

*Table 5: Transmission of different fragments through the Super-FRS, into the CR, and the emittances and momentum spread at the exit of the Super-FRS (*MF7 *).*

fragment	**^{132}Sn**	**^{232}Fr**	**^{104}Sn**	**^{22}O**
primary beam	^{238}U	^{238}U	^{124}Xe	^{40}Ar
T to MF7 [%]	24	46	79	52
T into CR [%]	14	46	76	33
ratio MF7 / CR	0.59	0.99	0.96	0.63
ε_x [mm mrad]	169	82	90	115
ε_y [mm mrad]	151	38	64	140
2 σ_p/p [%]	3.05	1.21	1.47	3.03

At highest projectile intensities fast extraction represents the most extreme conditions for the production target, see chapter 2.2. Easing of tension can be achieved if the stringent conditions for the size of the beam spot are mitigated. However, an increased size of the beam spot in the dispersive direction means that the fragment separation power is decreased as demonstrated with the detailed simulations in Figure 11. For many in-ring experiments this is no severe restriction.

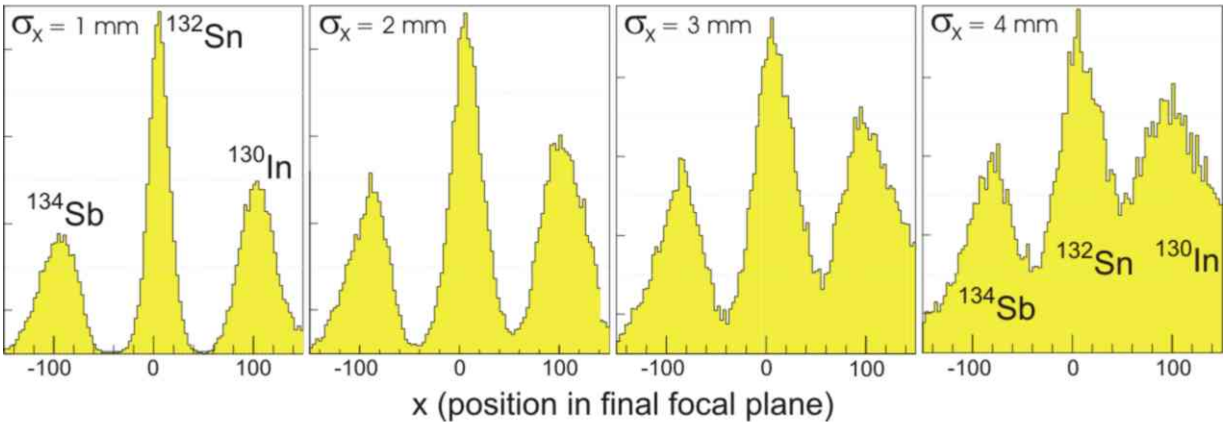

Figure 11: Calculated separation power as a function of the spot size σ_x (dispersive coordinate) at the production target. The selected example represents the separation of ^{132}Sn produced in projectile fission of ^{238}U. Both degraders at PF2 and MF2 had a thickness of half of the ^{132}Sn ion range.

2.1.4.3 Coupling to the low-energy experimental area

The low-energy branch, which delivers secondary beams with magnetic rigidities up to 10 Tm, includes a high-resolution dispersive separator stage behind the achromatic Pre- and Main- Separator. In combination with a set of profiled energy degraders, including a monoenergetic degrader [5], this setup has been designed to drastically reduce the energy spread and thus the range straggling of the hot fragments. Hence, there are two operating modes for this branch. After the energy-spread reduction and absorbers to reduce the fragment energies to Coulomb barrier energies, gamma- and particle-spectroscopy research can be done. Alternatively, the exotic beams can be stopped and cooled in a gas and quickly transferred to ion or atom traps. The system will be fast and universal for all elements and be independent of the chemical properties. With the energy-buncher stage the separated fragment beams can be slowed down and their large momentum spread of up to 5 % can be reduced to a resulting range straggling close to an ideal monoenergetic beam.

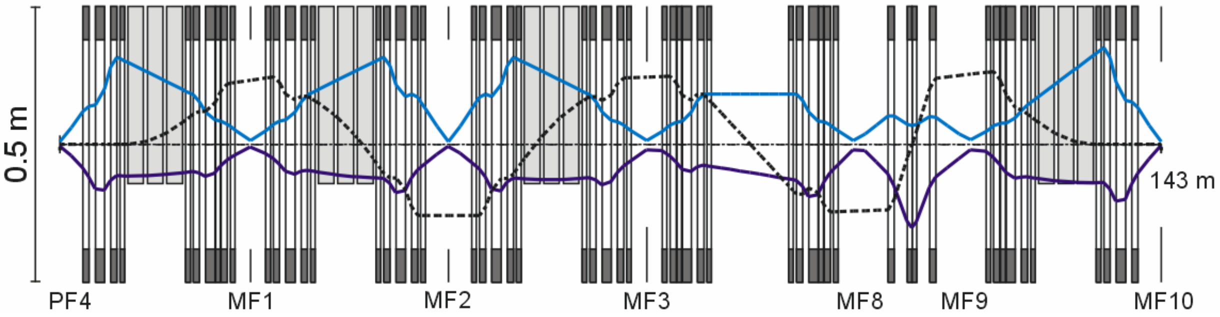

*Figure 12**:** Ion optical layout of the Low-Energy-Branch. Shown are the envelopes of a 40 mm mrad beam in x direction (upper half), y direction (lower half) and the dispersion in case of a ±2.5% momentum deviation (dashed line).*

The momentum spread of the fragment beam can be reduced if the resolving power guarantees that the spot size at the degrader is dominated by the dispersion and not by object magnification and aberrations. Since the emittances of the fragment beams are inevitably large, a large-aperture spectrometer with the necessary high resolving power is needed to compensate for the energy spread.

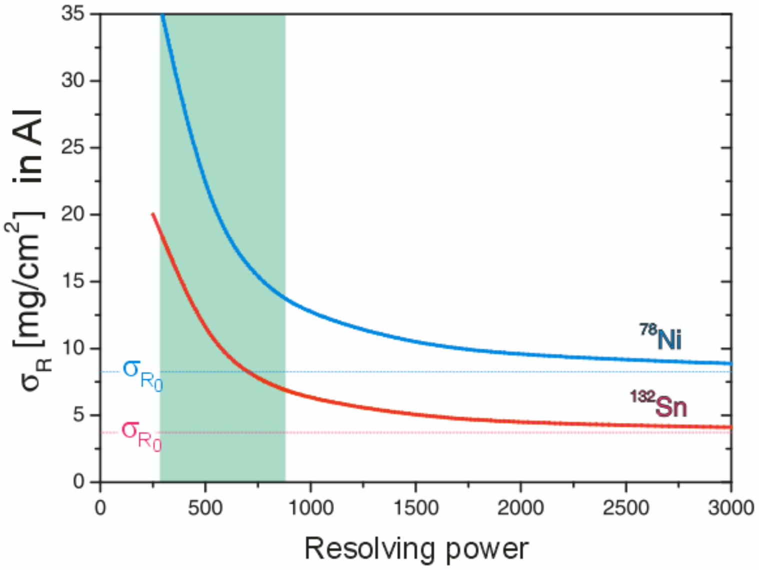

Figure 13: Resolution necessary for range bunching of ^{78}Ni or ^{132}Sn fragments produced in a fission reaction. Achievable range straggling σ_R for 300 MeV/u ^{78}Ni (blue solid curve) and ^{132}Sn (red solid curve) fragments in an aluminum stopper as a function of the momentum resolving power of the energy buncher. The dotted lines indicate the range straggling σ_{R0} of ideal monoenergetic beams of the same isotopes. The resolving-power domain which can be reached with the proposed energy buncher is marked as a green area in the figure.

In total the momentum resolving power of the dipole stage and the energy-loss straggling in a monoenergetic degrader determine how well the energy distribution can be bunched. This is shown in Figure 13 for different fragment beams compared to ideal monoenergetic beams. The area indicated in green represents the working range of the proposed energy-buncher.

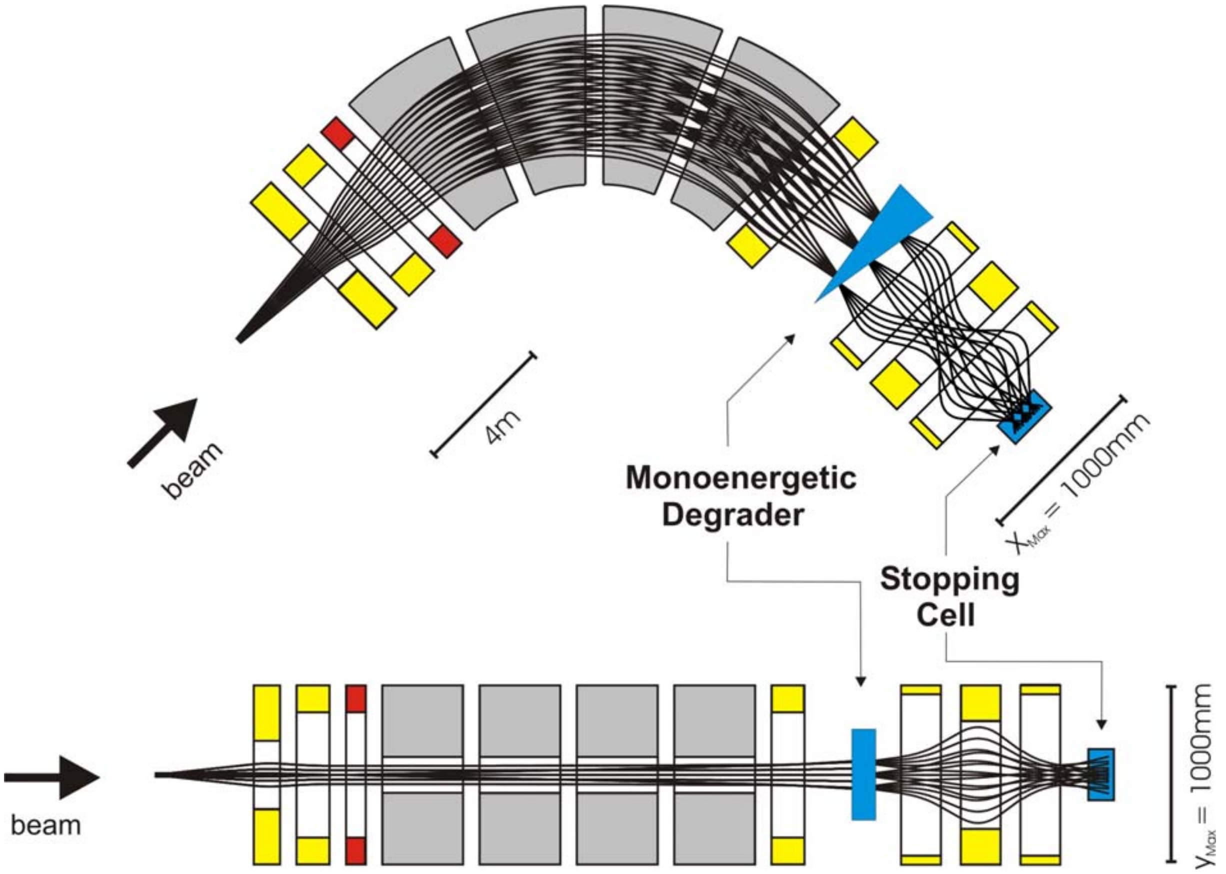

Figure 14:Ion-optical layout of the Energy Buncher, its main characteristics are: $B\rho_{max} = 10$ *Tm,* $\varepsilon_x = 300$ *mm mrad,* $\varepsilon_y = 200$ *mm mrad,* $\Phi_x = \Phi_y = 20$ *mrad,* $\Delta p/p = \pm 2.5\%$*, (transverse and longitudinal acceptance). Under these conditions a momentum resolving power of R=600 can be achieved.*

Figure 14 illustrates the ion-optical layout of the energy buncher. The spectrometer consists of a dispersive ion-optical stage with a large split dipole magnet system, quadrupole (yellow) and sextupole magnets (red). The magnetic quadrupole doublet in front of the dipole magnet is needed to properly illuminate the field volume of the dipole magnet to reach the required resolving power and to focus the secondary beam onto a monoenergetic degrader. The quadrupole triplet behind the dipole magnet guides the exotic nuclei into the gas cell or any other detector array. It will be advantageous to split the large 90-degree dipole magnet in several smaller units.

2.2 Production targets

Similar to the present SIS18/FRS/ESR facility, both, slow and fast extraction from SIS100/300 will be used at Super-FRS: the former (with typical extraction times of a few seconds) for counter experiments at the experimental caves, the latter for experiments with radioactive secondary beams in the storage rings (here short beam pulses with a length of typically $\tau = 50$ ns will be needed). The very high instantaneous power deposited in the target by fast-extracted beams (up to ~200 GW) may lead to explosive regimes [6]. As a result, the target could be destroyed by a single beam pulse, and it may not be usable for the next cycle. Therefore, special considerations for production targets for fast extraction are needed.

The key parameter for target technology is the specific power deposited by the primary beam and the fragments produced in the target. Since only ions lighter than the projectile are formed in projectile fragmentation, it is reasonable to consider only the parameters of the incident beams. The optimum target thickness will range from a few g/cm^2 up to about 8 g/cm^2 depending on the atomic number Z of the projectile and the selected energy. Table 6 lists typical specific energies deposited in graphite chosen as the target material by three benchmark beams, ^{40}Ar, ^{136}Xe and ^{238}U. All beam intensities are taken as 10^{12} ions/cycle, and the beam energies are 1 A GeV. The beam spot is assumed to be a two-dimensional Gaussian distribution with $\sigma_x = \sigma_y = 1$ mm.

Table 6: Typical beam parameters considered for planning production targets at the Super-FRS.

Beam	Total beam energy E [kJ]	Graphite target thickness [g cm^{-2}]	Deposited Energy ΔE [kJ]	Specific Energy $\Delta E/M$ [kJ/g]
^{40}Ar	6.4	8.0	0.83	1.5
^{136}Xe	21.8	6.0	6.0	15
^{238}U	38.1	4.0	12.0	44

2.2.1 Target design for slow-extraction

In slow extraction mode, the typical extraction time is 1 s, and, consequently, the energy values given in Table 6 can easily be converted into power with the same numerical values. The maximum beam power of 12 kW deposited by ^{238}U in the Super-FRS target can be compared to the values found in operating facilities (PSI) or to those considered in planned facilities (RIKEN/BigRIPS and GANIL/SPIRAL-II), see Table 7. The Super-FRS beam power in slow extraction is lower than in the above-mentioned facilities, and it should therefore be possible to use the same target material as chosen for the other facilities, namely graphite.

Table 7: Typical beam parameters for production targets of existing or planned secondary-beam facilities. All target concepts use rotating wheels and DC beams. For Super-FRS slowly extracted beams of a rate 1 /s were assumed. Specific power values are calculated assuming that targets rotate with 60 rpm.

Facility	Beam	Total Beam Power P [kW]	Graphite Target Thickness [g cm^{-2}]	Deposited Power ΔP [kW]	Specific Power $\Delta P/M$ [kW/g]
PSI	P	1000	10.8	54	0.18
RIKEN/BigRIPS	all ions	< 100	1	< 20	0.81
SPIRAL-II	D	200	~ 0.8	200	~ 0.25
Super-FRS	all ions	< 38	4 - 8	< 12	< 0.15

Although graphite has one of the best thermal characteristics, the energy deposited by the uranium beam in a stationary target would lead to very high temperatures of about 20,000 K, which are well above the sublimation point. The solution that has therefore been chosen at PSI, RIKEN, and SPIRAL-II involves a rotating-wheel concept, which allows to increases the volume where the energy is deposited. The same concept will be used at the Super-FRS.

2.2.1.1. Calculations of the target response to beam pulses

Preliminary calculations of the response of a graphite disk with 30 cm diameter and a thickness of 3.6g/cm^2 to a ^{238}U beam (1 *A* GeV, 10^{12} ions/s, homogenous profile, 1 mm radius, normal incidence at 2.6 cm from the outer edge) have been performed with the ANSYS code [36]. The power deposited by the beam was assumed to be removed solely by radiation. Assuming that the target disk rotates with a speed of 60 rpm, maximum temperatures of about 1000°C have been obtained [7] (see Figure 15), which is well within the acceptable technical temperature range for graphite.

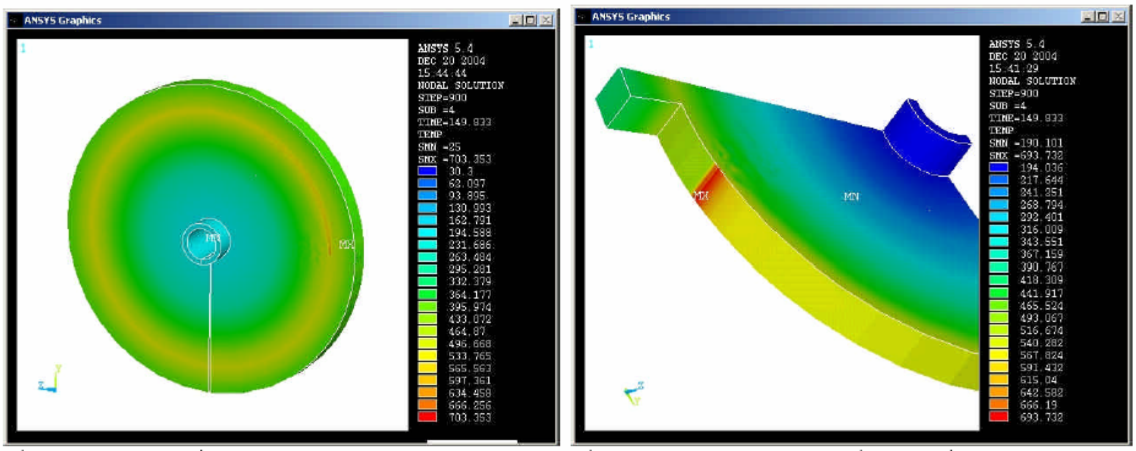

Figure 15: Surface temperature distribution (left) and cross sectional view near the beam spot (right) in a graphite target (rotating with 60 rpm) after 400 sec of irradiation with the ^{238}*U beam (1 A GeV,* 10^{12} *ions/s, homogenous profile, 1 mm radius) according to ANSYS simulation.*

2.2.1.2. Engineering design

Concerning the engineering design of the Super-FRS target for slow extraction the solution developed and used at PSI [8] will be followed.

The target will be a graphite wheel with a radius of 15 cm. Since it will be operated with a wide variety of incident-beam elements, the target thickness must be adjustable. This can be realized e.g. by subdividing the graphite ring into four concentric circles, each 12 mm wide, with thicknesses between 5 and 40 mm. The thickness will be changed by shifting the entire wheel assembly orthogonal to the beam direction. In the same way, the target can be removed entirely from the beam. The rotation will be induced by an electrical motor running outside the vacuum; the torque will be transmitted via steel drive shafts and a 90-degree gear. An important component are the ball bearings of the target wheel; at PSI these are made by GMN Co. [9], Nürnberg, Germany and consist of silver-coated rings and cages with MoS_2 lubrication and silicon nitride balls. They have been proven to run in vacuum during one year without failure [8].

The target will be cooled only by thermal radiation from the surface; no additional cooling will be applied. The advantage of operating graphite at elevated temperatures lies in the fact that the thermal conductivity of graphite decreases with increasing radiation doses, but the residual thermal conductivity after irradiation is higher if the irradiation occurs at high temperature. The maximum operating temperature is given by a tolerable level of the sublimation rate of graphite (about 10 mg g^{-1} $year^{-1}$), and should not exceed 2000 K [8].

From the PSI experience, the best choice of graphite material would be R6510P (SGL Carbon [10], Bonn, Germany). The most important property of this graphite is isotropic expansion during heating thus avoiding excessive radial amplitudes during target rotation.

The target box will be connected to the beam line via inflatable all-metal seals that do not require any clamping ("pillow seals", provided by Prophysik AG [11], Ruggell, Liechtenstein). In addition, all inserts in the target vacuum container (target assembly, pillow seals, diagnostic detectors etc.) together with their respective shielding are sealed from ambient air at working-platform level by organic-material seals that are operated manually during target service periods, see Figure 16. The shielding foreseen for each insert ("plug") ensures that the neutron dose at platform level during beam-on periods is low enough to allow the use of polymer seals.

The need to strip heavy fragments after their creation in the target, such that the maximum yield of fully stripped fragments is obtained, requires a layer of a suitable stripper material (e.g. niobium) deposited on the downstream face of the target wheel. A technical solution that is compatible with the high temperatures of the graphite wheel is presently under discussion.

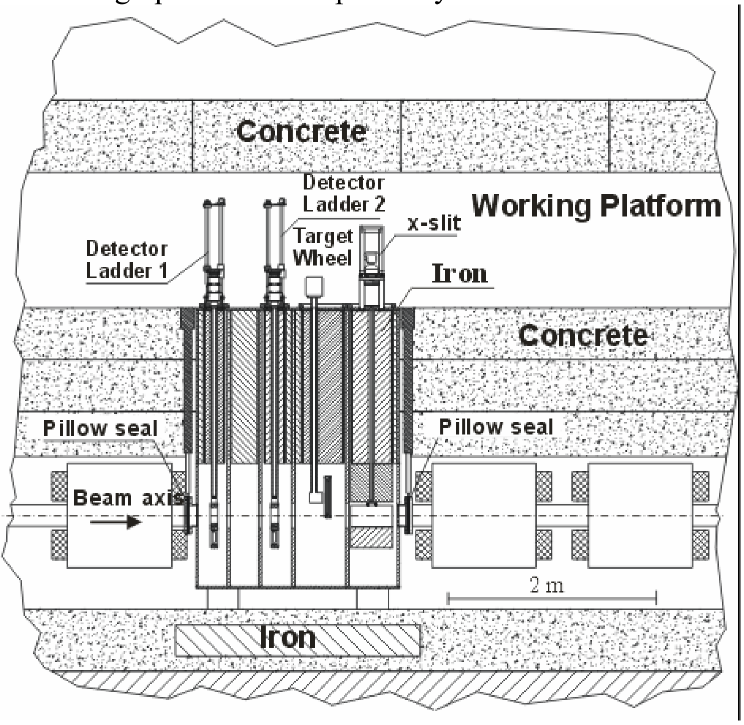

Figure 16: Layout of the target area of the Super-FRS. A plug system is adapted which has proven to guaranty a save and reliable operation at PSI in a very high radiation field. The routine maintenance at PSI is done once per year.

2.2.2 Target design for fast-extraction

The present planning for the Super-FRS target to be used with fast-extracted beams considers two options:

- For low deposited specific beam powers (low projectile Z and/or low intensities, extended beam spot size) the use of the rotating graphite wheel as used for slow extraction is foreseen also for fast extraction; this option was already discussed in the framework of the R3B project [12].
- For the highest power densities, as e.g. deposited by 10^{12} ^{238}U particles extracted within 50 ns, a windowless liquid-metal jet may be considered. This idea follows plans for the RIA heavy-ion fragmentation facility in the USA [13] or those for high-intensity pulsed proton beams e.g. in a ν-factory [14]. In both cases, however, the instantaneous beam power is much lower than estimated for Super-FRS: RIA will run heavy ions in DC mode, whereas pulsed proton beams will be used to produce ν.

Both options have uncertainties that need to be addressed in detail. It has e.g. to be investigated if many short beam pulses impinging on the graphite wheel lead to structural damage in the graphite that could limit the life time of a target wheel.

For the liquid-metal jet option, many questions are unanswered yet: some are related to development and propagations of shock waves induced in the jet, others are related to the constancy of the jet thickness in beam direction (in the steady state or after disruption), or to safety issues in case of hazardous metals used for the jet.

2.2.2.1 Fast-extracted beams on a graphite wheel target

In view of the complexity of the operation of a liquid-metal target, it is desirable to use the rotating-wheel target also for fast-extracted beams, as long as the critical parameters of graphite (temperature, pressure) are not exceeded. This will be the case if the projectile Z or the beam intensities are relatively low. A reduction of the power density of the beam can also be achieved by extending the size of the beam spot; a wider beam spot in the dispersive (x-) direction will deteriorate the ion-optical resolution, see Figure 11. An extended beam spot in y-direction will not affect the resolution but reduce the transmission. Going to σ_y=12 mm instead of 2 mm will reduce the transmission into the CR without changes in the optics by a factor of three.

In Table 8 we present the calculated requirements for the beam spot size to use the full intensity of 10^{12}/spill for different projectiles 1 A GeV. In these calculations the critical temperature of about 2000 K [8] and a tensile strength of 150 MPa are not exceeded. For reliable conditions of fast extraction the sudden temperature increase of the graphite should not exceed 472 K and a corresponding pressure rise of 42 MPa. The initial temperature (T_i) for ^{238}U ions is assumed to be 1273 K, see *Figure 15*. Lighter ions heat the target less.

Table 8: Temperature increase ΔT from the initial temperature T_i in the centre of a Gaussian beam spot. The assumed area of beam spot on the graphite target is presented in the last column.

beam	T_i [K]	ΔT [K]	area [mm^2]
10^{12} U	1273	471	48.0
$5\text{x}10^{11}$ U	1071	248	24.0
10^{12} Xe	966	472	16.4
10^{12} Ar	552	471	1.9

That means that the identical graphite wheel which will be used for slowly extracted beams can serve as a good option to perform experiments with high power fast extracted beams too. Nevertheless, due to the enlarged beam spot at the production target the transmission and the separation power of the Super-FRS are restricted in this operation mode, especially for the experiments using uranium primary beams. More refined thermo-mechanical calculations will be performed in the future to verify the estimates mentioned above.

2.2.2.2 Choice of material for liquid-metal jet

As mentioned above, the very high instantaneous power deposited by the uranium beam in fast extraction mode could lead to the destruction of solid materials. As an alternative solution, a windowless liquid-metal target will also be considered. The following liquid metals can be considered as potential targets for Super-FRS: light ones (Li, Na), medium-heavy ones (Ga), and heavy ones (Hg, Pb). The physical properties of some of the possible target materials are given in Table 9. Only pure elements are listed, since eutectics can be elementally separated during irradiation. Lower-Z targets are preferable due to lower multiple scattering of radioactive nuclides, higher number of atoms per unit energy loss of the primary beam, and smaller range of long-lived radioactive products.

Table 9: Physical properties of several materials considered as liquid-metal jet targets for fast extraction.

Target	Density of liquid [15] [g/cm^3]	Melting point[16] [^{o}C]	Boiling point [16] [^{o}C]	[a] Thermal conductivity [15] [W m^{-1} ^{o}C^{-1}]	[b] Vapour pressure [17] [Pa]	[c] Sound velocity [16] [m/s]	[a] Specific heat [15] [J kg^{-1} ^{o}C^{-1}]
Li	0.508	180.54	1342	42.258	$1.63 \cdot 10^{-8}$	6000	4226
Na	0.930	97.72	883	84.517	$1.33 \cdot 10^{-5}$	3200	1381
Ga	6.090	29.76	2204	33.472	$9.31 \cdot 10^{-36}$	2740	398.7
Hg	13.500	-38.83	356.73	8.368	$2 \cdot 10^{-4}$	1407	138.1
Pb	10.600	327.46	1749	16.318	$4.21 \cdot 10^{-7}$	1260	150.6

[a] Value given for the liquid state.
[b] Value of the vapour pressure is given for all materials but Na at the corresponding melting-point temperature. For Na, the value is given at T = 961 ^{o}C.
[c] Except for mercury, the values are given for the given material in solid state.

A definite decision on the material for the liquid jet will be made after detailed investigations of the hydro-dynamical and chemical behavior of the considered materials under high instantaneous power deposition have been performed.

2.2.2.3 Calculation of jet response to fast beam pulses

For the first preliminary test calculations, a jet made of liquid lithium was assumed. The response of a liquid-lithium jet to a high-intensity ^{238}U beam pulse of 50 ns length has been calculated with a 2-dimensional hydro-dynamical code, BIG-2 [18]. 10^{12} ^{238}U ions at 1 GeV/u within 50 ns were impinging on a 7cm thick liquid Li target. The beam spot was assumed to be $\sigma_x = \sigma_y = 1$ mm. The starting point of the calculation was at t_0=50 ns, right after passage of the beam pulse. In the present 2-dimensional calculation the high power density deposited in a column of liquid Li is predicted to lead to a fast vaporization of the Li contained in the volume traversed by the beam and to a shock wave that travels orthogonal to the beam direction.

The finite velocity of sound in Li makes sure that during the interaction the target density is unchanged, so that the probability of producing a fragment and its kinematical properties are unchanged. Typical parameters of Li in the beam trajectory according to the BIG-2 calculation are a temperature of 13,000 K, a pressure of 14 GPa, and an energy density of 42 kJ/g, see Figure 17 (left).

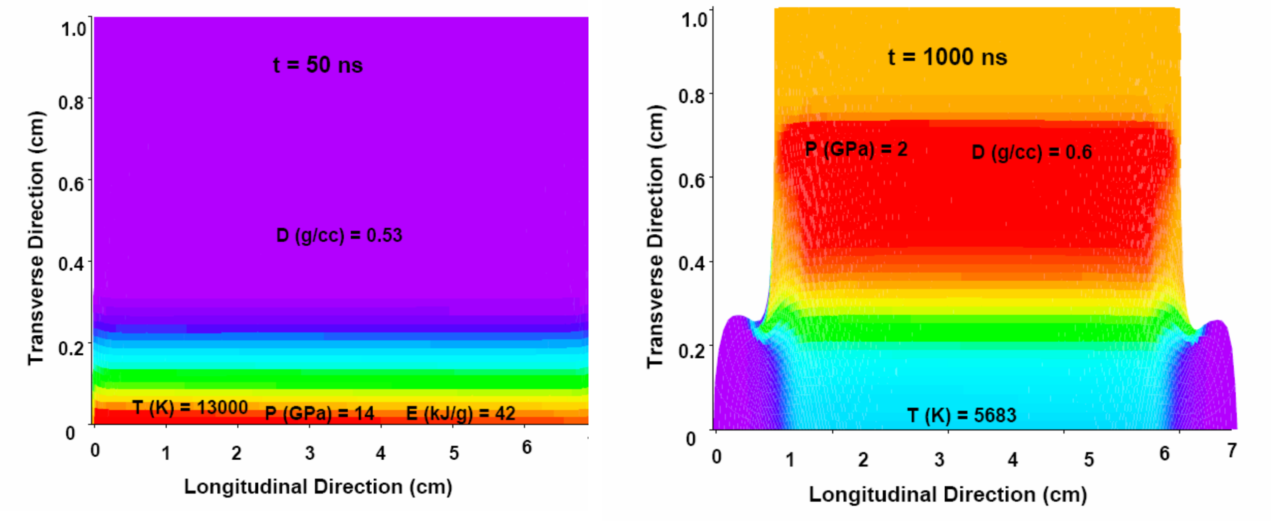

Figure 17: Calculated density of lithium (colour code is given in Figure 18) - left: after the beam passage (after 50 ns) and right: 1μs after the passage of beam. Along the beam trajectory the vaporized Li explodes. (violet regions in the figure). Orthogonal to the beam direction the shock front moves by about 8 mm within 1μs. For several positions in the Li jet, the values of temperature (T), pressure (P) and energy density (E) are also given in the plots.

The BIG-2 calculation predicts that the vaporized Li will explode in (positive and negative) beam direction with velocities of about 10 km/s, with the central density being reduced rapidly,see Figure 17 right. Orthogonal to the beam direction, temperature and density are not much higher than normal, but a pressure wave travels outward with an initial velocity of about 1.5 km/s. After 1μs the shock front has moved by about 8 mm.

An open question is how fast this shock wave will be damped and what will be the pressure at the shock front when the front hits structural components (e.g. the nozzle of the jet). Another question is how fast the jet will reform after vaporization and return to a steady flow. To answer these questions in detail, 3-dimensional hydro-dynamical calculations of the behavior of the metal jet are planned to be performed in near future.

Like in the case of the rotating graphite wheel it is of great interest to apply the conditions of the windowless liquid target with enlarged beam spots. Calculations with BIG-2 for 10^{12} ^{238}U ions at 1 GeV/u within 50 ns impinging on the liquid lithium target with a spot area of 48 mm^2 demonstrate that after 1μs the target remains liquid (density changes only by 0.04 g/cm ^{3}) and is only marginally influenced by shock waves, see Figure 18. The promising results for the graphite wheel with enlarged beam spots in Table 8 are even more relaxed for a liquid Li target, i.e., the minimum beam areas can be significantly smaller.

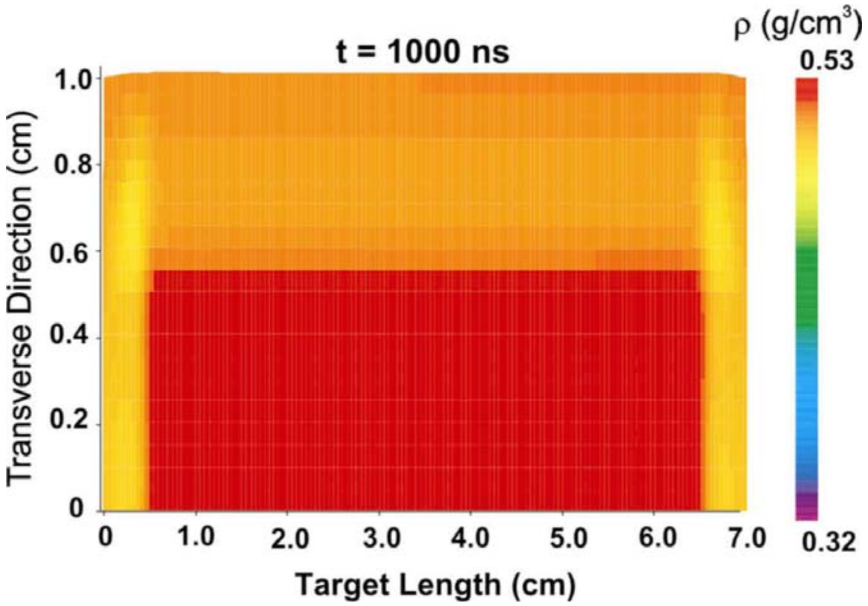

Figure 18: Calculated (BIG-2) density evolution of a 7cm liquid Li target after the penetration of 10^{12} ^{238}*U ions at 1 GeV/u within 50 ns, at 1000 ns after the beam interaction. The assumed beam size has an area of 48 mm*^{2}*. Under this condition the density changes only marginally between 0.53 to 0.49 g/cm*^{3} *and hydro-dynamical shock waves will not destroy the flow, contrary to the case in Figure 17.*

2.2.2.4. Engineering design

A prototype of an operational liquid-Li loop was built and successfully tested with an electron beam at ANL, Argonne (USA). The operation time was limited to a few minutes, because the heat induced by the beam was not removed from the Li volume.

Before performing a detailed engineering design dedicated 3-dimensional hydro-dynamical calculations and feasibility studies have to be performed. Questions to be solved are a heat-exchange system that allows extended operation of the jet including the impurity control system. One also needs to develop a comprehensive safety system that assures safe operation. For operation at the Super-FRS, the space restrictions at the production target site have to be respected.

At the RIA facility the target will be operated in a steady state (the instantaneous power deposited will be around 0.12 MW), while in case of the Super-FRS target in fast extraction we will deal with much higher deposited powers (about max. $240 \cdot 10^3$ MW), and, therefore, a direct scaling from the RIA to the possible Super-FRS liquid-metal jet target is not possible. Dedicated experimental and theoretical studies are needed in order to test the applicability of a liquid-metal jet concept at the Super-FRS.

2.2.3 Conclusion

In summary, we can state that the target design for slow extraction is technically solved and fulfils all the requirements for experiments with exotic nuclei at the Super-FRS. Prototyping and test experiments at the present FRS will be the next steps.

For fast extracted beams the design of a universal production target is still in progress. However, the rotating graphite wheel, ideally suited for slow-extraction, can also be used for the fast extraction at highest intensities under the condition that the separation power of the Super-FRS and the transmission are reduced. Replacing the graphite wheel by a liquid target with an enlarged beam spot yields even more favorable conditions for a long-term stable operation for the heaviest projectiles with 10^{12} ions within 50ns pulses. Dedicated 3-dimensional hydro-dynamical calculations on the behaviour of the liquid jet are in preparation. These more realistic calculations will improve the knowledge on practical aspects for the fast extracted beams.

2.2.4 Cost estimates for the target area

Target cost estimate	Quantity		
Target chamber	1		
Graphite wheel assembly + spare1	1		
Jet target assembly (rough estimate)			
Pillow seals	2		
Detector feed-throughs	2		
Slit system (x)	1		
Fe+X shielding material (26 ton)	26		
Crane (20 tons) + control	1		
Safty/transport container			
Vacuum system			
Cooling system			
Alignment tools			
Storage cell for target			
Hot cell			
Total costs			

2.3 Magnets

Since the Super-FRS has to accept fragment beams with a large phase-space volume it has to be equipped with large aperture magnets. In addition, the magnets have to provide high magnetic pole-tip flux densities to guide the 20 Tm ion beams. The dipole magnets will have a deflection radius of 12.5 m, a field of 1.6 T, and a gap of at least 140 mm. Most of the quadrupole lenses must have a good field aperture of 380 mm and require pole tip values of up to 2.4 T. These specifications suggest the use of superconductivity. We plan to apply the superferric technology with iron-dominated lenses where the magnetic field is formed by shaped iron yokes driven by superconducting coils. This technology is already successfully applied at the A1900 in-flight fragment separator at MSU, USA[19], at the BigRIBS fragment separator at RIKEN, Japan [20] and will be also applied at the future in-flight separators for RIA in the USA [21]. However, all of these facilities will work at much lower beam energies and hence the magnets are much smaller compared to those of the Super-FRS. Besides the operation of the large size magnets the other main challenge will be to work in a very high radiation level, especially in the target area and the first stage of the Super-FRS where the non-reacted primary beam will be dumped. Table 10, Table 11, and Table 12 list the specification of the magnetic elements for the Super-FRS.

Table 10: Design parameters for the dipole magnets of the Super-FRS

Location of the magnet	Dim.	Pre-Separator, 1^{st} stage	Pre-Separator, 2^{nd} stage	Main-Separator	Energy Buncher
Number of magnets		3	3	21	4
Design		H-type, straight	H-type, straight	H-type, straight	H-type, straight
		resistive rad. resistant	superferric	superferric	superferric
Max. field	T	1.6			
Average operating field	T	1.15			
Min. field	T	0.15			
Bending angle	deg	11	11	9.33	22.5
Edge angles (entrance / exit)	deg	5.5	5.5	4.665	11.25
Curvature radius, R	m	12.5			6.25
Effective path length, L	m	2.39	2.39	2.04	2.43
Useable horizontal aperture:	mm	±190			±300
Useable vertical gap:	mm	±70			±100
Vertical pole gap height	mm	±85			±120
Field quality (over horiz. apert.)		$\pm 3\times10^{-4}$			
Overall length	m	2.8	2.8	2.4	2.85
Overall width	m	2.7	2.1	2.1	3.1 ?
Overall height	m	1.9	1.3	1.3	1.9 ?
Overall weight	kg	80000	TBD	TBD	TBD
Current at max. field	A	750	186	186	TBD
Inductance	mH	1500	42700	36800	TBD
Resistance	mΩ	140	0	0	0
ramp rate		DC Magnets			
average power consumption	kW	145	0	0	0

Table 11: Design parameters for the quadrupole magnets of the Super-FRS

Location of the magnet	Dim.	Pre-Separator, 1st stage	Pre- & Main-Separator		Energy Buncher	
Number of magnets		2	34	27	1	4
Design		resistive rad. resistant	superferric			
Max. gradient	T/m	15.0	10.0		5.0	3.0
Average operating gradient	T/m	10.5	7.0		4.0	2.5
Min. gradient	T/m	1.5	1.0		1.0	0.6
Effective length, L	m	1.000	0.800	1.200	0.900	1.000
Useable horizontal aperture:	mm	±90	±190		±150	±300
Useable vertical aperture:	mm	±90	±100		±150	±120
Gradient field quality		$\pm 8 \times 10^{-4}$	$\pm 8 \times 10^{-4}$		$\pm 8 \times 10^{-4}$	$\pm 8 \times 10^{-4}$
Pole radius:	mm	90	240		190	TBD
Embedded octupole component G'' :	T/m^3	-	15	-	-	TBD
Overall length	m	1360	1260	1560	TBD	TBD
Overall width	m	1.600	1.400 (w/o cryostat)	1400 (w/o cryostat)	TBD	TBD
Overall height	m	1.600	1.400 (w/o cryostat)	1.400 (w/o cryostat)	TBD	TBD
Overall weight	kg	18000	11000 (w/o cryostat)	14500 (w/o cryostat)	TBD	TBD
Current at max gradient	A	2000	627	627	TBD	TBD
Inductance	mH	83.0	4240	6350	TBD	TBD
Resistance	mΩ	73.3	0			
ramp rate		DC Magnets				
average power consumption	kW	351	0			

Table 12: Design parameters for the hexapole magnets of the Super-FRS

Location of the magnet	Dim.	Pre-Separator, 1st stage	Pre- & Main-Separator, Energy Buncher
Number of magnets		1	39
Design		resistive rad. resistant	superferric
Max. hexapole component	T/m^2	15.0	15.0
Effective length, L	m	0.600	0.600
Useable horizontal aperture:	mm	±190	±190
Useable vertical aperture:	mm	±100	±100
Overall length	m	950	TBD
Overall width	m	Ø 0.800	TBD
Overall height			TBD
Overall weight	kg	1800	TBD
Max. Current	A	TBD	TBD
Inductance	mH	TBD	TBD
Resistance	mOhm	TBD	TBD
ramp rate		DC Magnets	
average power consumption	kW	TBD	0

2.3.1 Superconducting magnets

The use of superconducting magnets would be the best technical solution due to the large aperture radii and high pole tip flux densities of the quadrupole magnets. Except the 1st stage of the Pre-Separator all other dipole stages will be equipped with superconducting dipole magnets, since amp-turns (large gap sizes of theses magnets) and operation are most cost effective for this realization. We have chosen to adopt the technique of superferric magnets, considering the fabrication cost and liquid helium consumption to be more favorable compared to cos(Θ) magnets.

Dipole magnets

The dipole magnets have a bending radius of 12.5 m and a maximum flux density of 1.6 T. The implementation of localized beam dumps in the first dipole stage of the Pre-Separator requires 3 dipole units each having a deflection angle of 11°. This results in an effective path length of about 2.40 m. Such short units can be built as rectangular magnets (Figure 19) which have the advantage of a rather simple coil construction. The realization of a negative curvature is avoided. Following these concepts we divided all dipole magnets of the Super-FRS into several units (see Table 10). A first 2D/3D magnetic design for such a dipole unit was performed using the code Opera-2D/3D [22] (Figure 19 and Figure 20). Another advantage of using several short dipole units is, that most probably the same tooling devices as for the CR dipole magnets can be used (cost optimization), since the cross section of both dipole magnets is quasi identical (see also the *Technical Report on the CR for FAIR*).

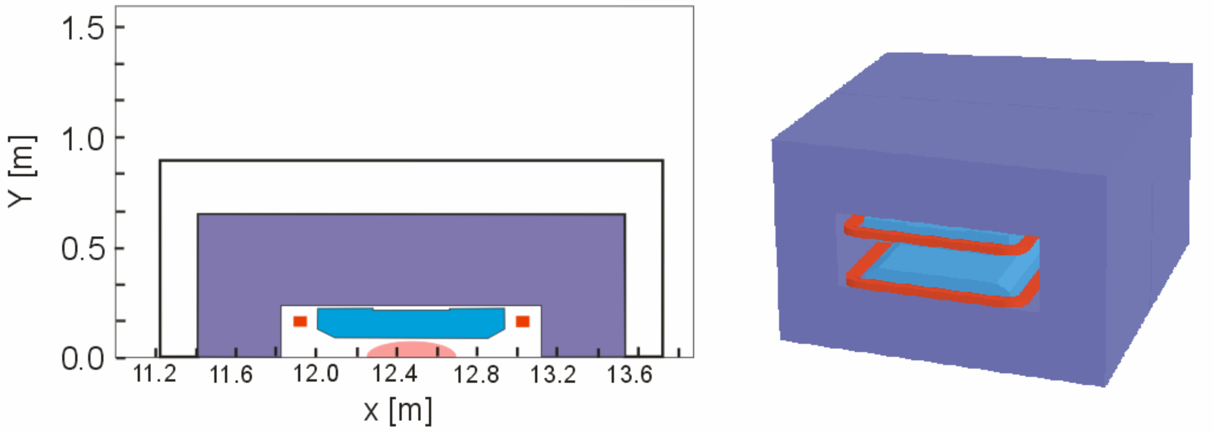

Figure 19: Two-dimensional cross section and three-dimensional view of a 2.4 m long straight dipole magnet

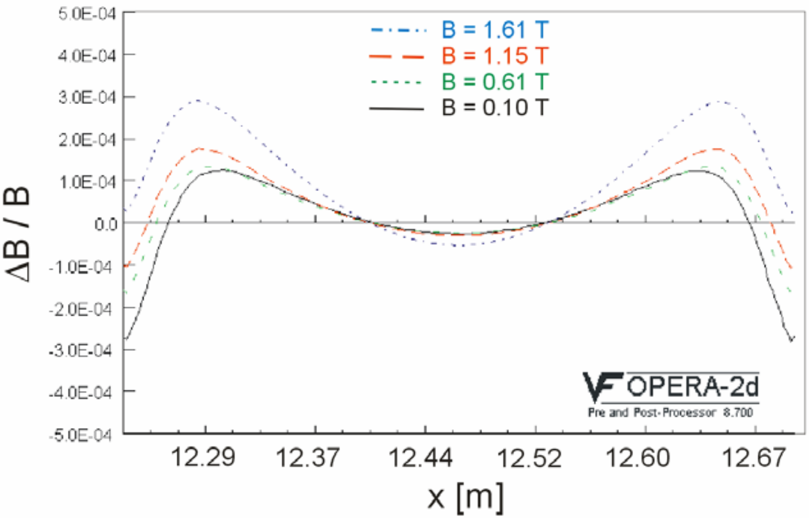

Figure 20: Calculated field distribution for the large- aperture Super-FRS dipole magnet shown in Figure 19 .

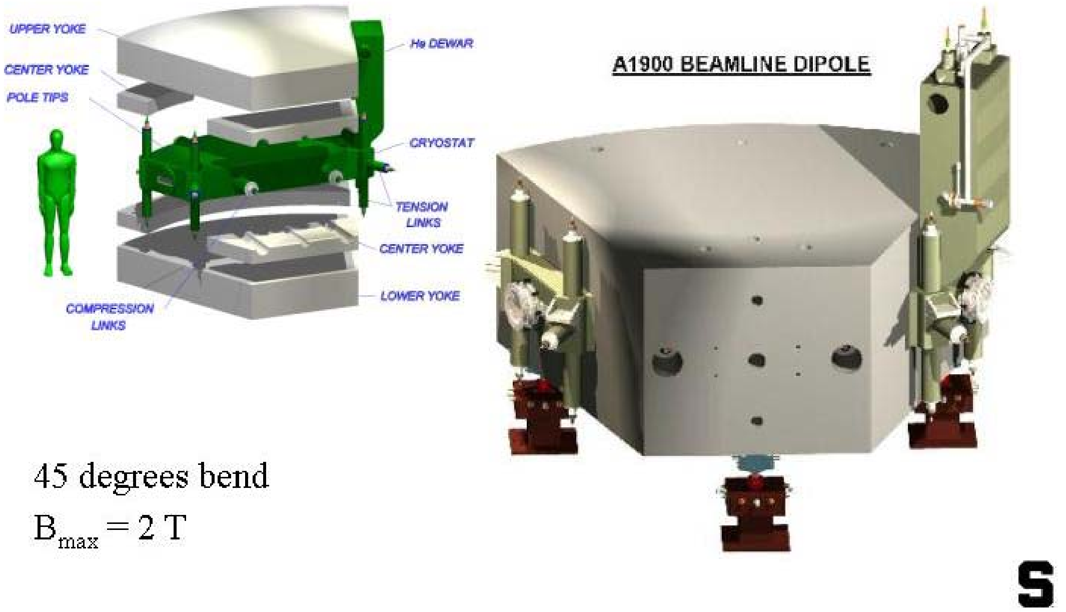

Figure 21: A1900 dipole at NSCL-MSU. The left side shows its different components like iron pole and yoke and the cryostat with its He dewar. The right side shows the assembled magnet.

Quadrupole magnets

Each dipole stage of the Super-FRS is equipped with a quadrupole triplet in front and behind the dipole magnet. The standard quadrupole triplet consists of 3 cold-iron, superferric quadrupole magnets with the same warm aperture radius of ±190 mm. They have lengths of 800 mm, 1200 mm, and 800 mm and provide a max. field gradient of 10.0 T/m. Octupole correction coils are superimposed to the 800 mm long quadrupole magnets to allow corrections of image aberration. The 3 quadrupole magnets will be assembled in one common cryostat together with a 600 mm long hexapole magnet before and behind this triplet. The same principle is used for the A1900 quadrupole triplet [23] and the quadrupole triplet for the BigRIBS [24], see Figure 22.
Furthermore, the Super-FRS uses 3 quadrupole triplets with a length of 1200 mm and a warm aperture radius of 190 mm for each single magnet. R&D work has to be done to solve the technical problems with this extended geometry of such 6-7 m long unit embedded in one cryostat.
Even larger apertures, 300 mm, are planned for the quadrupole magnets of the Energy-Buncher. The corresponding R&D work for this type of magnet will be done in collaboration with the RIA magnet group.

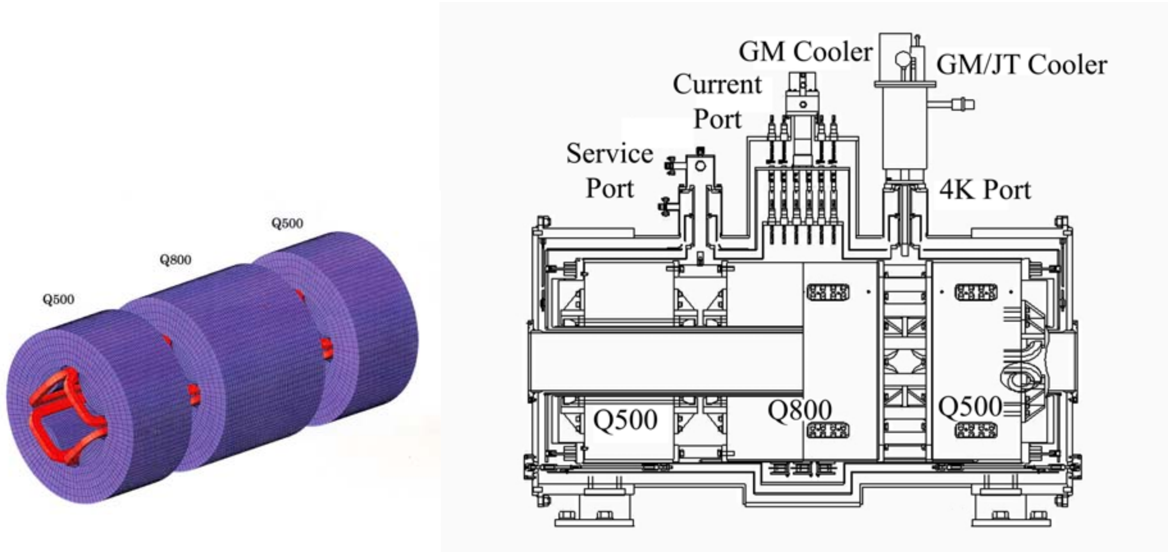

Figure 22: Schematic view of the RIKEN prototype quadrupole triplet (left side) and its installation into the cryostat (right side) [24].

More detailed considerations on superconducting magnets for the FAIR facility are compiled in the *Technical Report on Superconducting Magnets for FAIR.*

2.3.2 Radiation hard magnets

The target area as well as the beam dump area is in high fluxes of high-energy particles, mainly neutrons and protons. Magnetic elements located in these areas have to be reliably operated for the lifetime of the facility. The most radiation-sensitive part of a magnet is the electrical insulation. Conductors like copper and aluminum are many orders of magnitude more radiation resistant than organic insulators. Even the superconductors like NbTi and Nb_3Sn are at least 25 times more resistant than common organic epoxies and 10 times better than other organic insulation [25, 26], see Table 13. Therefore, ceramic insulators are required in the high-radiation zones of the Pre-Separator.

Table 13: General radiation sensitivity of coil materials and insulators [25,26].

Material	**Radiation limit / [Gy]**
NbTi	$\approx 5 \cdot 10^8$
Nb_3Sn	$\approx 5 \cdot 10^8$ (+)
Copper	$> 10^{10}$
Ceramics (Al_2O_3, MgO, etc)	$> 10^9$
Organics	10^6 -10^9

The magnets for the Super-FRS placed in high-radiation areas are difficult to construct because they require large apertures and high field gradients in the quadrupole magnets and large gaps in the dipole magnets. Designing the magnets with a resistive coil option leads to large magnets with a huge power consumption, while using superconducting magnets require iron warm solutions, in order to keep the refrigeration load (because of neutron heating)at an acceptable level.
Consequently, we will examine both options, resistive and superconducting. Presently we consider to use resistive solutions for the quadrupole magnets behind the production target, the three dipole units in the first stage of the Pre-Separator and the subsequent hexapole behind PF1 (the location of the last beam dump).

Normal conducting magnets.

Figure 23 shows a possible solution for a normal conducting dipole magnet for the Pre-Separator. This magnet consists of coils with mineral insulation cables (e.g. MgO, Al_2O_3). The conductor could be built with water hollows for direct cooling or with solid conductors for indirect cooling. These types of magnets exists already in laboratories [27].

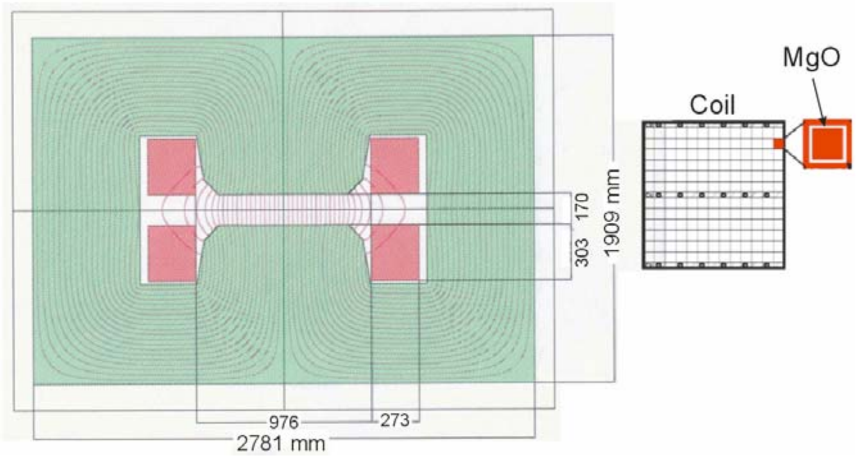

Figure 23: Possible solution of a normal conducting radiation resistant dipole for the 1st stage of the Pre-Separator. The coil consists of fully mineral insulated (MgO) cables achieving an engineering current density of ≈1.5 A/mm².

Superconducting Magnets.

Crucial issues for the superconducting solutions are:

1. Is the radiation flux so high that the superconductor is driven above the critical temperature?
2. What is the expected lifetime of the magnet?
3. Can a cryogenic system provide the power to compensate the heat load due to radiation?

The first question implies a heat load of less than 1 to 3 mJ/g [28], otherwise it will quench. 1 mJ/g translate to a dose rate of 1 Gy/s. Materials used for conductors and electrical insulation have different radiation sensitivities and are listed in Table 13. If we assume that the Super-FRS will be operated for 4000 hours per year, the accumulated dose at the quench limit is 14 MGy per year. Thus for an anticipated twenty-year life span, the dose is close to the limit for the superconductors and beyond the lifetime of organic materials. The radiation field and an effective shielding are subjects in the next chapter.

2.3.3 Radiation shielding of magnets behind the target and beam dump

The inevitable nuclear interaction in the target and the beam dump requires special considerations of the damage of the magnetic elements. In addition also the heating due to radiation is a critical issue for the operation of superconducting magnets.

The following magnet sections deserve special investigations:

- The first quadrupole behind the target
- The first dipole magnets
- The first hexapole magnet behind PF1

The deposited energy in the coils of these magnets is calculated in the following by PHITS [31] simulations.

Quadrupole magnets behind the target:
The radiation field behind the target is mainly caused by the fragments emitted in wide angles outside the acceptance of the Pre-Separator and by light secondary particles like protons and neutrons. Therefore, we have foreseen to install a 40 x 40 x 40 cm^3 iron shielding block in front of the first quadrupole magnet which stops the lighter ions and neutrons. This iron block should have an aperture just small enough to let the intense heavy ions pass. The light particles cannot be completely shielded by this iron block, therefore a detailed investigation was performed with the computer code PHITS [31]. The assumed geometry is depicted in *Figure 24* and the case for 10^{12} ^{238}U ions at 1500 MeV/u impinging on a 4 g/cm^2 carbon target has been simulated.

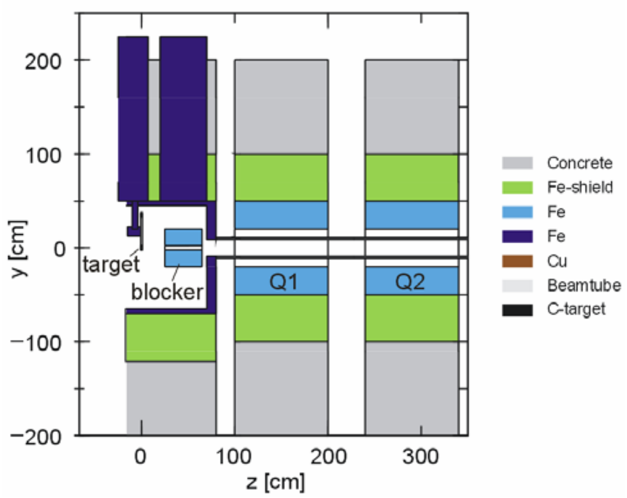

Figure 24: Geometry of the iron beam block behind the target wheel at PF0 shielding the successive quadrupole magnets Q1 and Q2.

Figure 25 shows the heating of the iron block per incident uranium ion. The total power deposited can reach 2kW which would exceed the performance of a practical cryogenic system. Critical are the coils of the subsequent magnets especially in case of superconducting magnets. The heating must stay below a quench limit of about 1 mJ/g. In the simulation the conductor was assumed to consist of a pure copper as the Nb/Ti is only a small fraction. A detailed plot of the deposited energy at the entrance of the quadrupole magnets is given in *Figure 26*. Note that, 1 MeV/cm^3 per incident ion corresponds to 18 mJ/g for 10^{12} ions in copper.

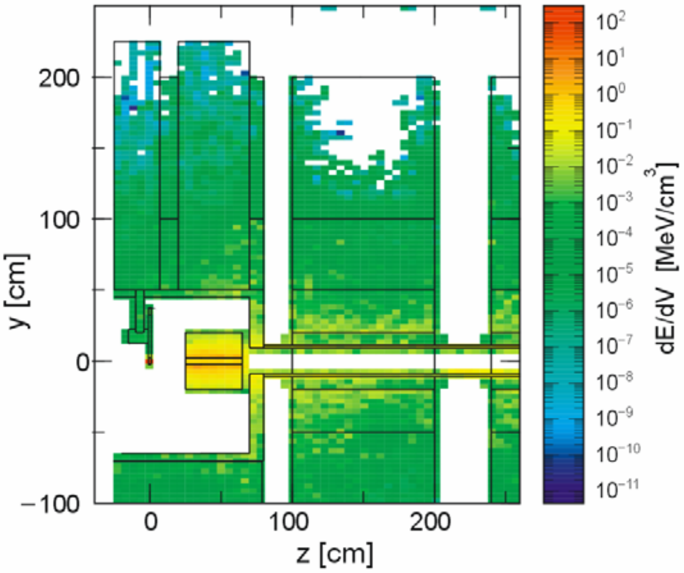

Figure 25: Energy deposition per primary 1.5 GeV/u uranium ion impinging on the 4 g/cm^2 C target. The primary beam and fragments pass through the gap in the shielding block.

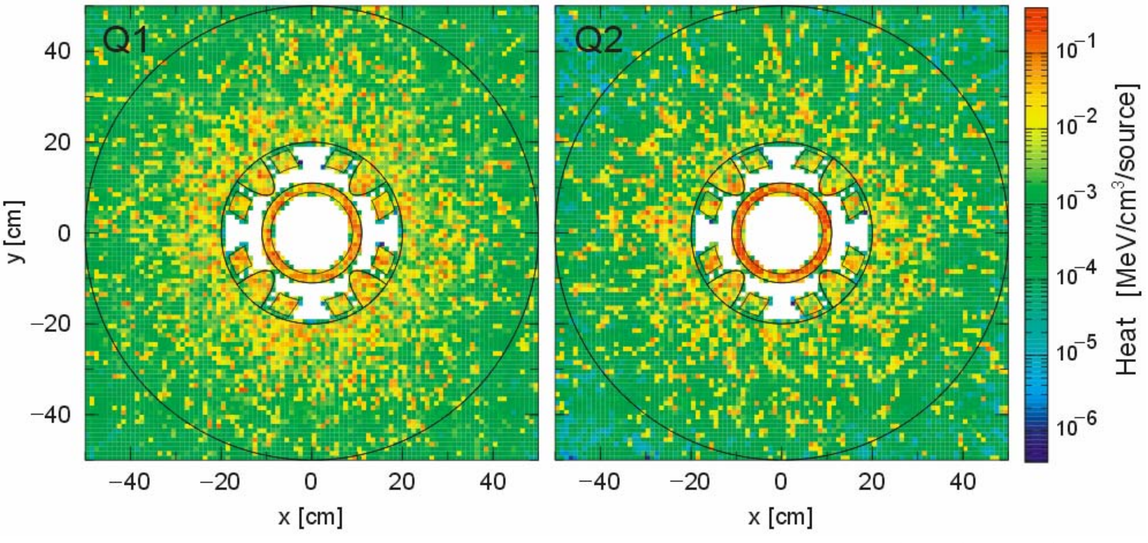

Figure 26: *Deposited energy per primary uranium ion at the entrance of the first (left) and second (right) quadrupole magnet behind the 4 g/cm^2 carbon target.*

The maximum energy density deposited by one spill in a part of the coil of the first quadrupole magnet is 0.0256 MeV/cm^3 per incident ion or 0.46 mJ/g for 10^{12} ions. The calculation was performed for the case of a 1500 MeV/u uranium beam on a 4 g/cm^2 target. This value is below the quench limit but the total power deposited exceeds the practical limit for a cryogenic system.

Hexapole behind the beam dump at PF1:

At the beam dump positions at BC1, BC2, PF1 the full primary beam can be dumped. Much thicker shielding is therefore required than in the target area. The simulation using PHITS showed that 80cm of iron is sufficient to suppress the neutron flux sufficiently. The geometry investigated is shown in *Figure 27*. Here the graphite part has an inclined surface to increase the range straggling, consequently the energy-loss density in the bulk material is reduced substantially. Critical are the coils of the following hexapole magnet.

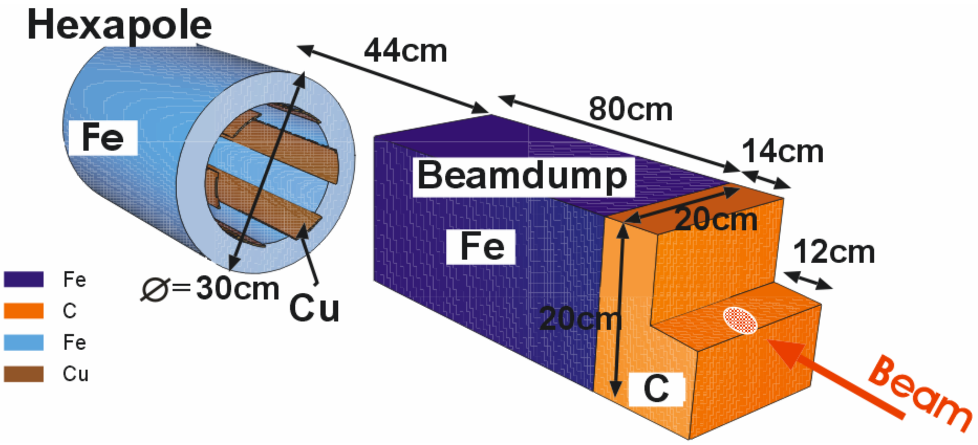

Figure 27: Geometry of the beam dump in front of the hexapole magnet at PF1 used in the calculation with PHITS [31].

In a side view the flux of protons and neutrons is shown in
Figure 28, *Figure 29*. Whereas the Uranium ions are stopped in the graphite an intense beam of protons goes deep into the iron. Outside of the beam dump the radiation is dominated by neutrons having a wide distribution on the hexapole magnet.

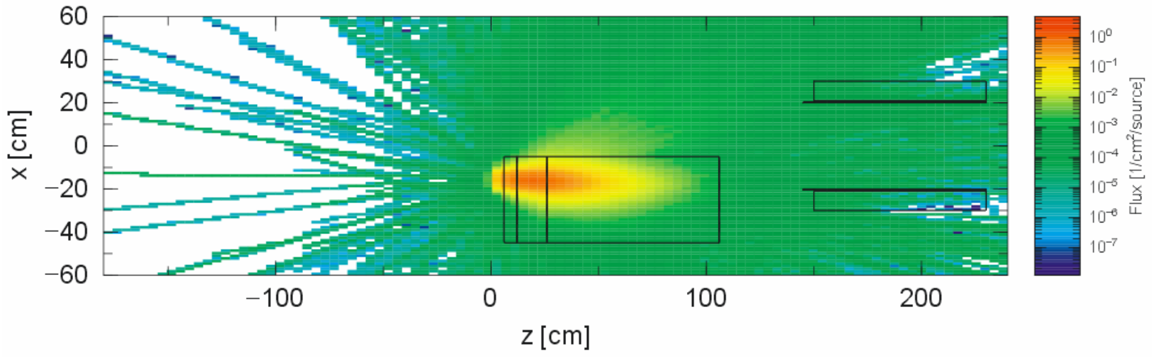

Figure 28: Fluence of protons per incident ^{238}U ion at 1500 MeV/u in the beam dump area at PF1.

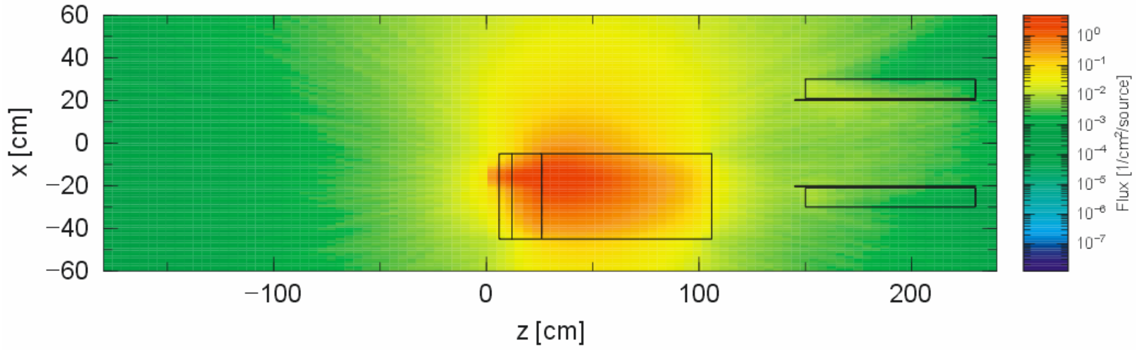

Figure 29: Fluence of neutrons per incident ^{238}U ion at 1500 MeV/u in the beam dump area at PF1.

The maximum deposited energy density in the coil in the direction of the incident primary beam of 0.045 MeV/cm^3 corresponds to 0.81 mJ/g for 10^{12} uranium ions.

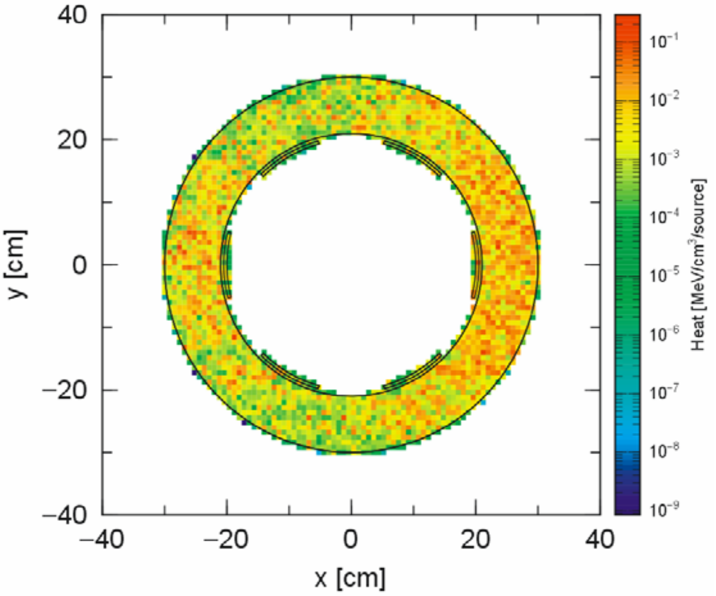

Figure 30: Calculated energy deposition in the hexapole magnet behind PF1. The outer thick ring represents the iron part and the six small layers the coils of the hexapole magnet.

The results for the beam dumps between the dipole magnets (BC1 and BC2) are similar to the ones at PF1 as the same thickness of the beam dump can be used. The situation for the dipole magnet is in general less critical because the coils are not positioned in the same plane as the beam.

2.3.4 Magnet power supplies

The demands for magnet power supplies for the Super-FRS are deduced by the requirements of field homogeneity and stability of the magnets. Sufficient experience is available from operating the present FRS facility. While for superconducting magnets the power supplies need only to provide the requested current, rather large power supplies are needed for the power-consuming normal conducting, radiation resistant magnets in the first stage of the Pre-Separator. For all types of power supplies needed, appropriate devices are available on the market and no special R&D work on this topic is foreseen.

2.3.5 Cryogenic distribution system for the Super-FRS

There are 24 superconducting dipole magnets in the second half of the Pre-Separator and in the Main Separator of the Super-FRS. The Super-FRS dipole magnet has a quite similar design as the CR-dipole. To reduce the cold mass, the Super-FRS dipole has warm iron and warm bore. Only the coils will be cooled in liquid helium. Based on the lattice design, every three neighboring dipole magnets could be arranged as one group of magnets which is controlled by one single feedbox for the cryogenic supply. Figure 31 shows the cooling scheme of one feedbox which controls helium flowing to and from coil cryostats of dipole magnets.

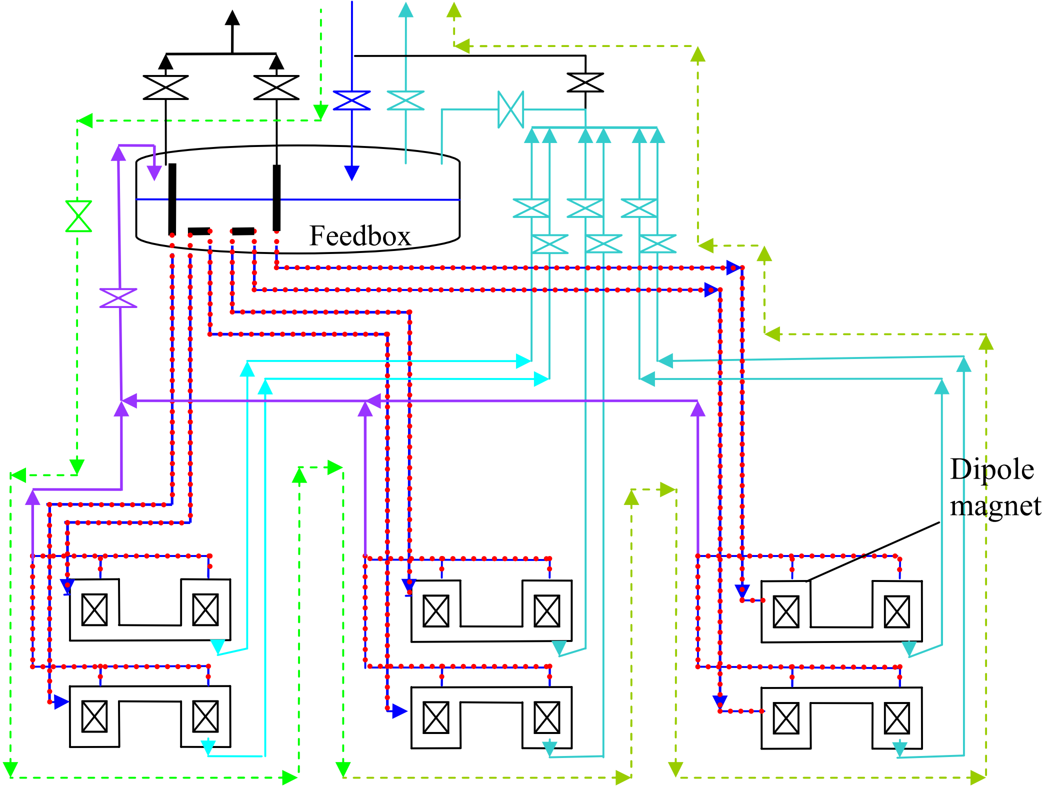

Figure 31: Scheme of the cryogenic distribution system for three Super-FRS dipole magnets and the feedbox

To connect electrically the three dipole magnets in one magnet group in series, superconducting bus bars are used to bridge the dipole magnets through the liquid helium supply lines and the helium bath in the feedbox. Thus a pair of vapor cooled current leads is needed only for the three dipole magnets. With the adoption of hybrid high Tc current leads the refrigeration load for current lead cooling could be further reduced.

There are superconducting quadrupole magnets placed in between two groups of dipole magnets. Three quadrupole magnets rigidly connected as a triplet are installed in a helium vessel in a single cryostat, cooled in a bath of liquid helium. Two types of superconducting quadrupole magnets will be used: an iron-dominated type (superferric) and an air-core type. The quadrupole triplets in the second half of the Pre-Separator and in the Main-Separator have superferric design with cold iron and warm bore. Thus high cooling capacity is required to cool down such triplets. On the other hand, the fine focusing in front of the production target is of cos(2θ) type which has much less cold-mass. This helps to reduce a significant amount of heat load at 4.5 K in the cryostats under the exposure of high radiation in the first half of the Pre-Separator. However, a much higher heat load due to the neutron radiation is still foreseen in the first four quadrupole triplets.

In accordance of using a scheme with the large cooling capacity requirements, it is planned to use the same cryogenic distribution line for all the superconducting dipole magnets and quadrupole triplets. It is foreseen that one individual feedbox controls the liquid helium distribution of several quadrupole triplets. *Figure 32* shows the flow control scheme of two neighboring quadrupole triplets in one focal plane and the corresponding feedbox for the cryogenic supply.

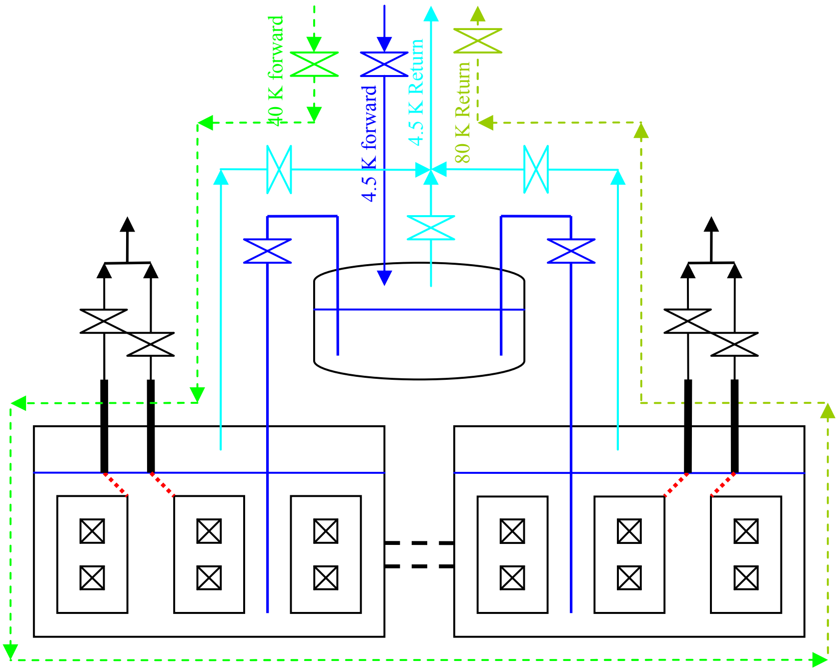

Figure 32: Cryogenic supply for two neighboring quadrupole triplets at one focal plane.

Figure 33 shows the layout of the cryogenic distribution system for all the superconducting magnets in the Super-FRS. This scheme facilitates the cooling capacity control and maintenance in the first half of the Pre-Separator with the help of the intermediate joint box.

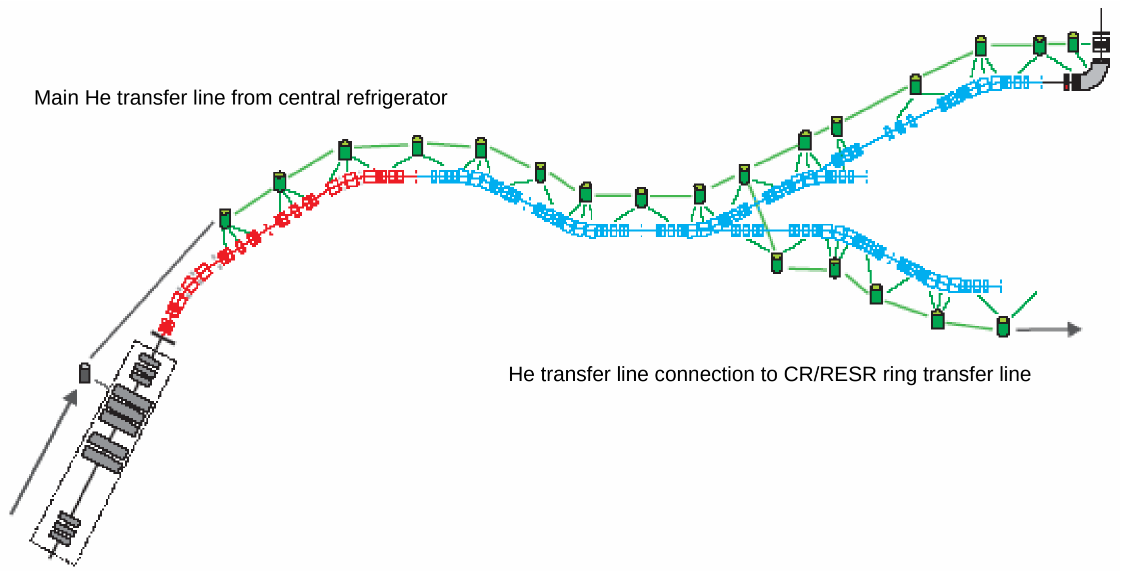

Figure 33 Layout of cryogenic distribution for the Super-FRS.

R&D phase of Super-FRS cryogenics

In the first part of the Pre-Separator, radiation-hard design is required not only for the magnets but also for all other devices, e.g., cryogenic instrumentation and cabling, actuator of control valves, cryogenic seals and fittings, and thermal insulation material in the cryogenic system. Therefore, R&D work to investigate the radiation impact on the lifetime of the cryogenic distribution system is necessary.

2.3.6 Survey and alignment for the Super-FRS

An accurate alignment of the Super-FRS components is important for good ion-optical resolution and transmission. It has to be pointed out that it is not only necessary to perform an exact alignment initially, but also to maintain and to check the position accuracy for a long period of time. For the initial installation of Super-FRS it is assumed to have the same conditions like for the storage rings and beam lines. R&D effort is required for the fiducialization concerning finding the axis. However, the Super-FRS tunnel is difficult to access for maintenance after activation. Therefore it is necessary to use automated, remote systems for position control and realignment within these zones.

A recently started R&D project called RALF (**R**emote **AL**ignment on the **F**ly) deals with the conceptual work on an approach for a high-precision survey and alignment system in inaccessible, high-radiation areas. The new measurement system has to meet the following requirements:

- No access of human personnel
- Required accuracy of about 1/10 mm
- Fast data acquisition

- Automated, remotely controlled adjustment of Super-FRS components
- Handling a nonlinear beamline with a length up to several 10th of meter

The method will not be used as a permanent monitor system but for regular check of the actual condition.

Status of survey and alignment in high-radiation environment with RALF

The ideas are based on a photogrammetric solution: close-range photogrammetry is the only non-contact geodetic measurement technique that works without human impact on the object and accomplishes flexible measurement and monitoring tasks with highest accuracies.

The approach relies on a number of high-precision digital cameras together with inclinometers that are installed on an automated guided vehicle system. Via tracks this device will be driven along the beam line in the activated area, which has to be surveyed. Appropriate fiducial points are mounted on the magnets / cryostats. In addition, photogrammetric tie-points and calibrated scale-bars are distributed in object space to guarantee a stable photogrammetric network. At least two adjacent components are captured in one shot, before the vehicle starts to move to the next stop for taking the following picture. After finishing with data acquisition the camera system is removed from the radiation-protected area into storage room to download the image data.

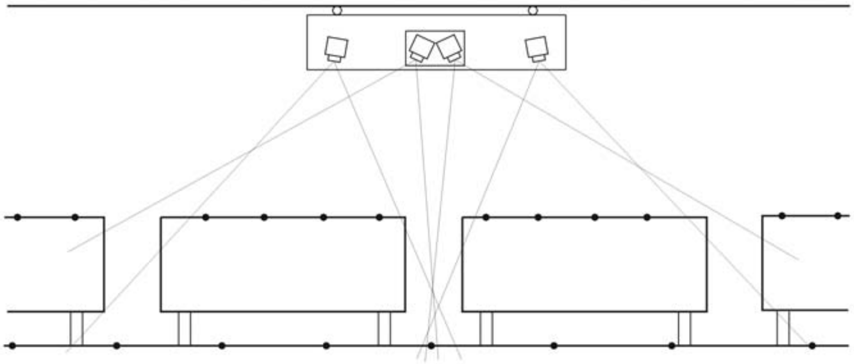

Figure 34: Present concept of the proposed surveying and alignment system RALF.

2.3.7 Cost estimates for magnets and power supplies

Magnet cost estimate	Quantity		
Dipole magnets (Pre-Separator I, rad. resistant)	3		
Dipole magnets (Pre- & Main Separator)	24		
Dipole magnets (Energy-Buncher, superferric)	4		
Quadrupole (rad. resistant, Pre-Separator I)	2		
Quadrupole triplet (standard)	17		
Quadrupole triplet (long)	3		
Quadrupole doublet (Energy Buncher)	1		
Quadrupole triplet (Energy Buncher)	1		
Hexapole magnets (radiation resistant, Pre-Separator I)	1		
Hexapole magnets (Separator & Energy Buncher)	39		
Octupole correction coils	40		
Steerer magnets	8		
Cryo feedboxes	21		
Cryogenic transfer line (280 m)	280		
Magnet support	54		
Magnetic field control	31		
Alignement (initial installation)			
Total costs			

Power-supply cost	Quantity		
Dipole magnets (Pre-Separator I, radiation resistant)	1		
Dipole magnets (Pre- & Main Separator)	8		
Dipole magnets (Energy-Buncher, superferric)	1		
Quadrupole (radiation resistant, Pre-Separator I)	2		
Quadrupole (short)	34		
Quadrupole (long)	26		
Quadrupole (Energy Buncher)	5		
Hexapole magnet (radiation resistant, Pre-Separator I)	1		
Hexapole magnets	39		
Octupole correction coils	40		
Steerer magnets	8		
Infrastructure (bridges, cable, distribution, trafo)			
Total costs			

2.4 Beam dumps

The beam dump serves two purposes, firstly to absorb the main part of the primary beam energy and secondly to shield the subsequent parts of the separator from a high level of secondary radiation. The challenge is to solve the technical problems due to the specific energy deposition of the heavy ions up to uranium for fast and slow extraction modes as outlined in the context of the production target in chapter 2.2. However, most of the kinetic energy of the heavy ions has to be absorbed by the beam dump system, whereas in the production target only about 10% is lost. For fast extracted uranium ions at 1.5 GeV/u the beam energy of up to 58kJ is deposited in one pulse of 50ns.

2.4.1 Position of beam dump

Dumping the primary beam within a magnetic separator requires special considerations. Depending on the magnetic rigidity (Bρ) of the selected fragments the primary beam may be deflected over a wide range of positions. The position in the first dispersive separator section can be characterized by the relative Bρ difference to the fragment beam, $\delta_p = B\rho_{prim} / B\rho_{frag} - 1$. The goal is to catch the primary beam behind the production target in beam dumps positioned outside of the magnetic elements at both sides of the optical axis depending if neutron-rich or neutron-deficient fragments are separated.

Detailed ion-optical calculations including nuclear and atomic interactions demonstrate that the beam dump must cover a range from δ_p = -30% to +30% for heavy ion beams up to uranium and up to 50% for very light ions (Z<9). Finally the situation due to possible failures of the magnet power supplies must be covered by the beam dump system.

These requirements can be fulfilled by a special layout of the first half of the Pre-Separator consisting of split dipole magnets with subsequent beam dumps, see Figure 5. Each dump covers a certain range of δ_p as illustrated in Figure 35.

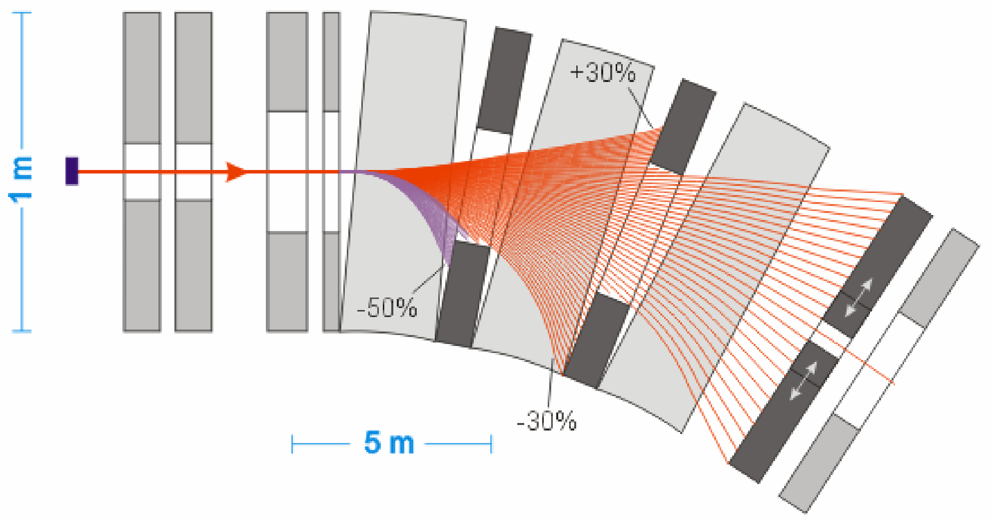

Figure 35: Trajectories of primary beams with different δ_p in steps of 1% calculated with the ion-optical program GICO [29]. The red rays represent possible separation scenarios for uranium beams and the violet rays hold for lighter ions with Z<9 to produce neutron-rich fragments. Note that due to the different scales in longitudinal and transverse direction the angles are not conformally represented.

2.4.2 Separation of fragment beams

Many Monte Carlo simulations of the primary and fragment beam distributions with the program MOCADI [30] were performed to make sure that the beam-dump system is universal for exotic nuclear beam experiments. A special challenge is to cope with heavy primary beams still carrying electrons after penetration through the target. An example is presented in Figure 36 for a ^{238}U beam after hitting a 4g/cm^2 lithium target at 1500 MeV/u. The Super-FRS is set to separate ^{132}Sn fission fragments and the primary beam still populates mainly 3 charge states, 92^+, 91^+ and 90^+.
In principle, the efficient separation scheme relies on a large Bρ difference between the primary beam and the fragment beam, but in this case the beam dump will reduce also the transmission of the selected fragments.

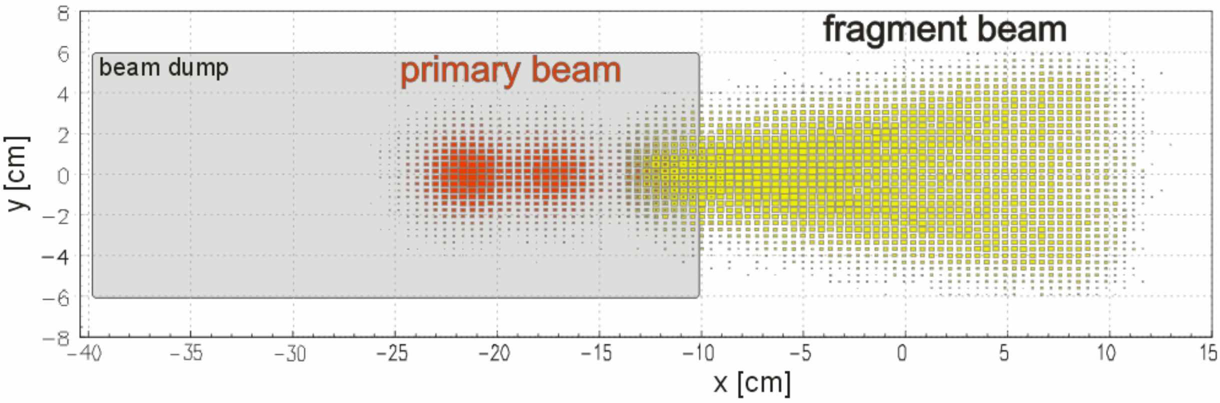

Figure 36: Calculated beam spots of the ^{238}U primary beam with three atomic charge states and of the fragment beam ^{132}Sn. The beam dump is moved in from the left hand side to catch the primary beam.

Crucial for the layout of the beam dump is the spot size of the primary beam which determines the temperature. The two different extraction modes will be treated separately but it is assumed for both cases that the beam spot at the target is σ_x=1mm and σ_y=2mm.
The fast extracted primary beam is characterized by a much larger phase space volume, see chapter 2.1, which results in favorably large beam spots at the dump. For the fast extraction mode with σ_p/p of 0.25% and the example in Figure 36 the calculated projections of the beam size in horizontal (x) and vertical direction (y) are shown in Figure 37.

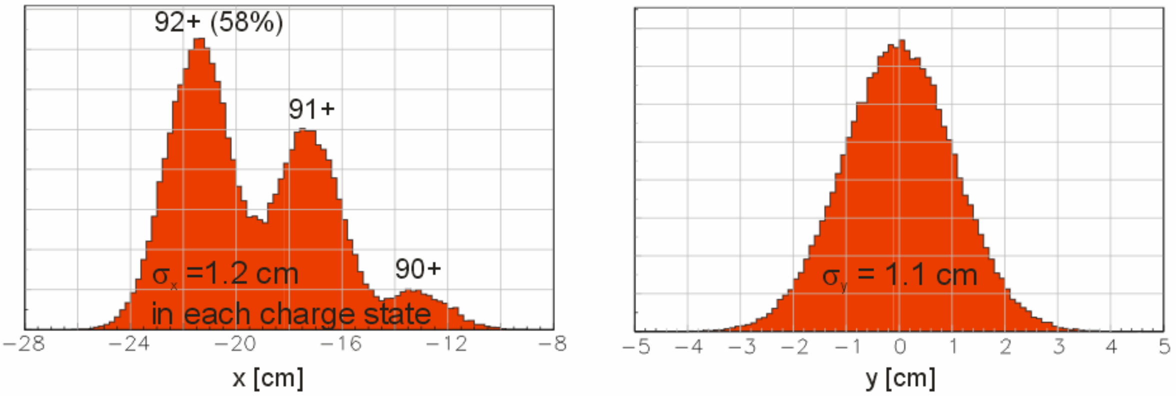

Figure 37: Spot size of the uranium primary beam at the beam dump at PF1 in horizontal (left) and vertical (right) direction in fast extraction mode. The peaks are projections of the distributions in Figure 36.

A beam dumped at an earlier stage in the Pre-Separator has less dispersion, but this is compensated by less focusing and thus results in a similar spot size. In general, the spot size in the fast extraction regime never becomes less than 1.0 cm^2 defined as a 1σ level.

For slow extraction, the initial emittance is much smaller but the nuclear and atomic interactions in the target cause a spot size for different δ_p between 0.25 and 0.5 cm^2 at the beam dump.

2.4.3 Beam parameters

The layout of the beam dump system is determined by the goals to provide safe and efficient operating conditions including maintenance requirements. Furthermore, it needs a well-defined operating range and interlock system. The choice of the relevant parameters is given below.

The maximal beam energy is limited to 1500 MeV/u for the heaviest ions at maximum intensity, whereas for light ions one can safely go up to 2700 MeV/u. For the minimum operating energy one has to consider to stay in the favorable ratio of the atomic and nuclear interaction length, which considerable reduces the effective Bragg peak in the stopping power. This condition is relatively easy to achieve for the critical case of fast extraction due to the fixed operating domain of the collector ring CR, i.e. the stochastic cooling requires 740 MeV/u and the operation in the isochronous mode 782 MeV/u. For the allowed energy range of slowly extracted beams one has only the restriction that the energy loss of the primary beam in the target causes that the beam is stopped in front of the first beam dump.

In general, the beam dump consists of a layer of light (e.g. Li) and heavy (e.g. Fe) material. The calculated energy deposition is presented in Figure 38 for different projectiles at 1 GeV/u. The reduction of the energy deposition due to the formation of lighter-Z fragments is clearly demonstrated. The Bragg peak of uranium ions still represents the maximum of the curve, whereas the Bragg peak of xenon is still visible but it is not the maximum of the curve any more. For the case of argon ions the Bragg peak is completely washed out by nuclear interaction. At the entrance of the beam dump the energy deposition of uranium ions exceeds the lighter ones by far, but at larger penetration depth the situation is reversed due to nuclear reactions. For light fragments and neutrons no high-power catcher is needed and a denser material for better shielding can be applied as a component of the beam dump.

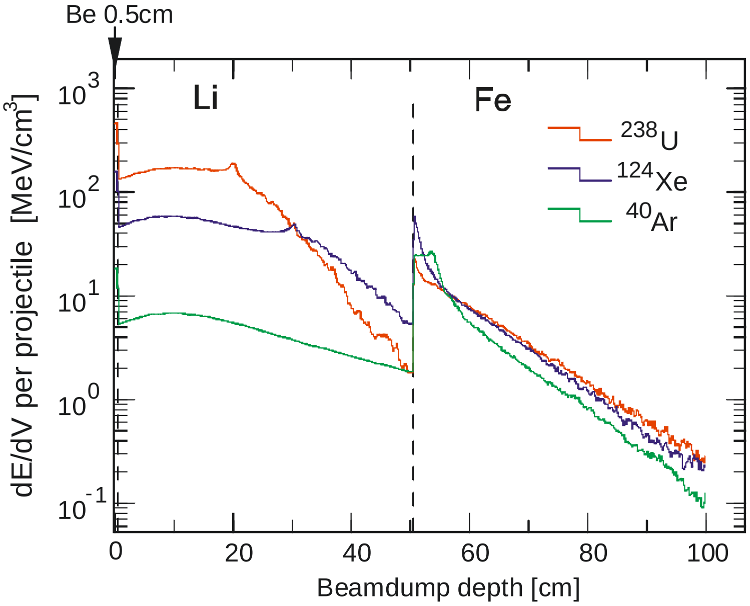

Figure 38: Deposited energy per 1000 MeV/u primary projectile and a 4cm^2 two dimensional Gaussian spot size for different ions, simulated with the PHITS code [31]. Here the high power part of the beam dump consists of lithium in a container with a beryllium window and the second half consists of iron. The jump in the curves is due to the different densities of the materials.

2.4.4 Choice of beam dump material

As already discussed the beam dump has two functions, energy absorption and shielding, which require the use two different kinds of material. In the first part of the beam dump, material with a low specific heat and low thermal expansion to avoid problems of melting and high pressure will be applied. In the second part material of higher density and Z will be used to achieve efficient radiation shielding in the limited space of the separator. All materials should be good heat conductors.

The entrance material should be low in mass number (A) to avoid too high temperatures. This can already be seen from the simple formula below for the temperature rise (ΔT) due to a number of particles (N) characterized by a stopping power dE/d(ρx), a beam spot area σ^2, and a molar heat capacity (C_{mol}).

$$\Delta T = N \frac{dE/d(\rho x)}{\sigma^2} \frac{A}{C_{mol}} \quad ; \qquad C_{mol} = 3N_A k_T \ for\ high\ T$$

As dE/d(ρx) changes moderately for different A and Z of the stopping materials, low A is clearly preferable.

Energy deposition in different materials

Besides the beam spot size the density of the deposited energy also depends on the amount of nuclear reactions of the primary beam. Simulations with the codes FLUKA [32] and PHITS [31] were performed to study the energy deposition taking into account both nuclear and atomic interactions and the contributions of the secondary beam. An example for 10^{12} uranium ions at 740 MeV/u dumped in carbon with a round Gaussian beam spot with σ of 1cm is shown in Figure 39. In

this calculation the initial energy spread was assumed to be zero. Without fragmentation the ratio of the stopping power at the entrance and in the Bragg peak would be 6.9 [33]. However, nuclear reactions reduce this ratio to 3.1.
In Li and Be the nuclear reaction rate is higher compared to the energy-loss cross section. Therefore, the Bragg peak would be reduced by an even larger factor. Values are listed in Table 14. The same conclusions hold for higher initial energies.

The density of energy deposition in the bulk material can also be reduced by geometrical shaping of the entrance of the beam dump such that the range straggling is enhanced. In the example of Figure 39 the ratio of the peak to entrance energy deposition has been reduced to about 1.8 using an inclined surface with a slope of 0.1.

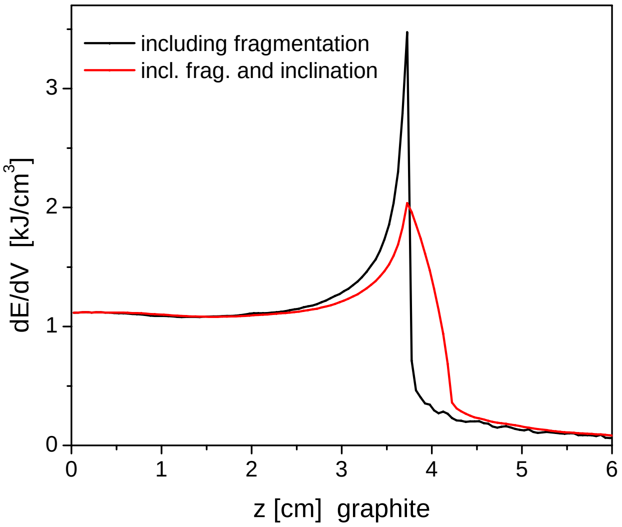

Figure 39: FLUKA [32] simulation of the energy deposition of a 740 MeV/u ^{238}U beam in graphite (ρ=1.84 g/cm^3) with a round Gaussian beam spot size with σ=1cm . The ratio of dE/dV at the entrance compared to the peak is only 3.1 compared to 6.9 [33] without nuclear reactions. An inclined entrance with slope 0.1 further reduces this ratio to only 1.8.

Table 14: Stopping powers at an energy of 740 MeV/u at the entrance of the beam dump, maximum energy deposition including fragmentation and the broadening due to the inclined surface with slope 0.1 in the Bragg peak, the initial temperature (T_i) and the resulting temperature (ΔT) and pressure rise(ΔP) in Li, Be, graphite and water for 10^{12} uranium ions instantaneously dumped with a spot size of 1 cm^2 (1σ of Gaussian distribution).

Material	dE/d(ρx) [MeV/mg cm^{-2}]	dE/d(ρx)$_{eff}$ [MeV/mg cm^{-2}]	T_i [K]	ΔT [K]	ΔP [MPa]
Li	18.0	25	490	175	460
Be	17.6	25	293	320	1420
C (graphite[1])	19.4	36	773	475	42
H_2O	22.1	32	293	200	780

---

[1] Values based on SGL carbon group grade R 6650 and ref [34]

In Table 14 the stopping powers and the resulting temperature and pressure rises are compared for different materials. Li has the lowest mass number and therefore the temperature rise has the lowest value. Beryllium and graphite have a rather high Debye temperature and do not reach their full heat capacity at room temperature.

The pressure rise of 1.4Pa exceeds even the tensile limit of beryllium. Beryllium can therefore not be used. As a consequence this prevents a solution of liquid lithium with a Be entrance window. Li cannot be used in combination with carbon due to chemical reactions. Only a windowless lithium beam dump could in principle satisfy the requirements. Considering the low density of Li of 0.54 g/cm^3 the dump would be about 50cm long, at least 20cm wide resulting in a required flow of about 1m^3/s of liquid lithium that would have to be pumped. Such a realization would comprise many technical problems.

The properties of diamond as a beam dump material would be ideal but by far too expensive. However, the derivate graphite is also suitable. The temperature in graphite is tolerable, the pressure is low because of the low bulk modulus and suitable for a long-term operation. Water would be evaporated in the hot spot of the beam and is therefore not suited directly as a beam dump but may be favorably used for cooling the solid material.

The values for graphite listed above will be lower in a realistic running scenario where a target with 10% reaction probability is usually applied. For the heaviest beams the population of several atomic charge states improves the conditions of energy deposition in the beam dump, cf. Table 15. The additional improvement due to the wedge-shaped entrance of the beam dump was already taken into account in Table 14. Under realistic operating conditions the initial temperature will be higher (~870 K) leading to a slightly increased heat capacity [34]. All these measures reduce the maximal instantaneous temperature rise for the graphite case, compared to Table 14, to $\Delta T = 186$K and the resulting pressure rise to $\Delta P = 17$ MPa when a 1300 MeV/u uranium beam is stopped in the beam dump at PF1.

Table 15: Equilibrium charge-state distribution of uranium ions after a carbon target as a function of specific energy according to the GLOBAL and CHARGE predictions [35].

Energy [MeV/u]	92+ [%]	91+ [%]	90+ [%]	89+ [%]	88+ [%]
1500	77.7	20.8	1.5	<0.01	
1000	58.0	35.9	6.1	<0.1	
750	41.9	45.7	12.2	0.2	<0.01
500	21.8	49.5	27.7	0.9	~0.01
250	4.0	30.6	59.7	5.5	0.2

2.4.5 Design of the beam dump

2.4.5.1 Graphite part

From the discussions above the preliminary design of the beam dump looks as follows: The entrance part of the beam consists of graphite whereas the second part is made of iron. Figure 40 shows a cut through the graphite part. The position of the water cooling pipes is indicated. The water flow goes directly through the graphite. Since the water-free region in vertical direction is 6cm only tails of the beam can be deposited directly in the water. The V-shape helps to bettter distribute the heat especially in the Bragg peak region, and increases the surface for better cooling. The iron part should be about 80cm long to sufficiently reduce the neutron radiation for the subsequent magnet coils. The transverse size needs to be 30cm to cover up to 5 significant charge states of uranium at the focal plane PF1, see Figure 37.

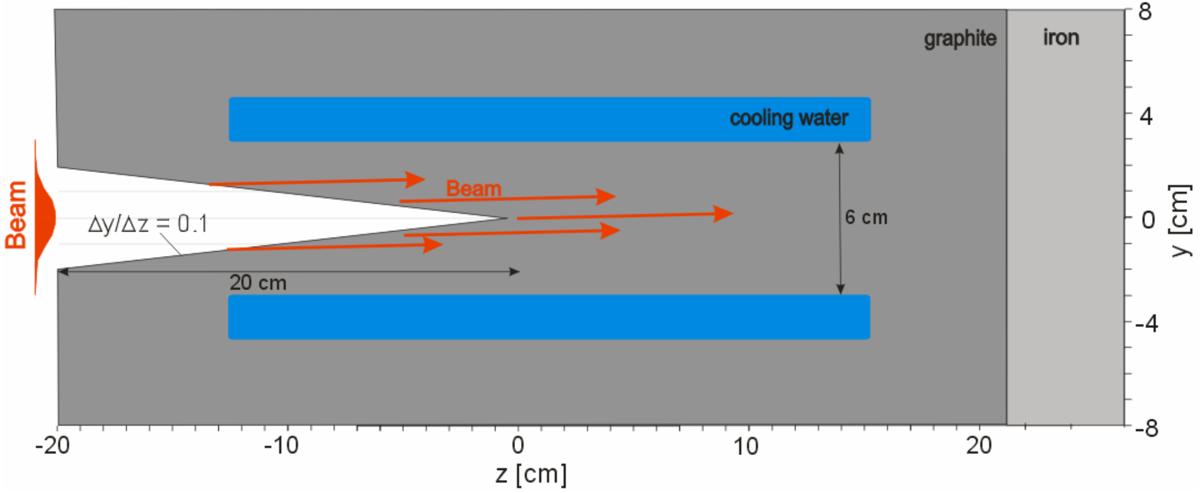

Figure 40: Cut through the water-cooled beam dump. The entrance part of the beam dump is made of graphite and the subsequent part of iron. The latter is only partially displayed in the scheme. The red arrows indicate the beam. Their lengths correspond to the mean atomic range of 1500 MeV/u uranium ions in graphite.

After an initial heating phase the temperature reaches its equilibrium. The equilibrium distribution was calculated using the ANSYS code [36] for the geometry depicted above. This simulation was done assuming a turbulent water flow in several cooling tubes. The profile of the power deposited was roughly adjusted to the fast extraction scheme as shown in Figure 37 and Figure 43. A volume with a spot size of 9x4.5 cm^2 and a depth of 9.1cm was heated homogenously with a total power of 51kW. Figure 41 shows that the maximum temperature in a small spot in the center of the beam dump becomes only 1160K in case of a DC beam. The walls of the cooling tubes stay below 100°C. The slow extraction mode would result in a smaller beam spot but a simple estimate of the heat diffusion time, following refs.[37,38], shows that the thermal diffusion time (t_D) can be fast enough to distribute the heat from a smaller volume, $t_D = \sigma^2 C_p \rho/(4\lambda)$. Here σ is the spot size, the specific heat C_p= 1.83 J kg^{-1} K^{-1} at 1100K, density ρ=1.84 g/cm^3 and the thermal conductivity λ=70 W $m^{-1}K^{-1}$. For σ = 0.5cm t_D becomes 0.28s. In case of 1cm it would be t_D=1.1s. This means that the temperature will not rise to values higher than in the fast extraction mode with a repetition rate of 1s.

The simulations also show that it is important for a tolerable maximum temperature in the center to have the cooling water close but not too close, to avoid boiling of the water on the walls of the hot tubes which would drastically reduce the heat transfer.

The heat coupling to the cooling tubes needs further investigations, for example how to guarantee enough turbulent flow and how to connect the cooling water to the graphite block. An alternative solution would be to install an aluminum tube in which the cooling water flows. In this case swirl tubes can be used providing a steady turbulent flow [39]. A prototype must be built and heated with external heat sources.

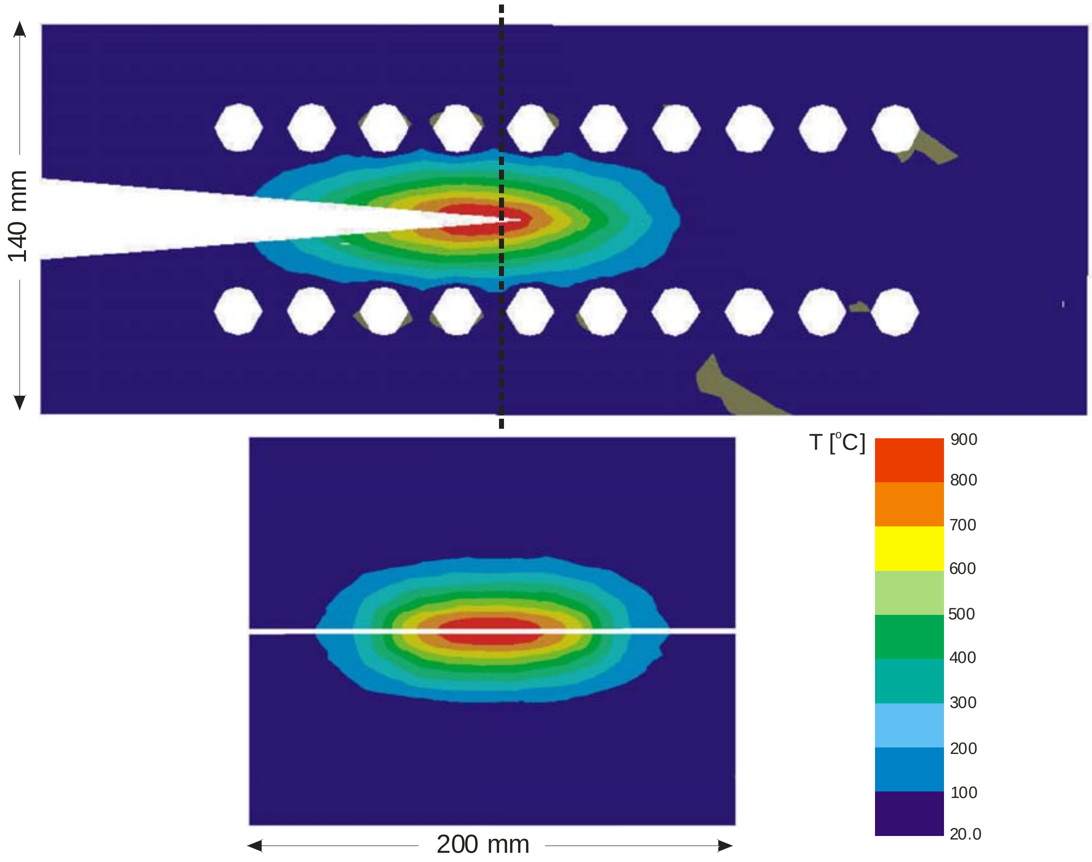

Figure 41: Calculated equilibrium temperature profile of the beam dump for an irradiation with a constant beam energy depositing of 51kW on a spot size of 9x4.5 cm^2 *up to a depth of 9.1cm. Top: cut through the center seen from the side. The holes represent the water channels for cooling. Bottom: cut through the central hot region seen from the front.*

In the DC mode the mechanical stress safely stays below the critical limits for a full graphite construction, see Figure 42. In the example shown the beam dump is free floating. Nevertheless the mounting should be done on a cold side which will not increase the stress too much.

In the fast extraction mode the shock from the instantaneous heating must be added on top of the pressure shown above. But as shown, this also does not exceed a few tens of MPa. In summary, we can stay below a critical limit for cyclic stress of ~60 MPa. Still pressure waves will propagate through the material. A simulation of the damping of such waves will be done.

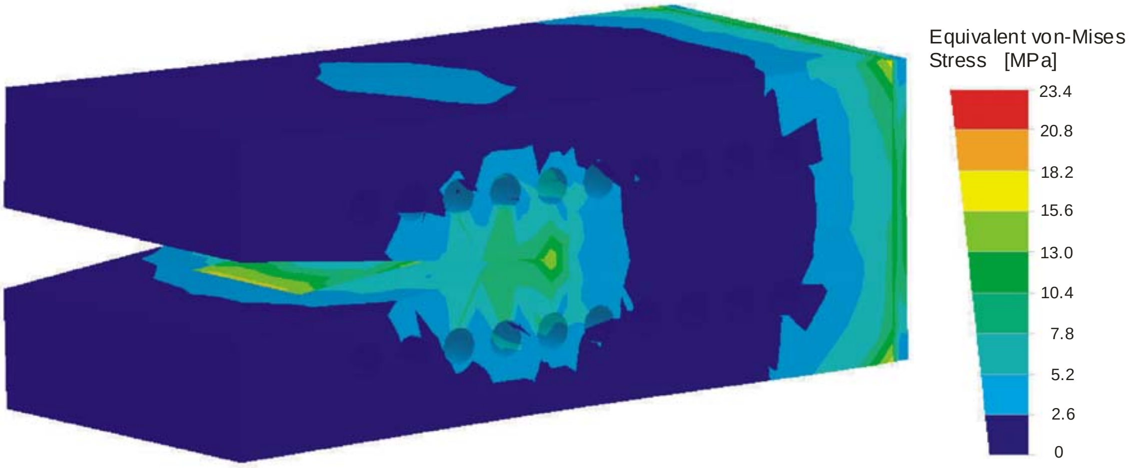

Figure 42: Mechanical stress (von Mises stress) on the graphite material in slow extraction mode after the central part has reached a temperature of 1160 K corresponding to Figure 41.

2.4.5.2 Iron part

After a certain distance in graphite the density of deposited energy becomes low enough to use iron as beam dump material. For example, after a penetration depth of 20cm of graphite the deposited energy per volume in the iron drops below 10 MeV/cm^3 per incident ion for a 1500 MeV/u uranium beam, see Figure 43. For 10^{12} ions in one fast spill this causes a temperature rise of at most 0.5 K which corresponds to a pressure rise of smaller than 3 MPa. Most of the energy is deposited in the carbon part but still the total heating of the iron can reach a power of the order of 10 kW. This requires water cooling of the iron as well.

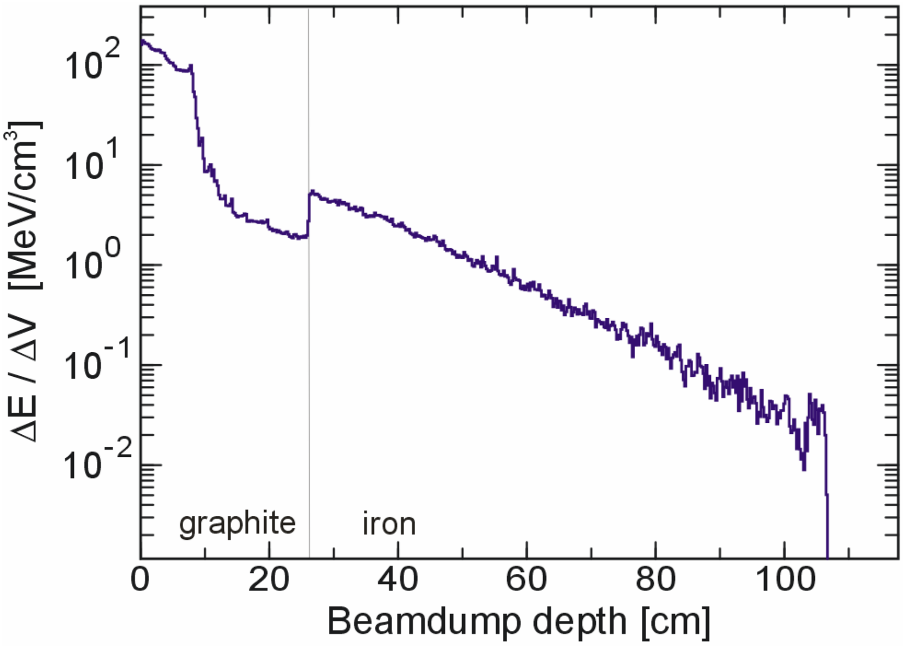

Figure 43: Energy deposition per volume in the carbon and iron part of the beam dump along the primary beam direction by a 1.5 GeV/u ^{238}U beam from a PHITS simulation.

There can be cases where not all high intensity components of the primary beam or fragments can be stopped in front of the degrader at PF2. This contribution should stay on a level of less than 1% of the full intensity of the primary beam to cause no damage in the degrader. However, the subsequent superconducting magnets have to be protected. Depending on the position and the energy loss in the degrader the magnetic rigidity of this beam can vary a lot in the second half of the Pre-Separator. Figure 44 shows possible trajectories and corresponding options for the beam dump locations. Like in the first half it is possible to find a setting of slits in which the beam is always dumped in a dedicated external catcher. At least after the slit at PF4 the total intensity must be reduced to an equivalent of 10^9 uranium ions at 1 GeV/u. Some of these slits need to be movable because they may otherwise restrict the fragment transmission. The construction of these beam catchers, however, is much more simple than in the first half of the Pre-Separator. Indeed they can be adopted from the present FRS slits.

From Figure 43 with the condition of 100 times less incoming beam intensity follows that the slits must have a thickness of about 30cm iron. As these slits are not radiated very often also higher density material (tungsten alloys) may be used without suffering from activation problems.

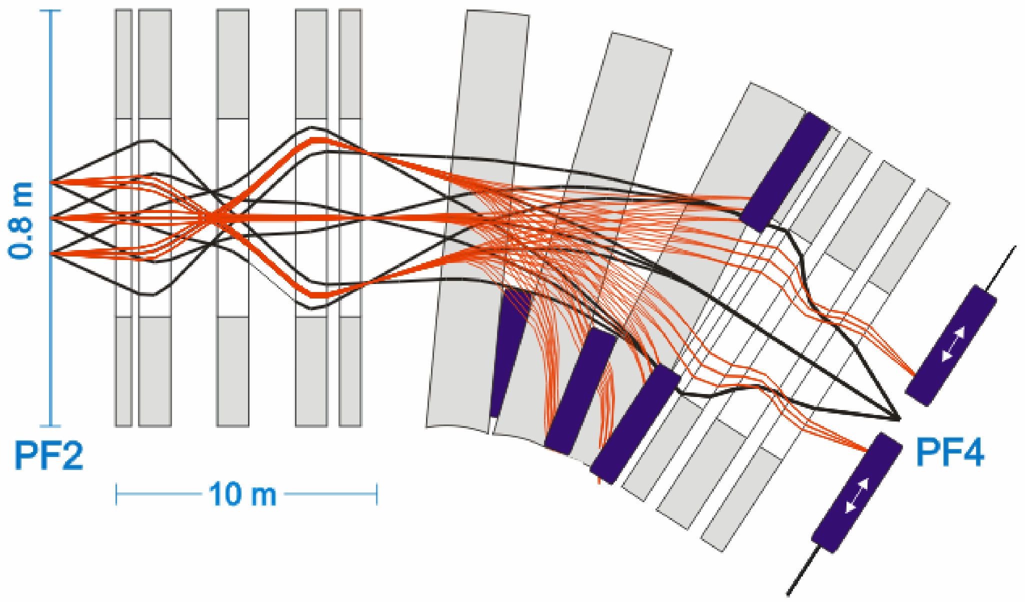

Figure 44: Location of beam dump positions behind the degrader station at PF2. Trajectories of the fragment beam are shown in black and possible trajectories of the primary beam in red. As the primary beam loses in most cases more energy than the fragments the beam dumps are needed mainly on one side.

2.4.6 Radiation damage

Radiation damage in the carbon part of the beam dump is caused by three mechanisms:

- Elastic collisions of the primary beam, fragments or neutrons with the carbon atoms.
- For high linear energy deposition the heating by the electronic energy loss can cause microscopic material melting and track formation. This happens in graphite above a threshold of dE/dx = 7.3±1.5 keV/nm [40] and will therefore occur only in the Bragg peak close to the

end of the range.
- Spallation of the nuclides and creation of other chemical elements.

The number of displacements per atom (DPA) resulting from elastic collisions was estimated with the PHITS code. The result is shown in Figure 45 as a function of the depth in the beam dump for a total number of ions of 10^{20} uranium ions, corresponding to 116 days of operation per year over 10 years with the full intensity and energy. A strong peak appears towards the end of the range in carbon near the maximum of nuclear energy loss. But as the range and beam position will vary in different experiments the number of DPAs will stay on average below 1.
Strong irradiation will also lead to heating and thereby annealing of the material. The semi empiric formula of Nickel [41] valid for heavy ions in the MeV range where most damage is created yields a result similar to PHITS. It also suggests a basic scaling of annealing of the graphite material as a function of temperature. Whereas almost no annealing will happen at room temperature, it predicts an enhancement of lifetime by a factor 50 with annealing at 1000K.
Due to the still widely unknown processes of track creation and annealing we cannot predict the expected lifetime of the device. For example, the track creation process leads at the same time to annealing. Considering only the damage by elastic collisions, the lifetime should be above 15 years, also comparing with the much higher number of DPAs caused by the intense PSI proton beam on the graphite target wheel [8].
The polycrystalline structure of the pressed graphite should tolerate rather high radiation damage. Heat conduction even improves in irradiated graphite, but this also means that some material transition definitely takes place.
The iron part is damaged mainly by fast neutrons. Here electronic energy loss plays no role. As shown in Figure 45 the number of DPAs stays below 1. This should allow operation over the whole lifetime of the Super-FRS.

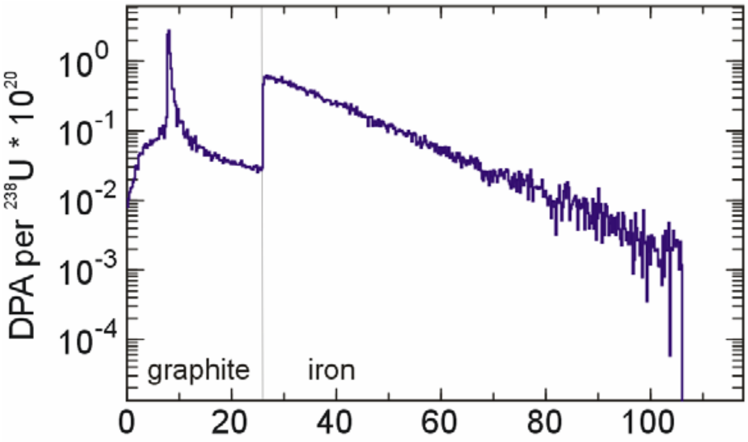

Figure 45:PHITS simulation of DPAs from elastic collision, all values stay below 1 DPA for the whole lifetime of the device even with full uranium beam intensity over 15 years with 77 days continuous operation in each year (10^{20} ions). The peak in carbon represents the end of the range near the maximum of nuclear stopping power.

From nuclear reactors it is well known that the material can also be modified by induced nuclear reactions. The amount of different elements created was calculated in a FLUKA simulation of the beam dump. Mainly helium is created in the graphite and the iron part. The ratio of atoms compared to carbon can reach 10^{-5} (10 appm) in the graphite and $3x10^{-6}$ (3 appm) in the iron after an assumed total irradiation by 10^{20} uranium ions considering that not always exactly the same spot is hit on the same beam dump. This may lead to swelling of the material.

In iron also a lot of metals close in atomic number are produced which cause no additional damage.

2.4.7 Activation

The PSI graphite wheel can serve as a reference for production of radionuclides in graphite [42]. In agreement with the FLUKA calculation they show mainly the production of ^{7}Be and ^{3}H. The FLUKA calculation for 100 days of irradiation with 10^{12} Uranium at 1.5 GeV/u and a following waiting time of 2 days shows an activation of $2x10^{12}$ Bq due to ^{7}Be and $9x10^{10}$ Bq due to ^{3}H. The resulting dose rate from the ^{7}Be activity in 1m distance is 15 mSv/h without shielding effects as defined in ref.[43], self-shielding by the carbon block reduces the value to 4 mSv/h. Even though most of the dose rate comes from ^{7}Be the long-lived gaseous tritium has to be considered for handling. The activity from other nuclides is many orders of magnitude lower and mainly due to trace elements in the carbon [42]. The activation of the cooling water is similar to the activation of the carbon. Again mainly ^{7}Be is produced but the amount of water in the beam dump is about a factor 10-100 less than carbon.

More serious is the iron part of the beam dump where more long-lived heavy nuclides are produced. Here the FLUKA simulation shows mainly the production of ^{46}Sc, ^{48}V, ^{51}Cr, ^{52}Mn, ^{54}Mn, and ^{56}Co with a total activity of $6*10^{13}$ Bq after the same scenario of 100 days of irradiation with 10^{12} uranium ions and a subsequent waiting time of 2 days. This corresponds to a total dose rate of 10 Sv/h at a distance of 1m caused almost entirely by gamma radiation. Self-shielding by the thick block of iron with a length of 20cm and an absorption length depending on gamma energy [44] reduces this value to about 1.3 Sv/h. A longer waiting time of 30 days would result in 330 mSv/h.

2.4.8 Handling, infrastructure

The dose rates mentioned above do not allow direct human access for maintenance. The plug system planned for the target will also be used for the beam dumps. The vacuum chamber at the exit of the dipole magnet needs to be very wide, cf. Figure 35. It is planned to incorporate the beam dump in the vacuum chamber for the dipole magnet. It also has to contain the iron shielding plug as usual vacuum seals can be used only on top of the plug. The whole setup of the three dipole magnets and the large vacuum chambers for the three beam dumps is shown in Figure 46.

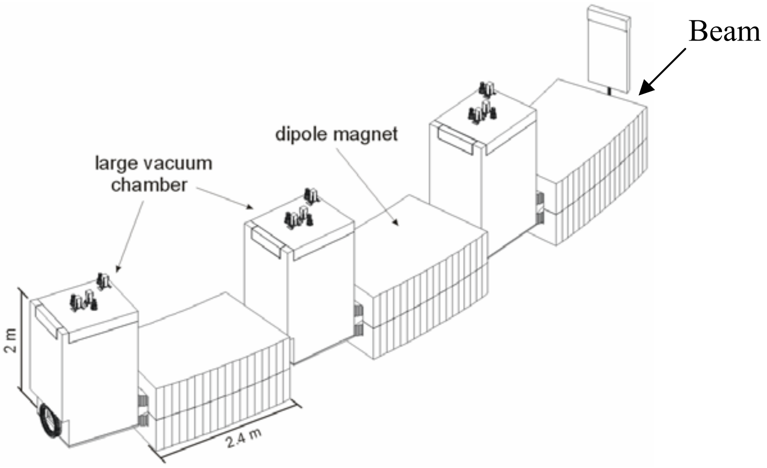

Figure 46: Layout of the beam dumps positioned behind each 11° dipole magnet of the Super-FRS.

A more detailed view of the plug and beam dump is given in Figure 47. Pillow seals will be used at the entrance of the dipole magnet and behind the beam dump where the aperture is small. Radiation shielding is provided by the iron plug inside the vacuum chamber or by surrounding concrete shielding. The beam dump and a position sensitive detector are mounted moveable on a rail and the corresponding motors are located on top of the plug.

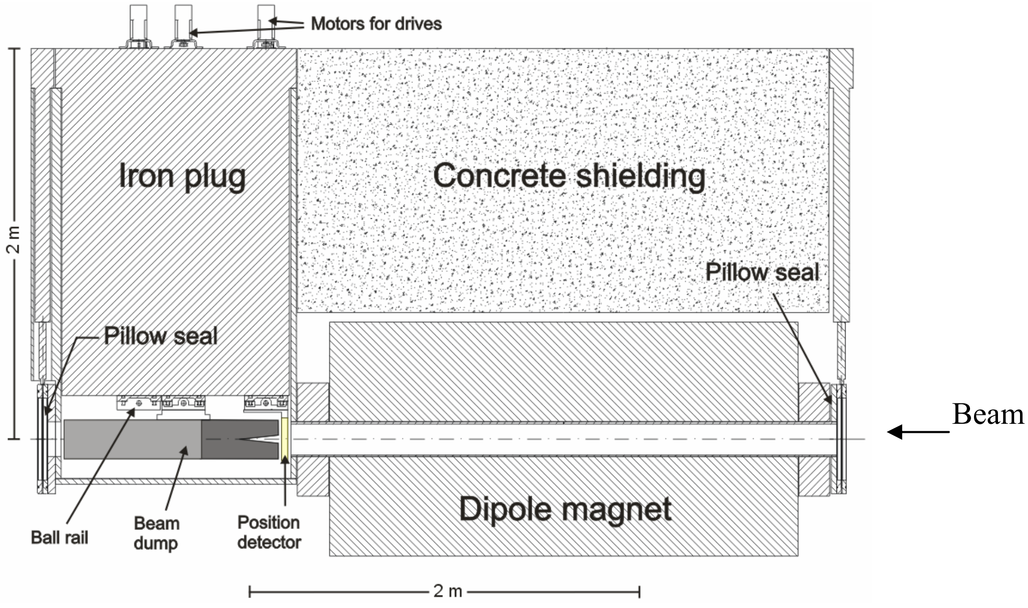

Figure 47 Scheme of the technical layout of the beam dump. Cut through the beam dump and the preceding dipole magnet.

For maintenance the beam dump must be removed first into a shielding bottle and carried to a safe deposit. As the dose rate with an iron bottle of 20cm thickness at the critical regions reaches about 100 μSv/h on the outside, it must be kept in an area with controlled access. A modification or

maintenance of the carbon is possible with manipulators after some decay time, whereas after long irradiation the iron part must be disposed of and can only be replaced completely.
As the total height of the whole slot is about 2.0m and the beam dump is about 100cm long and 30cm wide the total weight of the shielding bottle including the iron block in the slot reaches 20 tons. The cooling water must be kept in a closed circuit as it becomes activated. The heat exchanger capable of removing 60kW thus keeping the water at room temperature will be located at the top of the shielding plug in the maintenance tunnel. The water pipes lead through the plug. The water is not so much activated thus it is sufficient to place the heat exchanger behind an iron shielding of 10cm thickness.

2.4.9 Cost estimate for beam dumps

Beam dump cost estimate	Quantity		
Iron plug front part	6		
Iron plug back part	6		
Centering and guidance of plug	6		
Shaft drive and rail for beam dump	6		
Vacuum container with shaft feed through and guidance	6		
Carbon beam dump	6		
Iron beam dump	6		
Water cooling	6		
Rail drive for detector	3		
Feed through for cabling	3		
Heat exchanger	1		
Total costs			

2.5 Degrader systems and ion-catcher

The degrader systems are key components for the isotopically pure in-flight separation. Their effect and the ion-optical properties have been described in detail in refs. [45]. A newly implemented feature is the slowing-down, thermalization and post-acceleration of exotic nuclei employing a helium-filled stopping cell at the Low-Energy Branch. For this hybrid system, which will combine the advantages of the in-flight separation and isotope-separation on-line, a monoenergetic degrader system will be used. Existing techniques will be further developed and adapted to the performance of the Super-FRS. This concerns mainly the mechanical dimensions and thermal stress and radiation damage due to higher beam intensities. The numbers given in the following are based on calculations assuming the separation of exotic nuclei ranging from ^{11}Li up to ^{232}Rn. The range of specific kinetic energies and thicknesses is given in the following table.

	Thickness in units of range	Energy range (MeV/u)
PF2	0.1 ... 0.5	1000 ... 1500
MF2	0.1 ... 0.5	500 ... 1000
MF11	0.1 ... 1.0	100 ... 500

Figure 48 shows the generic concept of the degrader systems to be used at the central focal of the pre- and main-separator, PF2 and MF2, respectively, and at the final focal plane MF11 of the energy buncher. The unit consists of several components fulfilling different purposes: a rotational stage with two wedge-shaped disks of opposite rotation, thus allowing to vary the thickness continuously along the dispersive direction (indicated by the angle α), and two wedges moving linearly in opposite direction thus causing a continuously varying homogeneous thickness (d). In addition to that, homogeneous or wedge shaped pieces of material can be added (not shown in the figure) in order to provide larger thicknesses and/or angles.

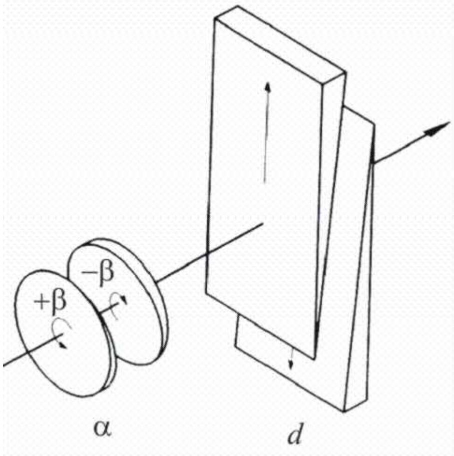

Figure 48: Schematic view of the degrader systems, which will be installed at the focal planes PF1, MF2, and MF11 of the Super-FRS. They consist of two rotating parts with wedge-shaped disks to generate the wedge-angle α and two linear drives equipped with rectangular wedges for the continuous thickness variation. Additional degrader plates may be added on an additional linear drive (not shown).

Detailed investigations [45,46] have been carried out to investigate the performance of a fragment separator employing a degrader system in dependence of the degrader material. These studies take into account nuclear absorption in the material, atomic processes like energy-loss straggling, small-angle scattering and charge-exchange, and the transport of the ions through the ion-optical system. Although for the lightest ions ($A<20$) a very light degrader material would be preferred, the overall optimum choice yielding high transmission for all nuclei is a medium-heavy element, like e.g. aluminum. Because of practical reasons, also quartz will be investigated (see below).

The energy spread additionally imposed on the fragments when penetrating through the degrader is the limiting factor of the resolution for the subsequent magnetic rigidity analysis. Thus it needs to be minimized and adjusted to the ion-optical resolution. Energy-loss straggling is unavoidable and thus the ultimate limitation. Practically, the main limitation arises from inhomogeneities and imperfect alignment of the degraders. The real shape of the degraders should match as good as possible the ideal shape, thickness non uniformities arising from inhomogeneous material (density) and/or surface inhomogeneities must be minimized. The tables given below show the tolerable values such, that the inhomogeneities cause the same width at the final focus as does the energy-loss straggling. These tolerances are of the order of few ten micrometer in order to preserve the ion-optical resolution, so that the degrader plates and the mechanical holders and drives require very high precision.

Because of the strong requirements, quality control is an important issue. Although several different manufacturers promise to fulfill the specifications (shape tolerances, surface uniformity,

density homogeneity), it has turned out that quality control needs to be done in-house. In the past years, the GSI target laboratory has developed tools to measure tolerances on a micrometer scale. The best results have been obtained with quartz material, which showed sub-micron surface tolerances and deviations from the ideal shape of very few microns only. Thus, from this point of view quartz is the preferred material. However, due to the manufacturing process, the minimum thickness is limited to values exceeding about 5 millimeters for each plate thus yielding at present only rather thick plates. In the near future we will explore other possibilities together with industry.
According to the specifications, the prototype system described in section 2.5.3 already reaches this precision. In an experiment we have tested Suprasil®-2 material (which is quartz-type material) and received the anticipated good results. The material is routinely manufactured with optical quality and exhibits a surface roughness of less than 10 nm, a maximum shape deviation of less than 1 µm and a material inhomogeneity less than 10^{-4}. Thus an areal weight homogeneity better than 0.2 mg/cm^2 is reached. Together with the prototype stepper motors and linear drives, a minimum thickness variation of 200 µg/cm^2 per step is achieved.

Concerning the ion-beam interaction with the degrader material, thermal and radiation damage issues are to be considered. The degrader unit of the pre-separator will receive the strongest load, and the worst case is a maximum intensity of 10^{10} uranium ions per second (resp. spill). Our calculations show that aluminum material will be heated by 8 K when the beam spot size has the expected dimensions of 4 cm^2. With 45 MPa, the pressure stays well below the cyclic stress limit of 290 MPa. The thermal diffusion time is of the order of 250 ms, thus well below the cycle time of the synchrotron. This time decreases linearly with the beam spot area, so that also for slow extractions no problems are expected. However, the numbers show that under continuous running conditions water cooling of the degrader of the Pre-Separator is required. The conditions will be similar to those which are presently prevailing in the FRS target area. In the considered energy domain of several 100 MeV/u elastic collisions leading to displacements and thus to radiation damage are of minor importance. Nevertheless it will be necessary to study whether such effects (like swelling, formation of bubbles, etc.) may occur after high-dose irradiations. This is an issue for the ongoing and coming development program.

For the degrader systems R&D is needed in order to further develop the existing technologies, e.g. to develop vacuum-compatible high-precision linear and rotational drives for degrader with areas which are larger than the ones which are operational now. Also the manufacturing and quality control of quartz-type degraders of the required dimensions is required.

2.5.1 Degrader system in the Pre-Separator

Width (cm)	Height (cm)	Thickness (g/cm^2)	Wedge angle (mrad)	Tolerances (µm)
15	5	1-10	0-120	120

2.5.2 Degrader system in the Main-Separator

Width (cm)	Height (cm)	Thickness (g/cm^2)	Wedge angle (mrad)	Tolerances (µm)
30	6	0.5-10	0-80	60

2.5.3 Degrader system in combination with the energy buncher

At the entrance of the Low-Energy Branch a particular and novel application using degraders is realized, an energy-buncher system. Its main components are a dispersive magnetic dipole stage and a monoenergetic degrader. It reduces the momentum spread of in-flight separated ion beams, usually of the order of several percent (±3% in case of the Super-FRS), down to values comparable to slowly extracted primary beams. Thus this scheme will be used to compress ("cool") the longitudinal emittance on a nanosecond timescale. It opens a new window to physics experiments with exotic nuclei: the energy-buncher stage will provide slow (Ekin ~ 100...1 MeV/u) monoenergetic (δE ~ 1 MeV/u) beams and will allow to stop exotic nuclei in very thin implantation arrays (~mg/cm2) or in helium-filled (gaseous or superfluid) stopping cells. From the latter, singly-charged ions of all elements can be extracted and post-accelerated to a few 10 keV for physics experiments (see section 2.5.4).

Adapted to the ion-optical parameters of the energy buncher, the calculated envelopes of the ion beams, and the properties during the slowing down, the following dimensions and tolerances have been calculated for the degrader system at focal plane MF11:

Width (cm)	Height (cm)	Thickness (g/cm^2)	Wedge angle (mrad)	Tolerances (µm)
60	20	0.5-20	0-120	140

Similar to the other focal planes, this unit will comprise wedges, disks, and homogeneous plates to yield the necessary flexibility. The large dimensions need special care. At present we are collecting information from different manufacturers who can provide all necessary plates with the required tolerances. A prototype is under development to gain experience and to test under realistic conditions at the FRS the performance and possible radiation damage or modifications of the material. Figure 49 shows the drawings and the first mechanical linear drives during assembly.

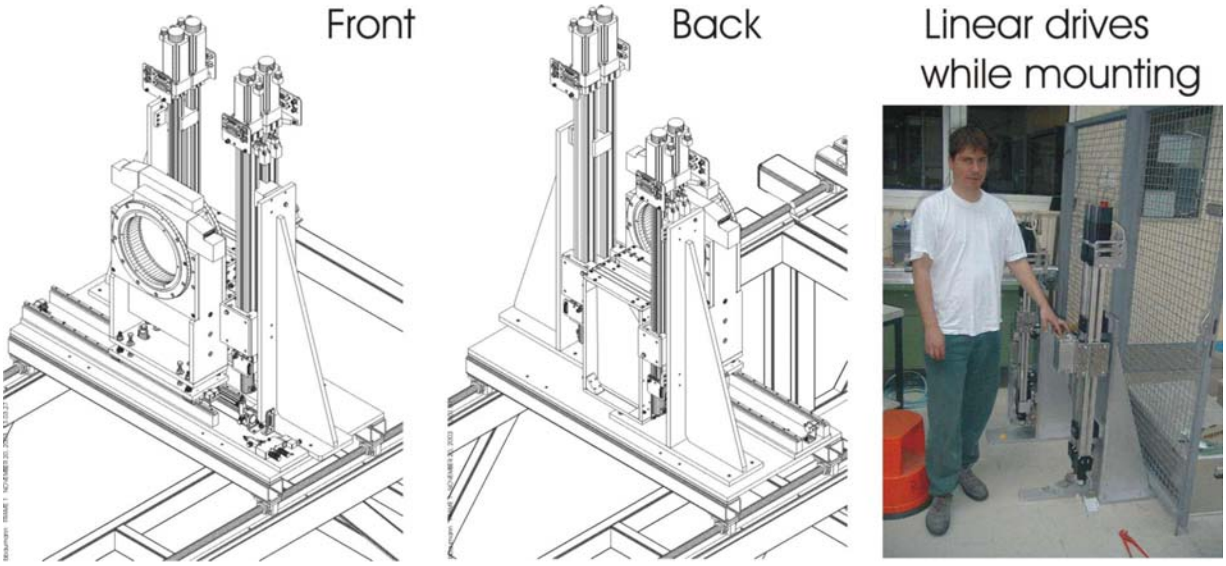

Figure 49: Drawings and first parts while mounting the prototype of the degrader for the energy buncher. This prototype will be used and tested for the FRS Ion Catcher setup.

2.5.4 Ion catcher

This stopping unit and its related components (beam extraction, cooling, bunching, and distribution system) as well the planned experiment is described in more detail in the section on the Low-Energy Branch.

For the Super-FRS Ion Catcher there is an R&D program already going on. *Figure 50* shows the prototype of an ion-catcher and beam-distribution system, which has been setup off-line and which will have its first on-line performance test with relativistic nickel ions in February 2005 at the FRS. Using an internal ^{252}Cf source for off-line tests, an efficiency of 10-20% has been determined for the full system. It is expected that singly-charged ions can be extracted on a timescale of a few milliseconds. Tests will be performed to find out possible high-intensity limitations due to space-charge effects. First on-line tests with a similar gas cell, operated at the MLL tandem accelerator at Munich, have shown the promising result that the overall efficiency of the stopping/extraction system stays constant up to intensities of a few 10^8 ^{107}Ag-ions per second [47]. This work is carried out within the European RTD network ION CATCHER and in collaboration with ANL Argonne, MSU, and Giessen University.

As an alternative approach, groups of JYFL Jyväskylä and KVI Groningen are developing and investigating the possibility to stop and extract exotic nuclei in/from superfluid liquid helium[48]. Similar extraction times and efficiencies as in the case of gaseous helium are expected, but the approximately 800 times higher density (as compared to gaseous helium at standard temperature and pressure) will allow for a much more compact apparatus. After thermalization in superfluid helium, positive ions form “snowballs” – clusters of helium atoms that form around positive ions due to electrostriction. Applying electrical drag fields, the snowballs drift to the superfluid helium surface and escape to the vapour region with high efficiency. In the near future further tests with improved setups are planned: off-line tests at KVI and on-line tests at JYFL. These studies will be further pursued as part of the European DIRAC design study.

Figure 50: Off-line setup of a high-pressure helium-filled stopping system for relativistic heavy ions. The present gas cell was constructed and assembled in Argonne (ANL) for tests relevant to the RIA and FAIR projects.

2.5.5 Cost estimates for degraders

Degrader & ioncatche cost estimate	Quantity		
Degrader plates(small, PF2 & MF2)	2		
Degrader plates (large, MF10)	1		
Linear drives (PF2, MF2, MF10)	3		
Rotational drives (PF2)	1		
Rotational drives (MF2)	1		
Rotational drives (MF10)	1		
Stopping cell, roots blower			
Gas system & vacuum components			
Beam extraction & distribution			
Diagnostic elements			
Total costs			

2.6 Detectors and data acquisition

Based on the operating experience gained at the FRS, we plan to implement a detection system that can be commonly used for all experiments at the different Super-FRS branches and comes with its associated data acquisition scheme. The main task of this combined system is threefold: (i) it can be used to set up and adjust the separator; (ii) it provides the necessary measures for machine safety and monitoring; (iii) it allows an event-by-event particle identification, tracking and characterization of the rare ion species produced. Furthermore, the beam intensities at different locations in the separator have to be monitored, e.g. as input for radiation safety interlocks as well as to normalize measured rates to extract absolute cross sections. The modi operandi depend strongly on these given tasks and the necessary requirements for the combined detector and acquisition systems will be given below:

(i) Setting up and adjusting the separator can be done at low rates for almost any detector system. The main design goal is to get a reliable system that is easy to maintain.

(ii) Online monitoring has to be performed, especially in the target and beam dump areas. Any deviation of the primary beam from its nominal position should lead immediately to an interlock. The main challenge is to cope with the very high intensities and background radiation here. The design of the detector systems should allow extended periods of operation without hands-on maintenance.

For almost all experiments, the separator is considered as the first part of the experimental setup. The ions entering the different branches have to be identified and their longitudinal and transverse momentum components have to be known. For tracking experiments to be carried out in the Low-Energy and the High-Energy Branches, the measurement has to be performed on an event-by-event basis. This implies that the data acquisition system of the particular experiments and the Super-FRS should be closely coupled if not identical. The Super-FRS data taking will therefore be designed in accordance with the common NUSTAR data acquisition scheme. The implication on the location of electronics and readout systems will be discussed in section 2.6.5. The requirements for detector systems are demanding at the entrance of the main separator, where rates of up to 10^9 particles /s can be expected.

The locations for the different detection systems are shown in Figure 51. The special conditions in the target area require a design of the detection systems that takes into account the radiation level of the area; it is foreseen to be able to run for about one year without opening the sections from PF0 to PF1. Generally we foresee UHV material although a pressure of 10^{-7} mbar is sufficient. The choice of the particular detector systems is driven by the idea trying to benefit from the various developments that are currently done in the detector laboratory (e.g. diamond detectors) and accelerator division (beam diagnostic systems) in conjunction with the FAIR project.

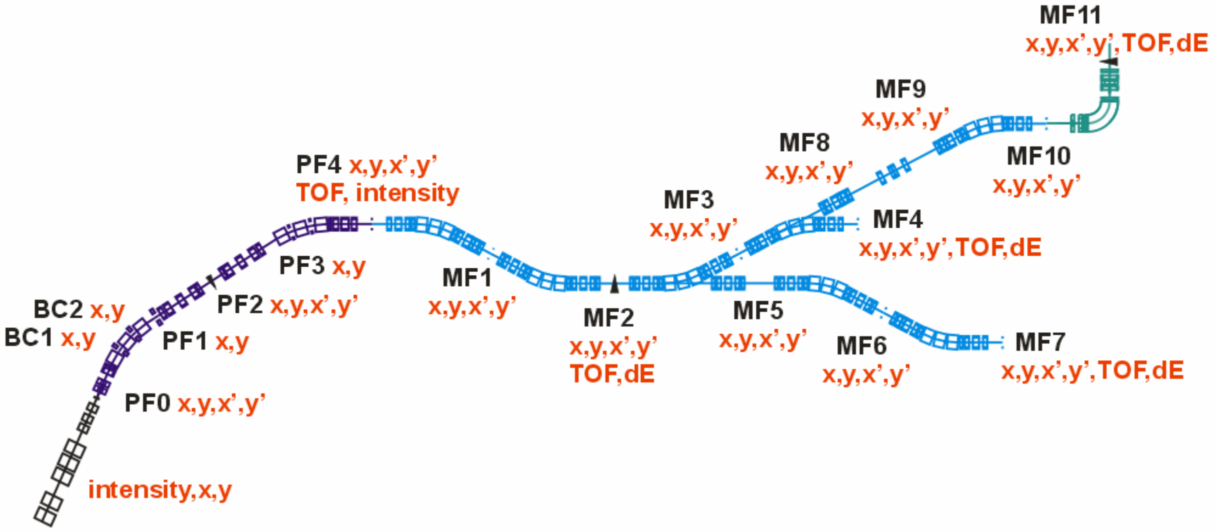

Figure 51: Detector systems at various positions in the Super-FRS. The individual areas and setups are described in the text. The letters "x,y" refer to position measurements in horizontal and vertical direction, x',y' to the corresponding angles. Energy deposition ΔE and time-of-flight (TOF) measurements are used for particle identification.

Radiation environment

The envisaged intensities of up to 10^{12} uranium ions per spill are demanding for the design of detector components in the first part of the Pre-Separator of the Super-FRS. As one can see in Figure 52 the minimum distance to the beam line where electronics components can be safely mounted is at about 1m radial distance. The end of the Pre-Separator (PF4) denotes the area where ion intensities are down to 10^9/s, comparable with the rates at the present FRS.

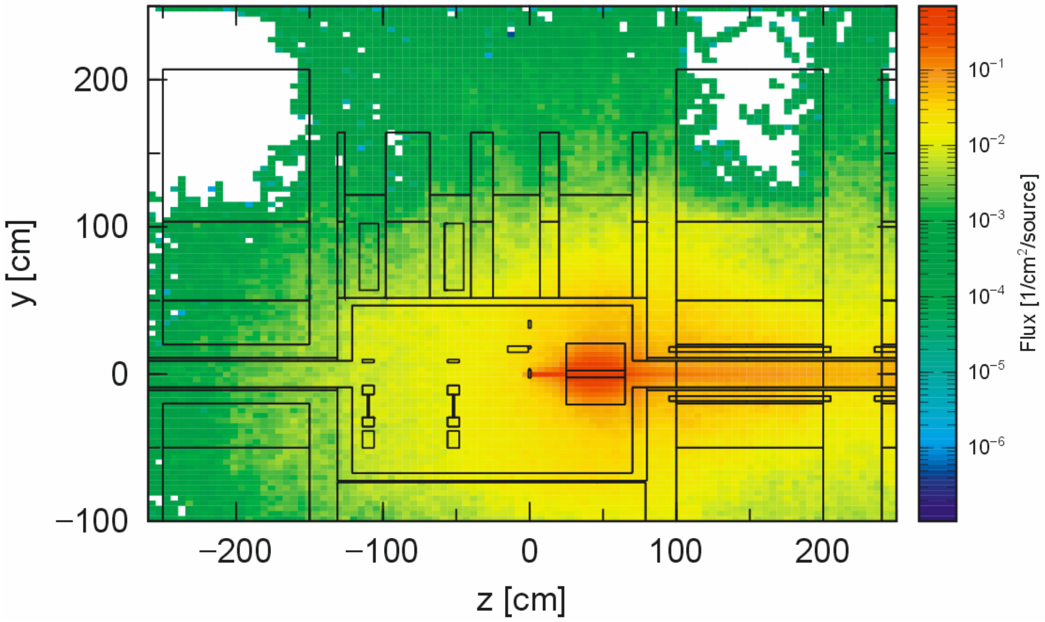

Figure 52: Total neutron flux (all energies) per incident particle in the target area of the Super-FRS (detector positions at z=-55 cm and z=-110 cm, target at z=0 cm, beam collimator starts at z=30 cm). The values are given for 1500 MeV/u ^{238}U ions hitting a 4 g/cm^2 carbon target. The material of the target chamber and nearby shielding is iron, the outside is concrete. All readout electronics should be placed at least 1m (y-direction) from the beam axis in the ladder drives (to stay below the limit of about 10^{15} neutrons/cm²).

2.6.1 Diagnostics target area and beam dumps

For the target and beam dump area it is foreseen to have a safety interlock on the nominal beam position on target and beam dump to avoid damage for any component in the high-radiation areas. It is clear, especially for fast extraction, that any detector material or foil will fail if hit by the full beam intensity. Therefore, contact-free measurements have to be used.

Target monitor

For monitoring the beam spot on target, an optical imaging technique in the infrared spectrum has to be developed together with the two types of targets. Since the camera has to be placed at a decent distance from the target to avoid radiation damage, a fibre or mirror optics has to be developed and tested. The camera images will be analyzed using standard image-processing techniques.
Another interesting method to visualize and monitor the beam spot on the target depends on the rest gas conditions. The induced fluorescence in the rest-gas volume can be used to deduce the profile of the incoming beam. This method has been successfully applied [49] at the UNILAC at GSI.

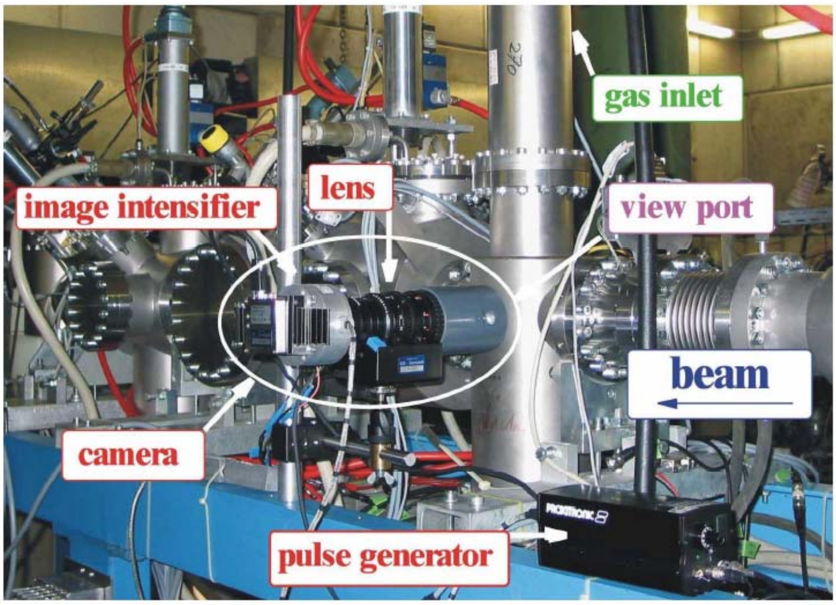

Figure 53: Beam-induced-fluorescence setup as used to measure beam profiles at the UNILAC accelerator. Uranium 28^+ *ions at 4.7 MeV/u with intensities of* 10^8 *-* 10^9 *ions per macro-pulse could be detected. For application in the Super-FRS camera and image intensifier have to be placed at a safe distance from the target and a suitable telescope or fibre optics has to be developed.*

Beam dump diagnostics system

The beam dumps of the system are described in section 2.4. It is desirable to perform on-line monitoring of the disposed intensity for security reasons. The simplest way would be to measure the transferred charge of the dumped ions directly by means of commercially available Ampere meters, i.e. use them like a Faraday cup. In practice, however, this method cannot be applied to these rather extended movable and cooled devices. Apart from the optical methods already mentioned, where one could monitor the deposition of the primary-beam intensity on the beam dump, there is another option that became available recently and is subject to intense ongoing development, namely diamond detectors.

Diamond has superior material properties -large thermal conductivity and high shock-wave resistance- that make it ideally suited for the hostile environment of the Pre-Separator. Commercially, artificially grown diamond films (CVD-D) are used as windows but became recently also available as detector materials. They are available as poly-crystalline (PC) or single-crystal (SC) films, depending on how close the substrate properties are to those of the diamond lattice. It has been demonstrated that PC-CVD-D detectors operating with low-noise low-impedance broadband amplifiers are able to measure linearly heavy ion rates in a broad range from 1 Hz up to >500 MHz by single particle readout of one detector channel. This value has been obtained with a detector of large capacitance of 8 pF and a scaler which limited the measurement due to its 500 MHz bandwidth. The single-particle count-rate capability is higher for reduced strip capacitance and GHz electronics signal processing [50]. If two-dimensional position resolution on thin detectors is needed, crossed strips can be applied on opposite sides of the diamond substrate. Note, that although this type of detector is of high interest for different experimental groups and the expectations for a successful realization are good, no such a detector has been developed up to now at GSI. Thus, joined R&D e.g. with the Atomic Physics and R³B collaborations is foreseen. Figure 54 shows the microscopic image of a pixel structure, which has been processed by sputtering a 1000 Å Si_3N_4 layer on a metallized surface. PC-CVD-D micro-strip and micro-pixel detectors have been developed (*Figure 55*) and excessively tested by the RD42 Collaboration at CERN [51] (GSI is a member).

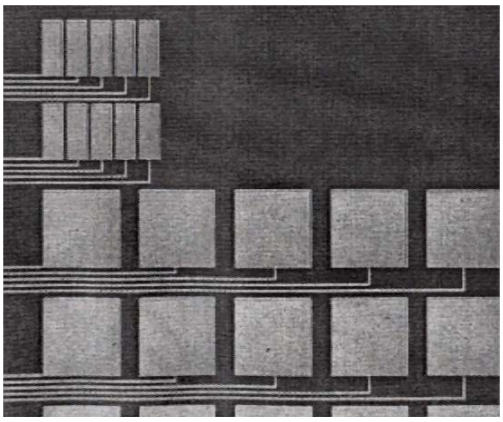

Figure 54: Pixel readout by Si_3N_4 - isolated micro tracks. Microscopic image of a pixel structure on a 1.3μm thick diamond membrane. The small pixels are 110 x 290 μm^2 and the large ones 400 x 400 μm^2. The width of the tracks is 15 μm and their pitch is 30 μm.

For fast micro-electrode readout providing a large dynamic range as needed for HI measurements no suitable ASIC exists yet. For CBM at FAIR, solutions are currently developed which aim at reading out its diamond start detector, a 20x20 mm^2 micro-strip detector with 50 μm pitch and a strip width of 25 μm. This chip would fit also for beam monitoring and tracking at Super-FRS.

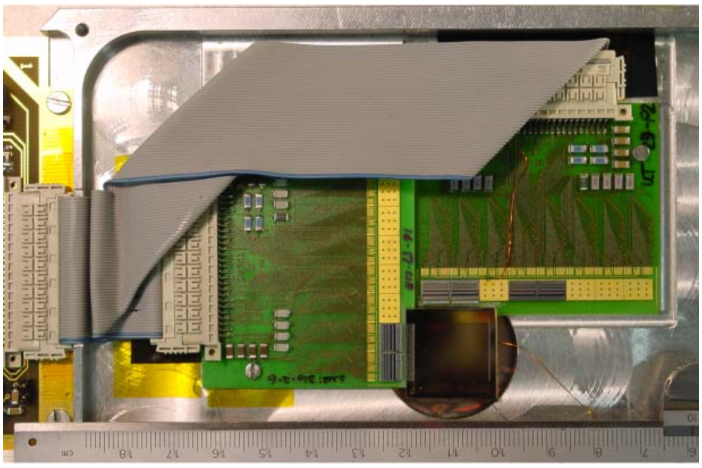

Figure 55: (RD42 collaboration). Two hybrids carrying PC diamond strip detectors and readout chips. The 2x2 cm² big sensors of a strip- and readout pitch of 50 μm are centered over a hole in the aluminum frame.

The expected radiation hardness of CVD diamond is the most important material property initiating the research and development of diamond detectors. For the tracking of minimum ionizing particles (mip) in the LHC experiments ATLAS and CMS [52] as well as for a variety of heavy ion

applications with high luminosity beams [53] diamond detectors have already been developed. In the case of mips no increase in leakage current and unchanged charge collection has been obtained for all kind of particles up to a fluence of about 10^{15} particles/cm². However, the heavy ion dose where damage of CVD diamond starts is still unknown. Currently, as a lower limit, about 10^{13} cm^{-2}, ^{12}C ions (at 1-2 GeV/u) and ^{131}Xe ions that were even stopped in the detector material have been already applied without any degradation of these detectors.
According to the fragment distribution as shown in Figure 36 we would expect an intensity of 10^{12} uranium ions on a 10x20 mm² area which corresponds to an annual dose of $10^{18}/(cm^2$ y). Our calculations have shown that the material as such will survive such intensities; the question to be investigated is now whether a thin detector film can stand such a dose without getting blind. The beam dump detector arrays would have an active area of 40x20 cm² made from the cheapest PC-CVD-D material. They will be freely movable over the full aperture of the Pre-Separator. A spatial resolution of about 1mm is considered to be ideal for monitoring the fragment distributions. It has been already demonstrated that the readout electronics can be safely placed about 1m away from the detector system without degradation of the electronic signals. However, a detailed study has to be performed how to build a 600 channel readout and cabling for these detectors.

2.6.2 Diagnostics for slowly extracted beams

We define slow extraction as extraction times that are above 100ms for the Super-FRS. Beam diagnostics systems will be installed at all intermediate foci PF0-4, MF1-12 with standardized active areas of 40x20cm² whenever possible (at MF11 90x20 cm² will be needed for the LEB). Two systems each will be placed at PF0,2,4 and MF1-12 to allow angular measurements. At intensities above 1 nA in the Pre-Separator, beam-induced fluorescence (see section 2.6.1) has to be used. If the energy deposit per mm will stay below 100mW, current grids [54] are routinely used to measure beam profiles. At even lower intensities (<100 kHz) usual multi-wire chambers or GEMs [55] with single-wire or single-pad front-end readout boards will be used to measure beam particles event-by-event, allowing tracking through the separator (see also section 2.6.5). This standard instrumentation is chosen for its moderate system cost. Whenever possible a continuous recording of the beam positions will be done to allow automatic steering of the beam to the nominal position.

2.6.3 Diagnostics for fast-extracted beams

For fast extraction and intensities above 1 nA, capacitive pickups [56] are routinely used at GSI to deduce the beam position for the ESR experiments. We will use these pickups for the Pre-Separator of the Super-FRS. The usual current grids and multi-wire chambers (see section 2.6.2) can be used to measure fast extracted beams at lower intensities. Recent investigations have shown that it is advantageous to operate the gas-filled current grids at reduced pressure or even without gas for fast extracted beams. This has to be taken into account in the design of the gas-supply system for the respective detector systems.

2.6.4 Luminosity monitor

We want to perform luminosity measurements at two positions in the Super-FRS: (i) at the very beginning in front of the quadrupole triplet prior to the target area; (ii) at the entrance of the main separator (PF4).

(i) The intensity of the primary beam delivered by SIS 12/18 or SIS 200/300 will be measured in a diagnosis box outside the target zone. The advantage of this arrangement is to have enhanced accessibility, and to keep the hot zone technically as simple as possible. Two ladders are foreseen in this diagnosis box, both containing detectors with active areas of 10x10 cm². The first ladder will be equipped with a Resonant Beam Transformer and a diamond counting detector. The second one houses a SEETRAM (Secondary Electron Emission TRAnsmission Monitor) counter and a Cryogenic Current Comparator. Resonant Beam Transformers [57] are the working horses at the current GSI facility. They can be used from 1nC up to 1µC with a resolution 10pC (rms) for bunches with a maximum pulse length of 1.5µs. Thus, they are perfectly suited for the detection of fast extracted pulses. Cryogenic Current Comparators are usable for DC currents down to about 100pA [58] and can be used for the slowly extracted beams. The SEETRAM counter [59] was developed for the FRS. Its operation is based on the emission of secondary electrons from thin metal foils by the passage of the projectiles. It can be used for slow and fast extracted beams. Its use for the Super-FRS is limited to intensities up to about $10^{10..11}$ particles/spill to avoid damage of the detector. The SEETRAM current is calibrated by directly counting individual ions. For the Super-FRS we will benefit from the high counting rates that can doubtlessly be handled by a diamond detector (10x10 cm², PC-CVC-DD (AG)). The diamond detector can also be used at reduced rates of $10^{9..10}$/spill – as has been done already for the SIS18 – to analyze the spill structure after slow extraction from the different SIS rings.

(ii) For the entrance of the main separator a SEETRAM counter and a diamond detector are planned to be used for the luminosity measurements. The diamond counter can be used (as shown in section 2.6.5) also as the start counter for a time-of-flight measurement. The expected spot size is here about 2x3 mm² as given by the magnification (M_x=2, M_y=1.5) of the Pre-Separator optics. With rates of up to 10^9 uranium ions this is just at the limit of what can be counted using a PC-CVD-DD. One may consider using single crystal material here. The recently available SC-CVD-D material is presently investigated by NoRHDia [60]. The charge collection efficiency of SC-CVD-D detectors amount to almost 100%, and the signal amplitudes are uniform over the detector area, which is not the case for PC-CVC-DD. However, due to much lower concentration of traps the detectors behave as fast drift chambers. Therefore, the count rate capability is lower and only 50 MHz are manageable. Instead of single particle counting one should investigate the possibility to perform a current measurement here, which becomes favorable due to the uniformity of the pulse heights.

2.6.5 In-flight fragment identification

Magnetic-rigidity measurements

The magnetic rigidity of an ion can be deduced from a position measurement in a dispersive plane. Two scenarios are considered: (a) determination during setup; (b) continuous monitoring. Option (a) requires a good knowledge of the relative magnetic field as a pilot beam is centered with known

Bρ and the measured B-field can be calibrated using an effective radius for the dipole magnets. Unknown magnetic rigidities can thus be determined. The centering process can be done at reduced rate using the standard detectors (see sections 2.6.2/3). Option (b) is more demanding but has been required by several NUSTAR experiments (e.g. the R^3B collaboration). The idea is here to gather additional information on the incoming beam by measuring its displacement in the dispersive plane (MF2) of the separator event-by-event. This method [61] has been successfully applied at the FRS to improve the mass resolution in the ALADIN-LAND reaction setup for fission fragments, by using a scintillator strip array (similar to the one shown in **Figure 56**). The granularity of the strip setup determines the maximum rate that can be dealt with (typically a few MHz/strip). The online monitoring of the stability of the separator settings will be used for feedback loops to perform e.g. automatic centering through the setup. This requires a combined analysis and simulation framework in order to be able to determine the offsets and compute the corrections. Here accelerator controls and Super-FRS instrumentation have to be coupled in the most efficient way.

Specific-energy-loss measurements

To achieve the required charge resolution via a specific-energy-loss measurement we consider MUSIC (multiple sampling ionization chamber [62] detectors as the optimal choice. These detectors can currently handle rates up to 200 kHz. There are developments underway to increase these rates up to a few MHz. These detectors, with active areas of 40x8 cm^2, will be inserted temporarily at the foci MF2, 4, 7, 10, and be operated continuously only at the final focal planes to identify fragments during experiments.

Time-of-Flight measurements

At present, plastic-scintillator detectors are being used in the FRS to perform the TOF measurements, leading to a rate restriction of a few MHz on the detector. In the dispersive plane of the FRS this problem can partly be overcome by using a segmented scintillator strip detector (see **Figure 56**). For the Super-FRS, we will investigate also the possible use of diamond detectors, providing both position information and timing signals at the MF2, 4, 7, 10 focal planes with active areas of 40x5 cm^2 and a pitch of 1 mm. For the rates foreseen these detectors would be optimal with respect to rate capability and radiation hardness. Using various heavy projectiles, the intrinsic time resolution of PC-CVD-DDs has been measured frequently to be well below 50 ps. Recently, the FOPI collaboration achieved a $\sigma_{intr} = 22$ ps with ^{181}Ta ions of 1 GeV/u. A similar value ($\sigma_{intr} = 29$ ps) has been measured in the HADES setup using ^{52}Cr ions of 650 MeV/u.

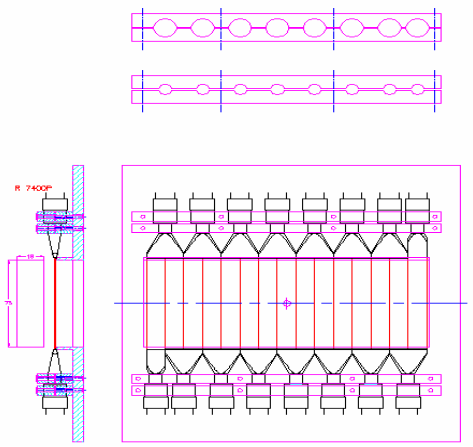

Figure 56: Finger strip detector consisting of 16 strips 73x14x10mm^3 plastic scintillator material read out with 16 Hamamatsu R7400P photo multipliers to be used at the FRS. For the Super-FRS the size and granularity of the detector system have to be adapted. The resolution in horizontal direction is given by the achievable $B\rho$ resolution with the dispersion at the different foci.

2.6.6 Data acquisition

The main task of the Super-FRS data acquisition (DAQ) is to provide on-line data about the production and separation process in the separator. It is clear from the beginning that there are rate limitations which will define the limit between event-by-event and integrated data. For different experiments in the experimental branches different classes of information are required.

Fragment Monitoring

For fast extraction, i.e. for the Ring-Branch experiments, only average properties of the pulses delivered to the CR/RESR/NESR complex are of interest. These are e.g.:

- intensity,
- charge and mass distributions,
- contaminants,
- deviations from nominal beam optics.

However, this is also the information that is needed as slow-control feedback data, which is described in the general NUSTAR DAQ section. These data will be collected by the local stand-alone Super-FRS DAQ together with an on-line analysis process that runs as a data server for the Super-FRS's slow control and the experiment bunch monitoring. The data server should provide a list of information it can deliver and provide a selection mechanism. Together with the information provided by the accelerator sections one is then able to monitor the full production process. This will also allow the accelerator controls to get specific feedback information from the experiments, allowing a very effective optimization of the setup data (see general NUSTAR-DAQ section). The necessary R&D will be done in close relation with the accelerator controls group.

Tracking experiments

Another class of experiments requires tracking of ions through the separator, e.g.:

- experiments performed at the final focus (MF4) of the Super-FRS, and
- experiments in the High-Energy Branch (R^{3}B).

Here the main issue is to obtain event-by-event information about individual particles through the setup. Since the fragment-selection process leads to substantial intensity-reduction factors (typically by 10^{-6} PF4 → Caves, and by 10^{-3} MF2 → Caves), coincidences have to be triggered at the end of the beam line. This means, especially for the diagnostic detectors at the entrance of the main separator, that at rates of several 10 MHz the spread in velocities for different isotopes with similar Bρ will lead to overlapping events. This problem corresponds to the task in high-energy physics of tracking particles with small yields while reconstructing their interaction vertices. Here this is usually overcome by storing the data first in the front-end electronics while subsequently transferring and reducing it in a multi-step triggering process. In our case this problem can be reduced to the problem of finding a plausible candidate in a certain time interval for an identified particle at one of the experiments.

There are several solutions, as discussed below, which have to be evaluated in close collaboration with the planned experiments:

(i) a suitable reduction rate can be achieved already by demanding a coincidence window, where events are taken. The particular coincidences are evaluated off-line.
(ii) Coincidences are fully evaluated on-line.

Option (i) can be realized in several ways. The conventional approach is to adjust cable delays to digitize all data from the experiment within a coincidence time (e.g. given by a gate). This is, however, also the most inflexible approach in view of the different DAQs that should be coupled together. Another option is to perform full data readout with subsequent selection of suitable events. This requires an efficient way of addressing data into the past, corresponding to a certain delay time. The detector system at the two locations PF4 and MF2 should provide both, absolute times for a time-of-flight measurement and position information in horizontal direction. This can be realized using a circular ring buffer to store timestamps and positions for the detector systems. Typically one would expect some 10..20 Bytes/event of information here. Given a sampling frequency of about 100 MHz, this corresponds to a data rate of 1-2 GByte/s for the buffer input. A similar system has been already realized for the mass measurements at the ESR, using commercially available oscilloscopes for sampling. We want to develop a dedicated readout board using contemporary FPGA designs. The design will be an extension of the existing GSI Taquila system (see NUSTAR-DAQ section). The board should be synchronized by the common time distribution system (see NUSTAR-DAQ section). It should store all channels synchronously with the time-stamp given by the sampling clock into its circular ring buffer. The relative time within the samples is then given for every hit by the ADC value form the TAC. In this way, a precision for the timing information of 50-100 ps can be reached. The digital delay can then be realized by reading out the circular buffer with a certain offset of the readout pointer as the data is stored in fixed time intervals. The reduced data rate is then expected to be a few MByte/sec only. Apart form this option we will look for other developments for the different FAIR experiments.

In order to avoid long storage times, we foresee to place this readout system in the Super-FRS DAQ electronics-room, which should be nearby the R^3B and LEB counting rooms. In that case signal propagation and beam propagation downstream would be aligned and the trigger information could be provided directly to the readout modules, thus saving additional delay times.

Standard electronics

The remaining particle identification and tracking can be realized using a conventional trigger scheme. The existing VME readout scheme will be gradually updated with the upcoming novel developments described in the NUSTAR DAQ section. In order to come up with a fast readout scheme we will investigate to reduce the data already before building events to be written to mass storage for all detector systems (e.g. tracking detectors could already deliver pre-processed positions instead of raw times). We expect about 100 words of data at a rate up to 1-10 MHz corresponding to 100 MByte/sec up to 1 GByte/sec. These are maximum values; typically the rates to be handled in the different experiments are in the order of a few 10 kHz.

2.6.6 Cost estimates for detectors and data acquisition

Detector & DAQ cost estimate	Quantity		
SEETRAM counters	2		
Beam Induced Fluorescence	1		
Multi Wire Gas Detectors	32		
Current Grids	32		
Pick Ups	2		
MUSIC detectors	4		
Resonant Transformer	1		
Cryogenic Current Comparator	1		
CVD-DD (diamond detectors, calibration)	1		
CVD-DD (diamond detectors, calibration)	1		
DAQ system			
Sum without options			
options (see text)			
(i) CVD-DD (diamond detectors, focal planes)	4		
CVD-DD readout	4		
(prices are expected to drop, see text)			
(ii) conventional scintillator array (5mm pitch, MF2)	1		
ladder with scintillators (var. thickness) 2 fast PMT, elec.	3		
Total costs (i)			
Total costs (ii)			

2.7 General layout, infrastructure and engineering

2.7.1 General layout

The high-intensity primary beams that will be delivered by SIS100/300 in the final stage of FAIR require a special layout of the first section of the Super-FRS that contains the production target(s) and the beam dumps. Following concepts developed at other radioactive-beam facilities (e.g. PSI, TRIUMF-ISAC, RIKEN-RIBF, GANIL-SPIRAL), we will apply the "plug" concept in the Pre-Separator up to PF1. This concept involves:

- a combination of beam-line inserts (targets, beam-dumps, slits, diagnostic detectors etc.) with local mobile shielding that can be removed as one unit ("plug");
- a *compact* shielding of the beam lines and vacuum chambers;
- vertical insertion of the plugs along rails into the vacuum chambers;
- vacuum seals and media connection in a moderate-radiation area above the local shielding that can be serviced manually after shutdown.

Schematically, this concept is depicted for the production-target area in Figure 16. The compact shielding reduces the shielding volume (and thus cost) and avoids air activation. Plugs can be removed individually from their common vacuum chamber; the vacuum chamber itself can be separated from the beam line by inflatable "pillow" seals. A similar scheme will be applied to the beam-dump modules in between the first dipole magnet sections and at the Pre-Separator degrader unit.

Areas at and downstream from the Pre-Separator mid-plane (PF2) are expected to be less activated by at least 2-3 orders of magnitude and to be exposed to dose rates similar to the present FRS. Consequently, the same concepts developed and applied successfully for FRS will be foreseen there.

2.7.2 Maintenance and handling of highly-radioactive components

The service platform mentioned above, where all radiation-sensitive devices are located (pumps, polymer vacuum seals, media connectors) allows manual intervention during shut-down periods. After media and vacuum disconnection, plugs will be removed vertically by a heavy-load crane and will be inserted in shielded transport containers in which they can be safely transported to either a storage position (in case a new module is to be inserted) or a hot cell (in case repairs have to be performed on a module). The transport container ensures that highly-activated components are never exposed to the surrounding areas and that manual intervention is possible e.g. in case of crane malfunction.

2.7.3 Maintenance and handling in low-radiation areas

Contrary to the high-radiation areas, the less activated areas in the Super-FRS main separator will have a *wide* shielding with a service area that allows operation of an industrial robot equipped with appropriate tools to disconnect devices from the vacuum containers and the media and to remove them from their respective flanges. A well-shielded storage area has to prevent radiation damage to the robot during beam-on periods. All other concepts can be easily adapted from current FRS robot operation techniques.

2.7.4 Vacuum system

The vacuum system, pumps, valves and controls, will be based on the experience gained at the present FRS. The requirements for the vacuum system of the Super-FRS are mainly determined by the necessity to be coupled to the UHV systems of the storage rings and to the driver accelerator without applying any separation foil. At the relatively low primary beam intensity at the present FRS a thin titanium window is used between the separator and the vacuum of the beam line to the SIS-18. At the Super-FRS such a window would not survive interaction of the high-intensity fast extracted beam. A foil between the achromatic final focal plane and the collector ring would severely disturb the experimental conditions, especially for the heaviest fragments which are not fully ionized at a kinetic energy corresponding to 13Tm. In summary, we aim at pressures of better than 10^{-7}mbar and will use UHV- compatible materials inside the vacuum chambers. The residual gas pressure will be of course slightly higher in the Pre-Separator with the pillow seals, the hot materials due the energy deposition of the primary beam and the plug system compared to other sections of the Super-FRS.

For illustration, two typical vacuum chambers with the corresponding valves, pumps and focal-plane equipment are shown in Figure 57 and Figure 58.

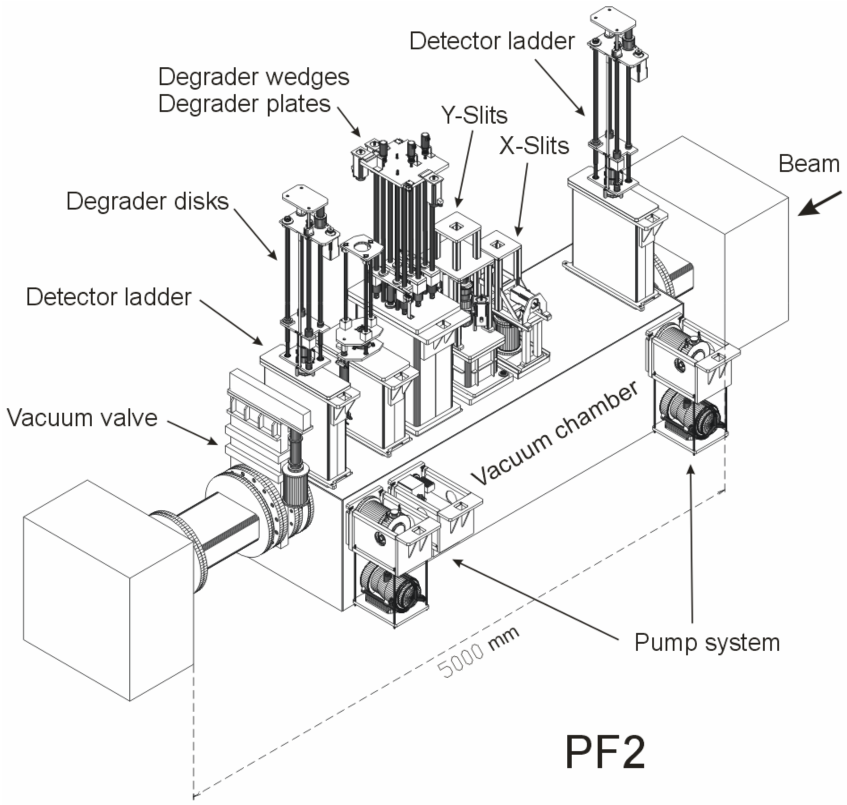

Figure 57 Setup at the mid focal plane of the Pre-Separator (PF2). The degrader system at the focal plane PF2 consisting of rotating disks, a homogenous degrader with continuously variable thickness (wedges), and plates is plotted with its vacuum chamber, valves and pumping system. In front of the degrader system a pair of slits in x- and y-direction is mounted. Two universal detector systems have been placed at a suitable distance in the vacuum chamber to measure the position and angles of the ions at the different intensities. All movable components can be operated remotely.

Since PF2 can have a significant radiation field any maintenance will be done with a robot system. First experience with such robots is presently gained at the FRS, where one device has been installed at the first focal plane. A photo of the robot at the first focal plane of the FRS is shown in Figure 60.

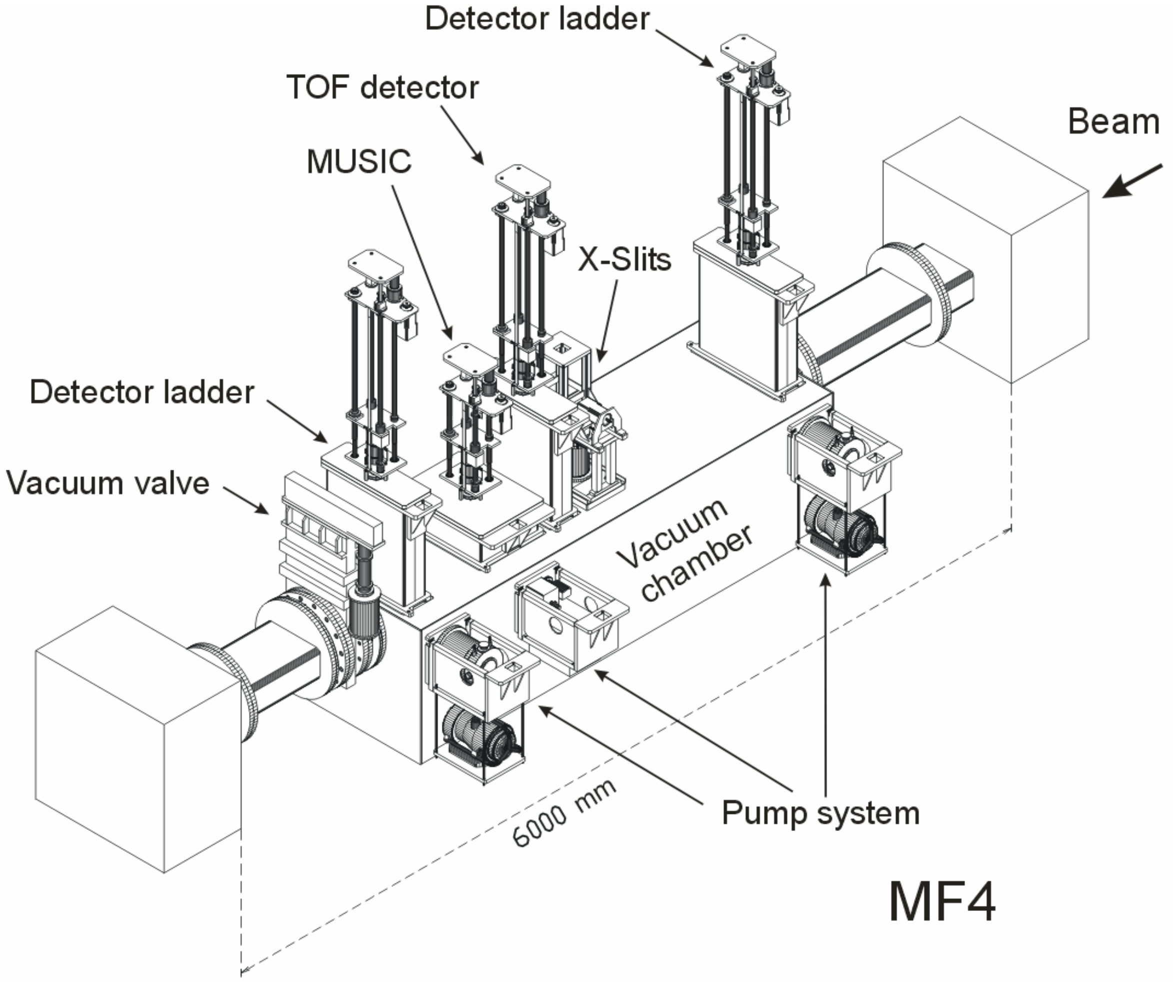

Figure 58 Setup at the final focal plane of the Main-Separator (MF4). The vacuum system is quite similar to all other focal planes, here at MF4, mainly detectors for in-flight particle identification are installed.

An overview of the total vacuum system of the Super-FRS is schematically shown in Figure 59.

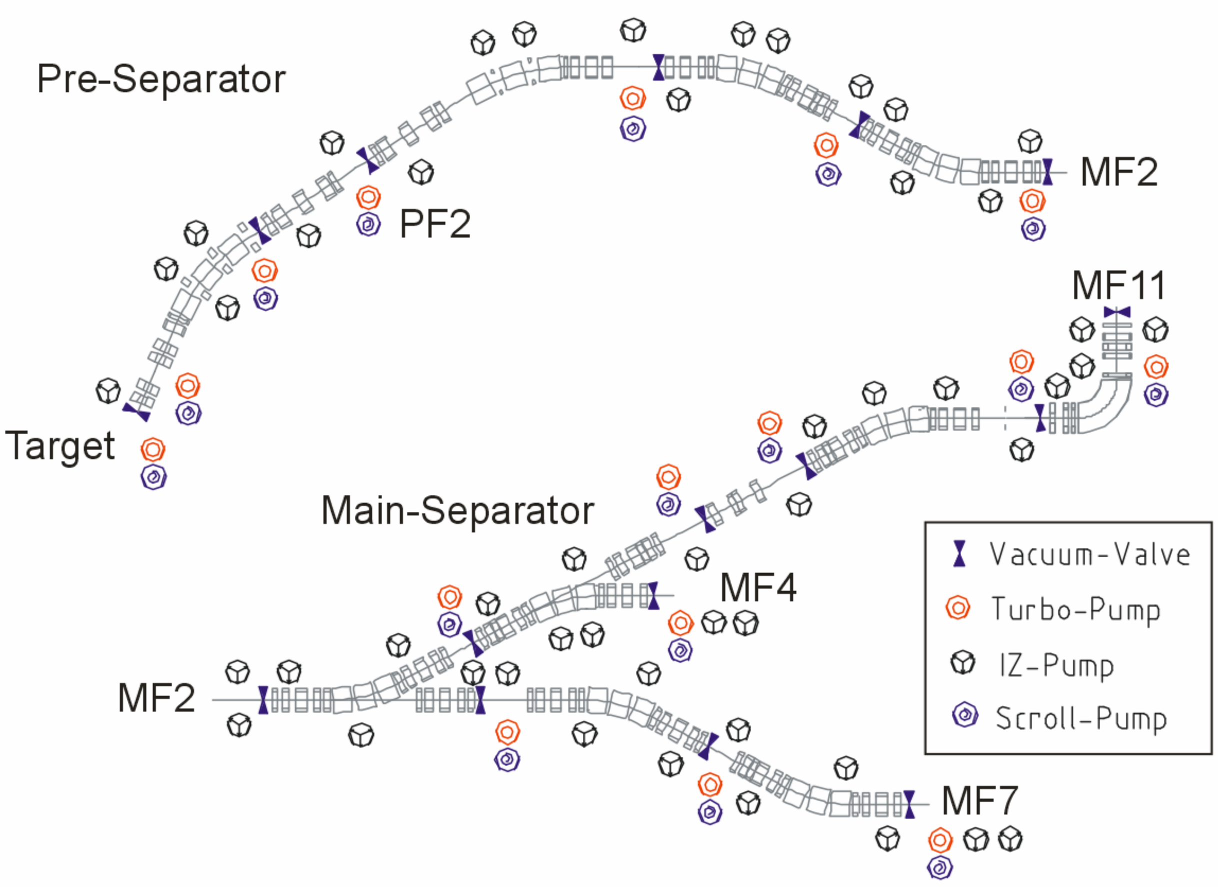

Figure 59: Schematic overview of the Super-FRS vacuum system including oil-free pumps and valves.

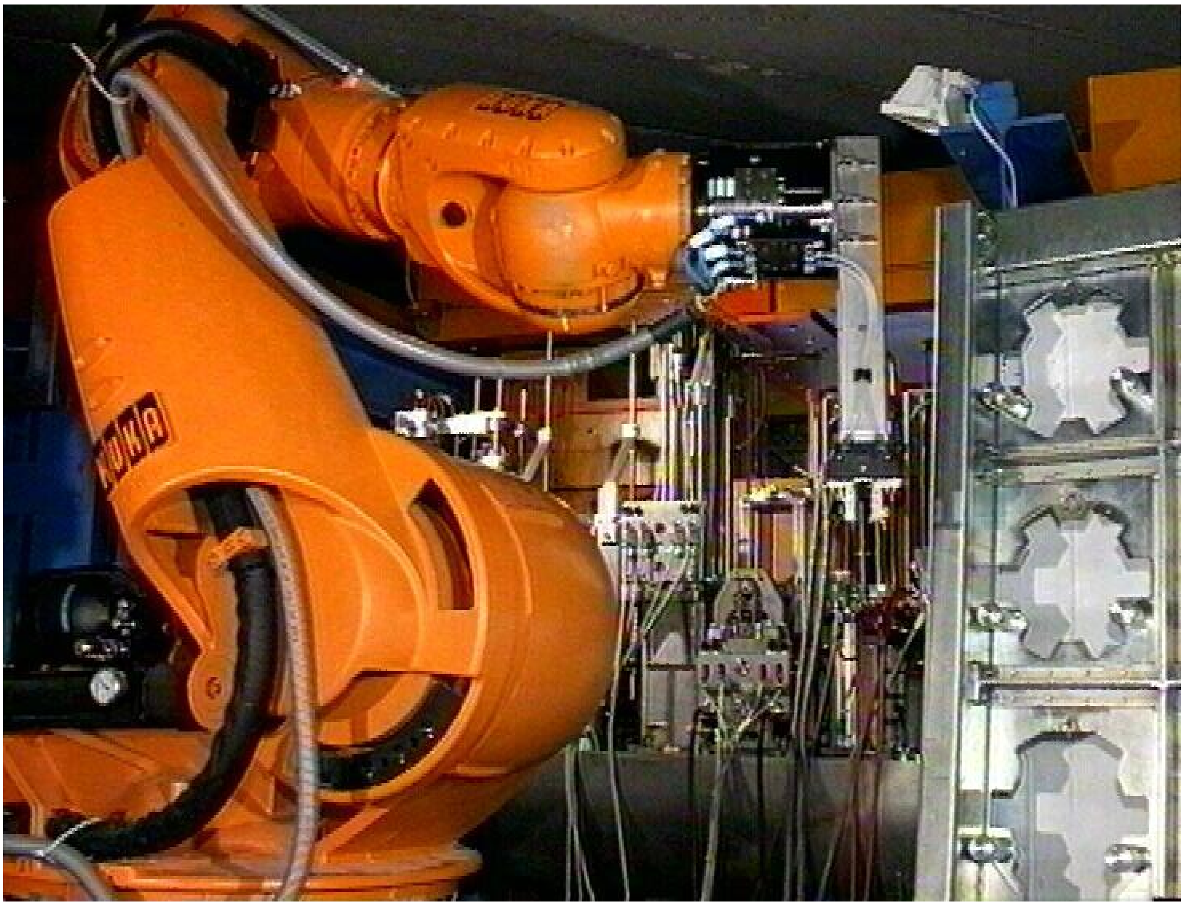

Figure 60: Robot for remote maintenance installed at the first focal plane of the present FRS.

2.7.5 Interlock system

The general procedure for high-intensity operation is to adjust the beam on detectors at lower intensity. The magnet setting is saved as a reference. The effective thickness of the target and other material in the beam line is also defined. For high intensity operation some diagnostic detectors must be removed but the conditions of SIS100/300, targets, magnets, and the first degrader must stay the same.

The interlock system must prevent damage and consequent delay for repairing. Already nowadays at the FRS it would be possible to destroy certain elements with the beam. The interlock and general safety system can guaranty that no damage to humans can happen. Much experience has been gained with the set up successfully applied at the present therapy system at GSI. As the Pre-Separator is the most critical part only specially trained people should be allowed to set up the device for high-intensity beams.

Different levels of interlocks can be defined:

- **Int-0**: **Type of operation is not allowed**. The control system must refuse input. It will have also input from physics. For example the energy loss code and the target/degrader thickness are known to the program. Like this it is possible to predict the position of beam dump. The program can then refuse changes in energy or degrader thickness which would cause that the beam is dumped at wrong positions.

- **Int-1**: **Stop extraction and dump of beam in SIS12 or SIS100/300** and no further beam request. It will be possible to stop extraction in the slow extraction mode within a few ms. This will avoid the rest of the spill to be extracted. Afterwards the beam must be dumped in the synchrotron beam dumps. In fast extraction mode this simply means no extraction towards the Super-FRS.
- **Int-2**: **No beam request**. Many devices in the Super-FRS must be checked before an extraction of a spill can be requested. Otherwise the machine will not start accelerating ions.
- **Int-3**: **General radiation safety interlock.** This stops the beam in case of detection of too high radiation levels on the outside of the area with controlled access or no access during beam time.
- **Int-4**: **User defined interlock**: This is intended to protect detectors in the Super-FRS and following experiments. It can be defined by experimentalists and stop request or reduce intensity.

Situations for Int-0:

1.) Too high energy in synchrotron for maximal beam intensity leads to too much energy in one spill (e.g. $N=10^{12}$/s uranium and E>1500 MeV/u).
2.) Too low energy so that ions could heat target or entrance of beam dump too much, especially in fast extraction mode or have a magnetic rigidity outside of the range covered by the beam dumps.

Situations for Int-1:

1.) Too high intensity at target for given situation. Detect with beam transformator or cryogenic current comparator in front of target.
2.) Too high intensity after degrader at PF2 which could damage degrader and slits. Detect with transformator and based on calculation.
3.) Target wheel not in proper position can lead to wrong energy after the target and indicates possible damage to the target. Online monitoring of wheel required.
4.) No fast extraction target present. Must be checked by optical means before extraction.
5.) Deviation in position on target, tested by inductive position probes in fast extraction, and beam induced fluorescence in rest gas or hot spot on target wheel in slow extraction mode (Δx, Δy <2mm)
6.) Too high temperature in target or beam dump. Detect with resistive temperature measurement, infrared optical control for target.
7.) Quenching of superconducting magnets.

Situations for Int-2:

1.) Diagnostics detectors or similar inserted in the Pre-Separator, valves closed, or no PF2-degrader inserted. Detect by readout of feed throughs and step motors.
2.) Magnets not at set field strengths and currents. Requires field and current measurement.
3.) Not enough flow of cooling water in cooled devices and magnets.
4.) Too high temperature of magnets, especially in the cryo system.
5.) Bad vacuum, pressure gauges show to high pressure level.

What is not protected by these interlocks?

Slow extraction: As the SIS beam can be shut off within 10ms, the heat load on the target beam dump and other devices can hardly excess critical values if detected fast.

Fast extraction: One spill of beam can still be delivered if the failure happens in between checking and extraction. This can cause severe damage to the devices. However, most components cannot fail within 10ms. For example the magnet field decreases slowly and mechanical movements are also slower.

Maximal damage

If these control systems fail in the worst case overheating and high pressure may lead to fracturing of devices. As some of them especially the beam dump are water cooled this can lead to water leaking into the vacuum system. A sink underneath the beam dumps must catch this water as it will be activated.

By melting of the beam pipe a vacuum leak may be caused. Fast shutters to protect other parts of the facility in this case are necessary.

Special monitoring devices

- Camera watching target wheel, looking at the opposite side of beam spot and via mirrors for radiation protection.
- Laser beam reflected on Li jet target with mirror system to have laser source and detector outside target area.
- Fast read out of position and intensity from detectors.
- Temperature sensors in critically heated parts (target, shielding block after target, beam dumps).
- Flow meter for water cooling.
- Online calculation of beam position from magnet setting, known beam and devices inserted.

2.7.6 Cost estimates for the vacuum system, drives and feedthroughs, and infrastructure

Vacuum-system cost estimate	Quantity		
Dipole chamber (Pre-Separator I)	3		
Dipole chamber (Pre- & Main Separator II)	24		
Dipole chamberr (Energy Buncher)	4		
Beam pipe (163 m)	163		
Diagnostic chamber (different sizes)	21		
Bellow (L=150, D=400)	73		
Pillow seals	4		
Support (different sizes)	24		
Pumps (TPU 400 & 1000)	22		
Pumps (IG)	48		
Pumps (Scroll pumps, different sizes)	22		
UHV valves (D=400)	15		
Infrastructure (Controler, seals, cable; different locations)	25		
Total costs			

Drive&feedthroughs cost estimate	Quantity		
Target ladder	1		
Slit systems (x and/or y)	18		
Detecor feed-through	38		
Infrastructure & control	94		
Total costs			

Super-FRS infrastructure cost estimate

Infrastructure cost estimate	Quantity		
Robot system	2		
Slewing crane	15		
Control console			
Gas supply	15		
Media supply	15		
Total costs			

3. Safety

3.1 General safety considerations

The general dangerous materials to be used at the Super-FRS are those that are already in use today at the FRS.

Inflamable gases for detectors: Methane in ionization chambers. For the small amounts used the exhaust can most probably be diluted and the usual outlet be used.

Liquid nitrogen: Used in large amounts for cooling of magnets. Today an automatic nitrogen filling system is already installed at the FRS for germanium detectors. The concentration of nitrogen is monitored and an alarm caused in case of danger of suffocation.

Vacuum windows: Metal foils (~100µm titanium) over a larger area of 40cm x 20cm will be used to seal the vacuum from experimental setups in air. Breaking of the windows can be avoided by safety caps while working in these areas. Fast shutters must be installed upstream in the beam line to stop the resulting shock wave from propagating to other beam lines.

High voltage: Usual high voltage ($U_{max} < 10$ kV) will be used.

3.2 Radiation environment (radiation protection)

3.2.3 General radiation protection measures

In areas open for access to technical or scientific personnel or to the general public, radiation dose limits given by the Radiation Protection Ordinance, must not be exceeded. Assuming a worst case scenario the additional annual dose for the population, arising from the operation of all facilities at the GSI site, must be less than 1 mSv, in addition the effective dose resulting from the release of radioactivity to the environment has to be smaller than 0.3 mSv per year. According to the limits of the German Radiation Protection Ordinance the dose rate should be less than 0.5 µSv/h on GSI ground and less than $\approx 8 \cdot 10^{-8}$ Sv/h outside the facility.

3.2.4 Activation of air

Activation of air can lead to exposition of personnel if areas with previous beam operation have to be entered. This exposition can be substantially reduced by applying a ventilation system in areas under consideration. However the outlet air of these areas may again lead to exposition of population and personnel. Hadronic or heavy ion beams in the energy range of 1 GeV/u produce a variety of radioactive isotopes while passing through air. Short-lived positron emitters like ^{11}C, ^{13}N, ^{14}O and ^{15}O are being produced due to spallation reactions. ^{7}Be and ^{32}P which have lifetimes in the order of weeks, play an important role in activation of air.

Longer lived beta-emitters like ^{3}H and ^{14}C are expected to be produced as well in substantial quantities. Finally, ^{41}Ar can be produced by capturing thermal or slow neutrons by the noble gas Argon. It is important to reduce the path length of the neutrons in the air to reduce the activation process in air. A fully encapsulated target area is planned to effectively reduce the activation of air, (see Figure 61).

3.2.5 Activation of soil

Roughly 70 neutrons with energies larger than 100 MeV are being produced when a uranium particle with the energy of 1 GeV/u is completely stopped in a thick iron target. These neutrons may also lead to activation of soil when there is no sufficient shielding below the target area. ^{22}Na, ^{54}Mn, and depending on the composition of the soil ^{60}Co and other trace elements are of largest relevance in terms of polluting the ground water.

3.2.6 Shielding against direct radiation

A simple model has been developed for the first shielding design of the Super-FRS. Based on the measurements of double differential neutron yields originated from a 1 GeV/u uranium beam hitting a thick iron target, dose values can be estimated via the following formula.

$$H(r,\vartheta) = H_0(\vartheta) \cdot I \cdot \frac{1}{r^2} \cdot e^{-\frac{d \cdot \rho}{\lambda(\vartheta)}}$$

The dose(rate) $H(r,\vartheta)$ is derived from the angular dependent constants $H_0(\vartheta)$ and $\lambda(\vartheta)$, the density ρ of the shielding material with the thickness d and the ion rate I. The constants $H_0(\vartheta)$ and $\lambda(\vartheta)$ have been determined by Agosteo et al. [63] by fitting the results of a Monte-Carlo calculation using the measured neutron spectra mentioned above [64].

Three representative modes of the Super-FRS were investigated to cover the large variety of settings in the experimental operating:

- separation of a fragment with similar magnetic rigidity compared to the primary beam. ^{132}Sn by projectile fission of ^{238}U
- separation of a very neutron rich fragment ^{11}Li by fragmentation of ^{18}O.
- separation a very neutron deficient fragment ^{100}Sn by fragmentation of ^{124}Xe

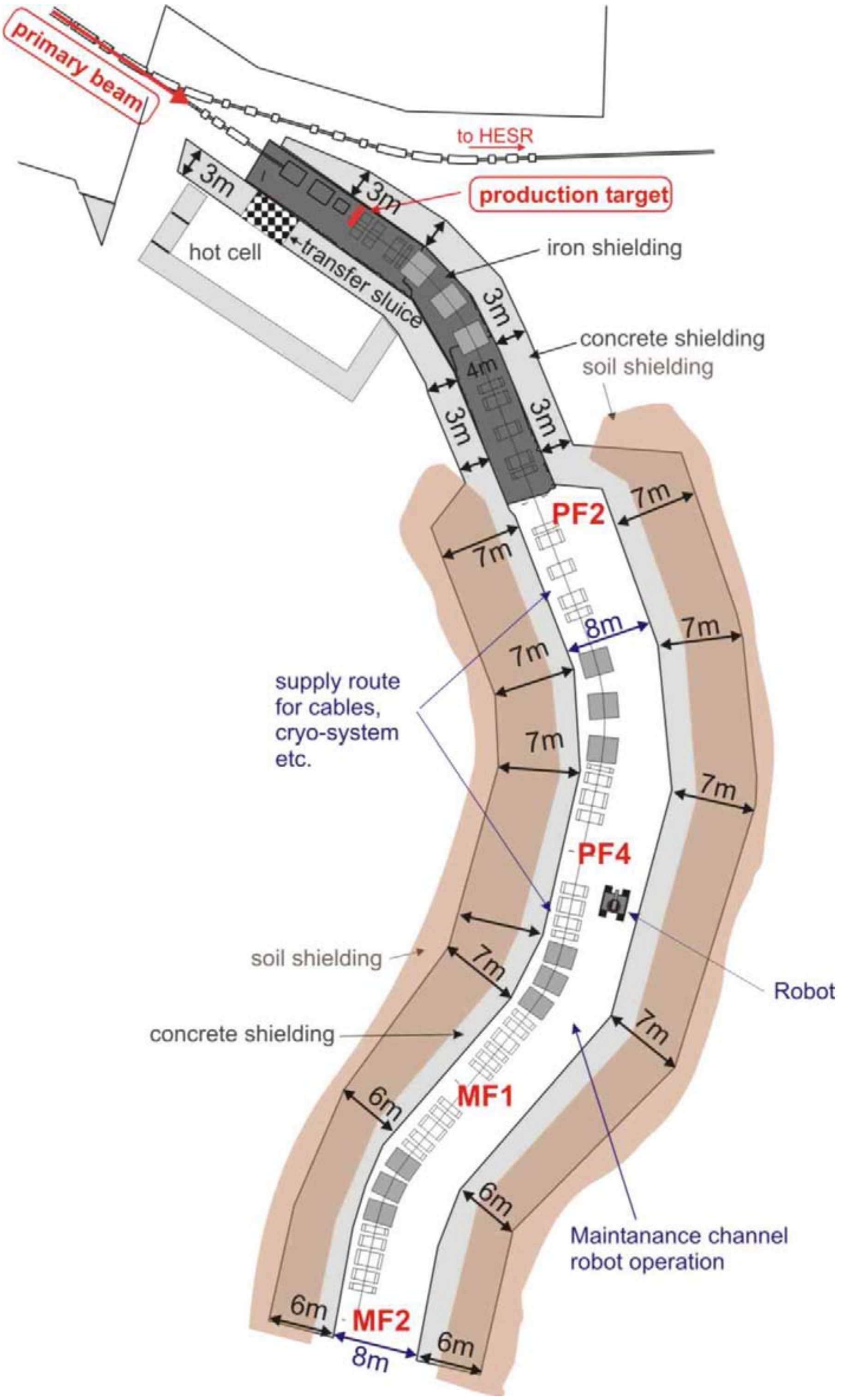

Figure 61. Schematic layout of the Super-FRS with beam line and shielding measures. The area from the target up to the intermediate focal plane PF2 of the Pre-Separator is shielded with iron in order to provide a compact radiation protection. Without iron roughly 8 m of concrete are necessary to assure the same shielding effect. The concrete can be partially replaced by soil taking into account a ~20% smaller absorption of the soil.

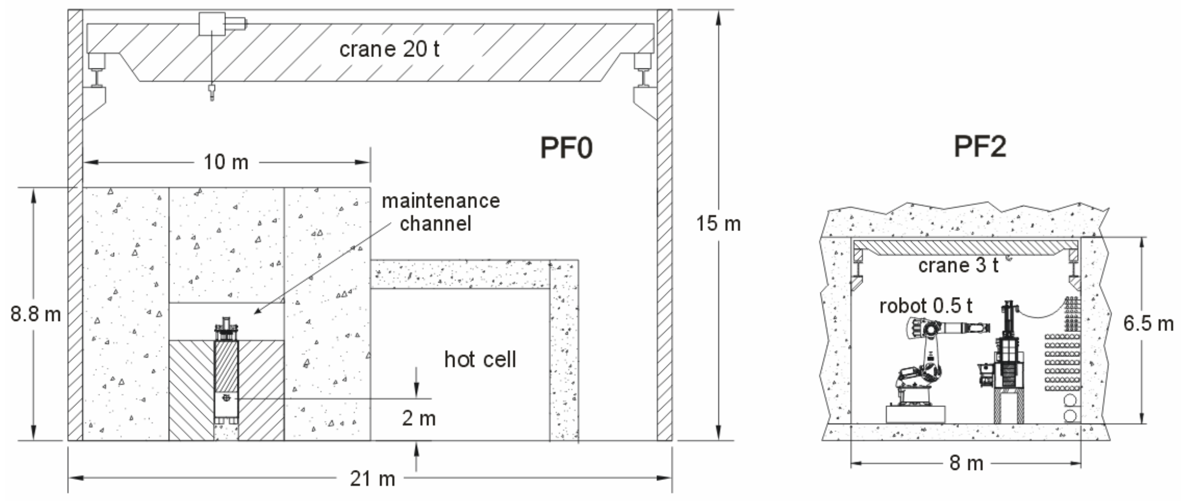

Figure 62. Left hand panel: Layout of the Super-FRS target area with plug system, hot cell, shielding and the overhead travelling crane. Left hand panel: Layout of PF2 focal plane with the first degrader system, robot for maintenance and a small overhead crane.

The distributions of the losses of both the primary and the fragment beams have been calculated [65] with the fragmentation model of ABRABLA [66] and the simulation code for fragment separators Lieschen [67]. Figure 61 shows the calculated thicknesses of the concrete walls along the Super-FRS. The thicknesses reach from ≈ 7.0 m downstream of the target PF2 down to 6 m at the middle focal plane MF2 of the main separator. In the close vicinity of the target a compact iron shielding will be used to replace the concrete. Further on concrete will be partially replaced by soil taking into account the somewhat larger absorption length. A hot cell is foreseen to store activated components. In order to benefit from the close distance to the target area a transfer sluice could be established for an easy and safe storage mechanism.

3.3 Activation of beam line parts

Many parts of the Super-FRS can be activated, especially in the Pre-Separator up to PF1. A simulation of the activation of iron on top of the target was done with the PHITS program [31]. The scenario of 100 days beam time with a 1.5 GeV/u 10^{12} ^{238}U beam was investigated and the activation in a 63cm x 63cm and 10cm thick iron block calculated. Taking into account the self shielding of the thick iron block, the different longer-lived nuclides produced (mainly ^{56}Co, ^{52,54}Mn, ^{48}V), and applying the dose conversion factors of ref.[43] this leads to a dose rate of 1 µSv/h in 1m distance after one day of waiting.

As the flux of low energy neutrons is rather homogenous in this area, cf. Figure 52, we may extrapolate this value for the whole activated and unshielded surface in the maintenance channel.

This includes also concrete which is less activated than the iron parts (mainly ^{22}Na). Doing this we obtain a dose rate of about 10 μSv/h for a person working in the maintenance channel. After 30 days this value will be reduced to 4 μSv/h.
As a conclusion the maintenance channel on top of the beam line from target to PF1 is accessible after one day of waiting. This is a reasonable time scale as anyway the concrete shielding on top has to be removed first.

The highly activated parts like beam dump and target including the shielding plug can then be pulled into a shielding bottle like the one shown in Figure 63 used at a corresponding position at PSI. While the concrete shielding is removed the hall has to be an area of controlled access for radiation protection. But as the radiation level is rather low it is also clear that with the help of the shielding bottle the radiation level outside the hall cannot exceed the limit of 0.08 μSv/h explained above. Inside the hot cell manipulators will be used to exchange parts, for example to mount a new target wheel.

Figure 63: Radiation shielding bottle at PSI [8] to move activated parts to a hot cell. The whole plug is pulled into the bottle which is then transported with a crane.

A typical value to still allow hands-on maintenance is 1 W/m for the beam power deposited by a 1 GeV proton beam along the beam line [68]. This value can be scaled to a heavy ion beam considering the shorter range and nuclear fragmentation [69]. As already described in section 2.4 the the beam dump will be the most activated part as it catches almost the full beam power of maximal

58kW. At 1 GeV/u the factor for comparing protons with uranium ions is still 0.2, which means an equivalent of 10 kW/m proton beam at the beam dump, which forbids maintenance by people but robots can be used.

A similar conclusion can be drawn from the neutron fluences into the surrounding vacuum chamber shown in Figure 29. They are a factor 100-1000 less than in the beam dump but this still means strong activation of the surrounding vacuum chamber leading to dose rates of (0.3-3)mSv/h at the outside of the chamber. As the magnets are protected from the beam they will be activated about a factor 10 less. If a magnet in the area PF0 to PF1 would have to be replaced a long waiting time and a special shielding of the hall with the crane has to be installed.

The values are much reduced in the Main-Separator. A factor 1000 times lower beam intensity and more distributed beam dump lead to about 1 W/m. Still, allowing 10^9 Uranium ions at 1GeV/u to pass through the whole Main-Separator is equivalent to the uranium primary beam rate nowadays at the FRS ($2x10^9$/spill as in 2004) even about a factor 5 higher due to the higher repetition rate.

The FRS target area cannot be accessed directly during experiments and stays as an area with controlled access most of the time.

4 R&D phase (2005-2006/2007)

4.1 Description and ranking of necessary developments (objectives, milestones)

to assign the risk in the critical parts (target, beam dump, magnets)

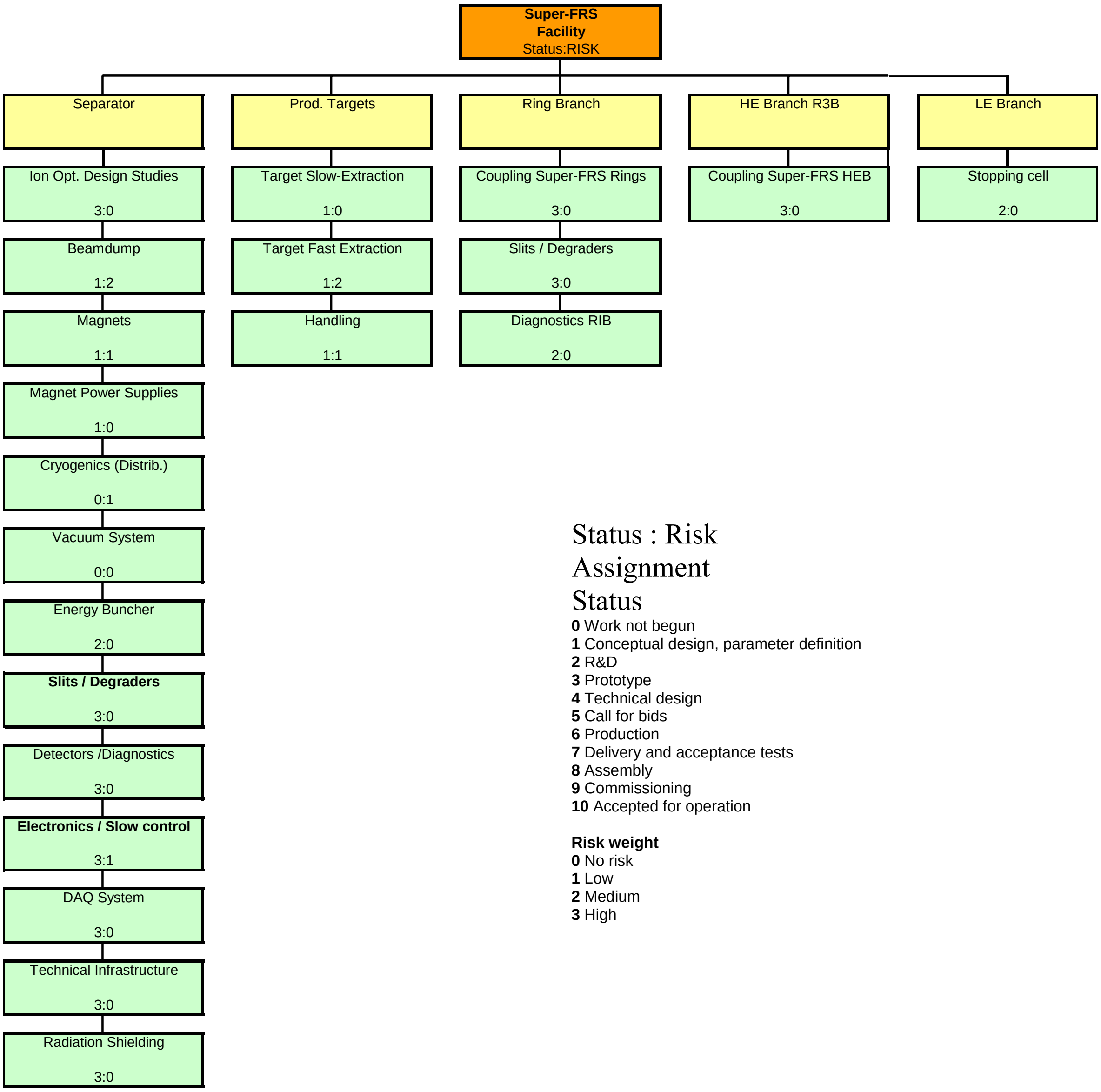

Status : Risk
Assignment
Status

0 Work not begun
1 Conceptual design, parameter definition
2 R&D
3 Prototype
4 Technical design
5 Call for bids
6 Production
7 Delivery and acceptance tests
8 Assembly
9 Commissioning
10 Accepted for operation

Risk weight
0 No risk
1 Low
2 Medium
3 High

4.2 Gantt diagram for R&D with milestones

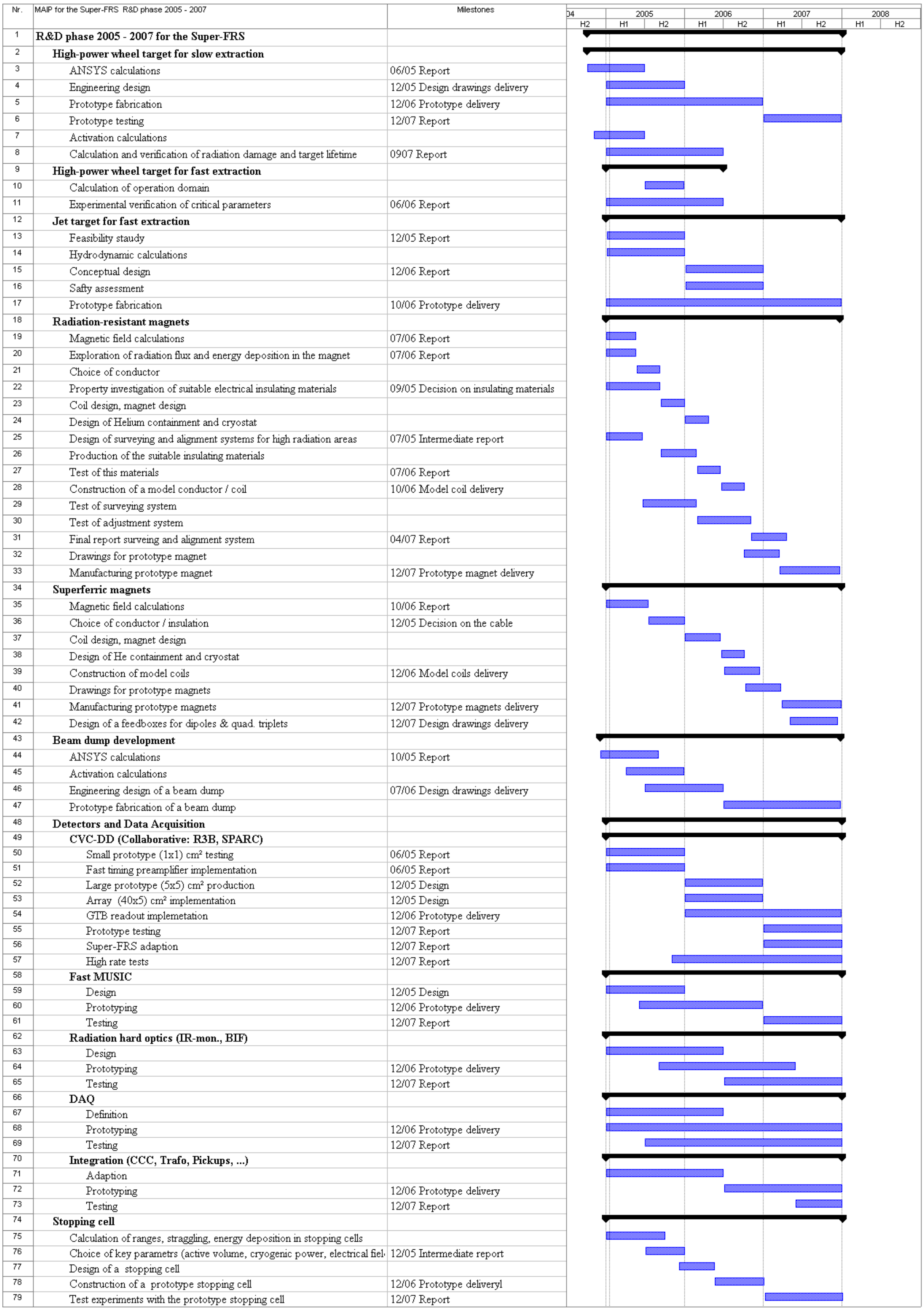

Nr.	MAIP for the Super-FRS R&D phase 2005 - 2007	Milestones
1	**R&D phase 2005 - 2007 for the Super-FRS**	
2	**High-power wheel target for slow extraction**	
3	ANSYS calculations	06/05 Report
4	Engineering design	12/05 Design drawings delivery
5	Prototype fabrication	12/06 Prototype delivery
6	Prototype testing	12/07 Report
7	Activation calculations	
8	Calculation and verification of radiation damage and target lifetime	0907 Report
9	**High-power wheel target for fast extraction**	
10	Calculation of operation domain	
11	Experimental verification of critical parameters	06/06 Report
12	**Jet target for fast extraction**	
13	Feasibility staudy	12/05 Report
14	Hydrodynamic calculations	
15	Conceptual design	12/06 Report
16	Safty assessment	
17	Prototype fabrication	10/06 Prototype delivery
18	**Radiation-resistant magnets**	
19	Magnetic field calculations	07/06 Report
20	Exploration of radiation flux and energy deposition in the magnet	07/06 Report
21	Choice of conductor	
22	Property investigation of suitable electrical insulating materials	09/05 Decision on insulating materials
23	Coil design, magnet design	
24	Design of Helium containment and cryostat	
25	Design of surveying and alignment systems for high radiation areas	07/05 Intermediate report
26	Production of the suitable insulating materials	
27	Test of this materials	07/06 Report
28	Construction of a model conductor / coil	10/06 Model coil delivery
29	Test of surveying system	
30	Test of adjustment system	
31	Final report surveing and alignment system	04/07 Report
32	Drawings for prototype magnet	
33	Manufacturing prototype magnet	12/07 Prototype magnet delivery
34	**Superferric magnets**	
35	Magnetic field calculations	10/06 Report
36	Choice of conductor / insulation	12/05 Decision on the cable
37	Coil design, magnet design	
38	Design of He containment and cryostat	
39	Construction of model coils	12/06 Model coils delivery
40	Drawings for prototype magnets	
41	Manufacturing prototype magnets	12/07 Prototype magnets delivery
42	Design of a feedboxes for dipoles & quad. triplets	12/07 Design drawings delivery
43	**Beam dump development**	
44	ANSYS calculations	10/05 Report
45	Activation calculations	
46	Engineering design of a beam dump	07/06 Design drawings delivery
47	Prototype fabrication of a beam dump	
48	**Detectors and Data Acquisition**	
49	**CVC-DD (Collaborative: R3B, SPARC)**	
50	Small prototype (1x1) cm² testing	06/05 Report
51	Fast timing preamplifier implementation	06/05 Report
52	Large prototype (5x5) cm² production	12/05 Design
53	Array (40x5) cm² implementation	12/05 Design
54	GTB readout implemetation	12/06 Prototype delivery
55	Prototype testing	12/07 Report
56	Super-FRS adaption	12/07 Report
57	High rate tests	12/07 Report
58	**Fast MUSIC**	
59	Design	12/05 Design
60	Prototyping	12/06 Prototype delivery
61	Testing	12/07 Report
62	**Radiation hard optics (IR-mon., BIF)**	
63	Design	
64	Prototyping	12/06 Prototype delivery
65	Testing	12/07 Report
66	**DAQ**	
67	Definition	
68	Prototyping	12/06 Prototype delivery
69	Testing	12/07 Report
70	**Integration (CCC, Trafo, Pickups, ...)**	
71	Adaption	
72	Prototyping	12/06 Prototype delivery
73	Testing	12/07 Report
74	**Stopping cell**	
75	Calculation of ranges, straggling, energy deposition in stopping cells	
76	Choice of key parametrs (active volume, cryogenic power, electrical fiel	12/05 Intermediate report
77	Design of a stopping cell	
78	Construction of a prototype stopping cell	12/06 Prototype deliveryl
79	Test experiments with the prototype stopping cell	12/07 Report

5 Commissioning

5.1 Description of the commissioning phase

The commissioning of the Super-FRS will be done in stages. The first stage involves the Pre-Separator including the target area. After the ion-optical properties have been verified, the first degrader station at PF2 will be used for fragment beams created with low-intensity primary beams. In the beginning we will take care to have only low activation throughout the Super-FRS system till reliable conditions have been achieved. After the Pre-Separator has been fully commissioned, the Main-Separator and its branches will be tackled in the same way.

Table 16 Multi-annual implementation plan for the Super-FRS

Nr.	
1	**Super-FRS**
2	Development for the Super-FRS setup at the FRS
3	Ion-optical design studies for the Super-FRS
4	Technical Report
5	FP6 EU Design Studies, R&D, Prototyping
6	Technical Design Report
7	EU Design Study completed
8	Pre-Separator
9	Comissioning of preseparator
10	High-Energy Branch
11	Comissioning of High-Energy Branch
12	Ring Branch
13	Comissioning of Ring Branch
14	Low-Energy Branch and Energy Buncher
15	Comissioning of Low-Energy Branch

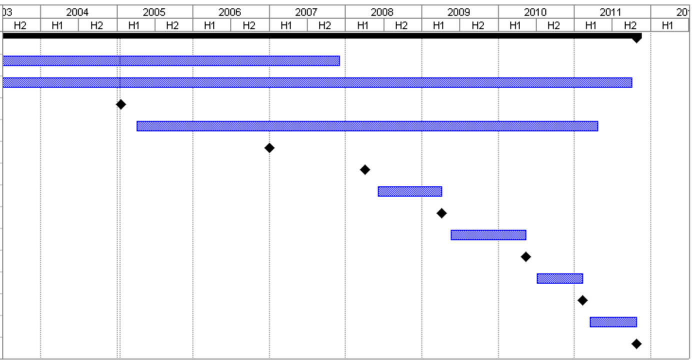

6 Operation

6.1 Description of the operation phase

The Super-FRS can be operated quite analogously to the present FRS. There exists an experienced group of engineers and scientists which is involved in all experiments with different external groups. However, this operation is not realized in a service enterprise but to reach the highest performance the in-house group is actively involved in the research program and experiments.

In the first 14 years of successful operation the FRS experiments amount to 60-70 % of the accelerator running time. Being realistic the total amount of running time at FAIR will also be similar due to the diverse physics program at the different FAIR facilities.

However, there will be one major difference in the operation of the Super-FRS compared to the present separator. The high intensity primary beams at the Pre-Separator will probably demand that only experienced and trained personnel can make the first tuning of the primary beam and also the first setting for fragments at highest intensities.

7 Management organization and responsibilities, Planning of the Super-FRS

Super-FRS Collaboration

All participating institutes working at the different branches of the Super-FRS have indicated that they will actively contribute in the design, construction and commissioning phases of the Super-FRS and its experimental setups. Only in discussions with these users we will find the optimal parameters for the construction and operating. Many technical contributions will come also from the GSI infrastructure and accelerator groups as successfully practiced with the FRS project. The specially listed institutes have indicated to contribute on specific subprojects, see NUSTAR LOIs.

GSI Darmstadt, D-64291 Darmstadt, Germany

Justus-Liebig Universität Gießen, D-35390 Gießen, Germany

Universidade de Santiago de Compostela, E-15706 Santiago de Compostela, Spain

Technische Universität München, D-85748 Garching, Germany

Institute of Analytical Instrumentation, RAS, 198103 St. Petersburg, Russia

Michigan State University, East Lansing, MI 48824, USA

Argonne National Laboratory, Argonne, IL 60439, USA

St. Petersburg State Technical University, 195251 St. Petersburg, Russia

Johannes Gutenberg Universität, D-55099 Mainz, Germany

Technische Universität Dresden, D-01062, Germany

Philipps Universität Marburg, D-35032, Germany

Fachhochschule Mainz, D-55099 Mainz, Germany

Paul Scherrer Institut, CH-5232 Villigen PSI, Schweiz

Babcock Noell Nuclear, D-97080 Würzburg, Germany

Efremov Institute St. Petersburg, Russia.

Budker Institute of Nuclear Physics, RU630090 Novosibirsk, Russia

Technische Universität Darmstadt, D-64289 Darmstadt, Germany

Forschungszentrum Karlsruhe, D-76344 Eggenstein-Leopoldshafen, Germany

Riken, 2-1 Hirosawa, Wako, Saitama 351-0198, Japan

CEA, Saclay, F-91191 Gif-sur Yvette, France

University of Surrey, Guildford, GU2 5XH, UK

Comenius University Bratislava, Sk-84248 Bratislava, Slovakia

7.1 Summary of WPBS work packages

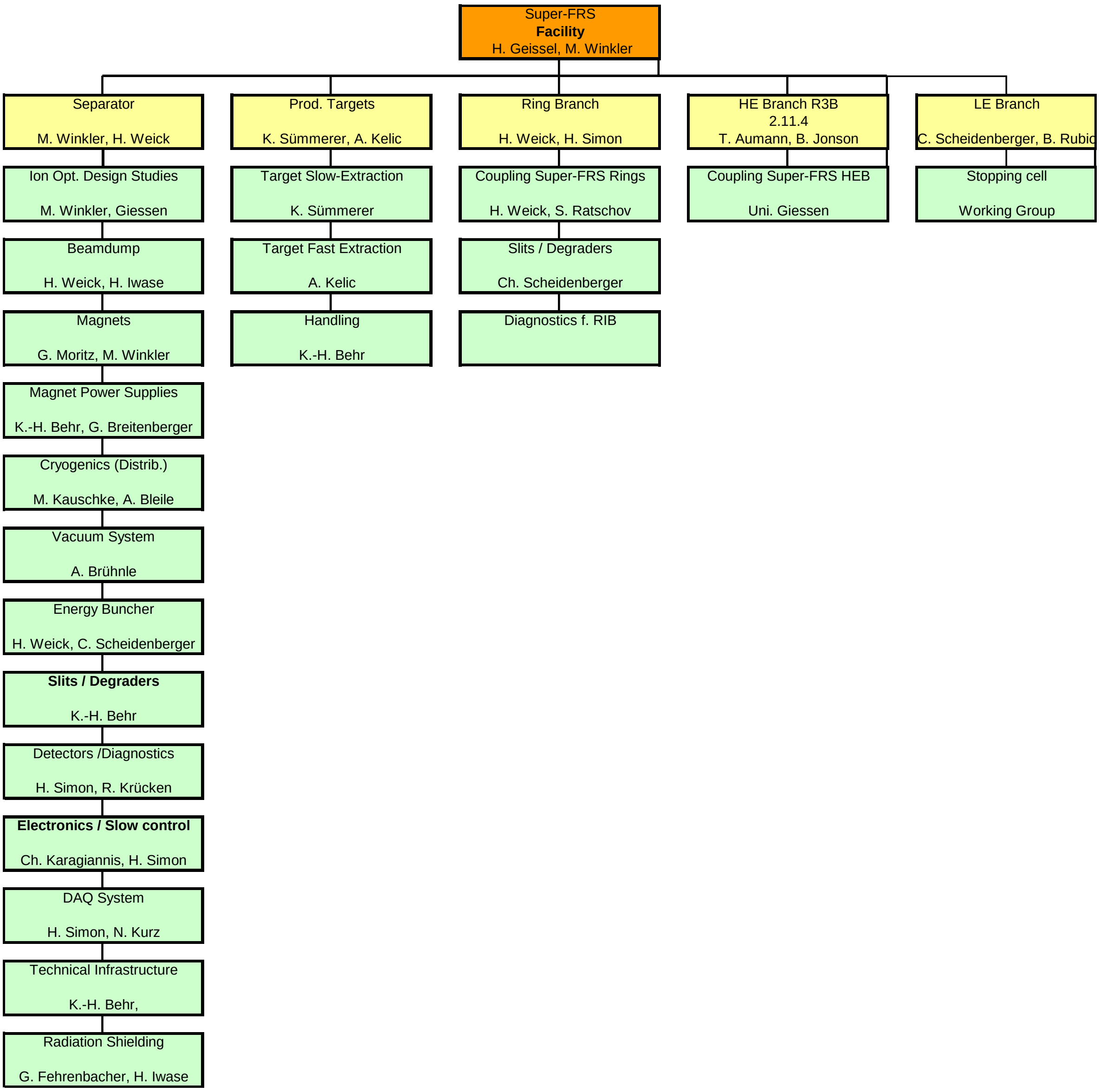

7.2 Total project cost estimate

Global cost estimate for Super-FRS

Super-FRS cost estimate		
Target area		
Magnets		
Power supplies		
Beam dumps		
Degrader system & ion catcher		
Detectors & DAQ		
Vacuum system		
Drives & feed-throughs		

The cost estimate is based on an assumed conversion rate of 0.9 € / $, which is applied mainly to the magnet costs.

7.3 FTE request

In addition to the existing manpower the following personal effort is needed to perform the described projects.

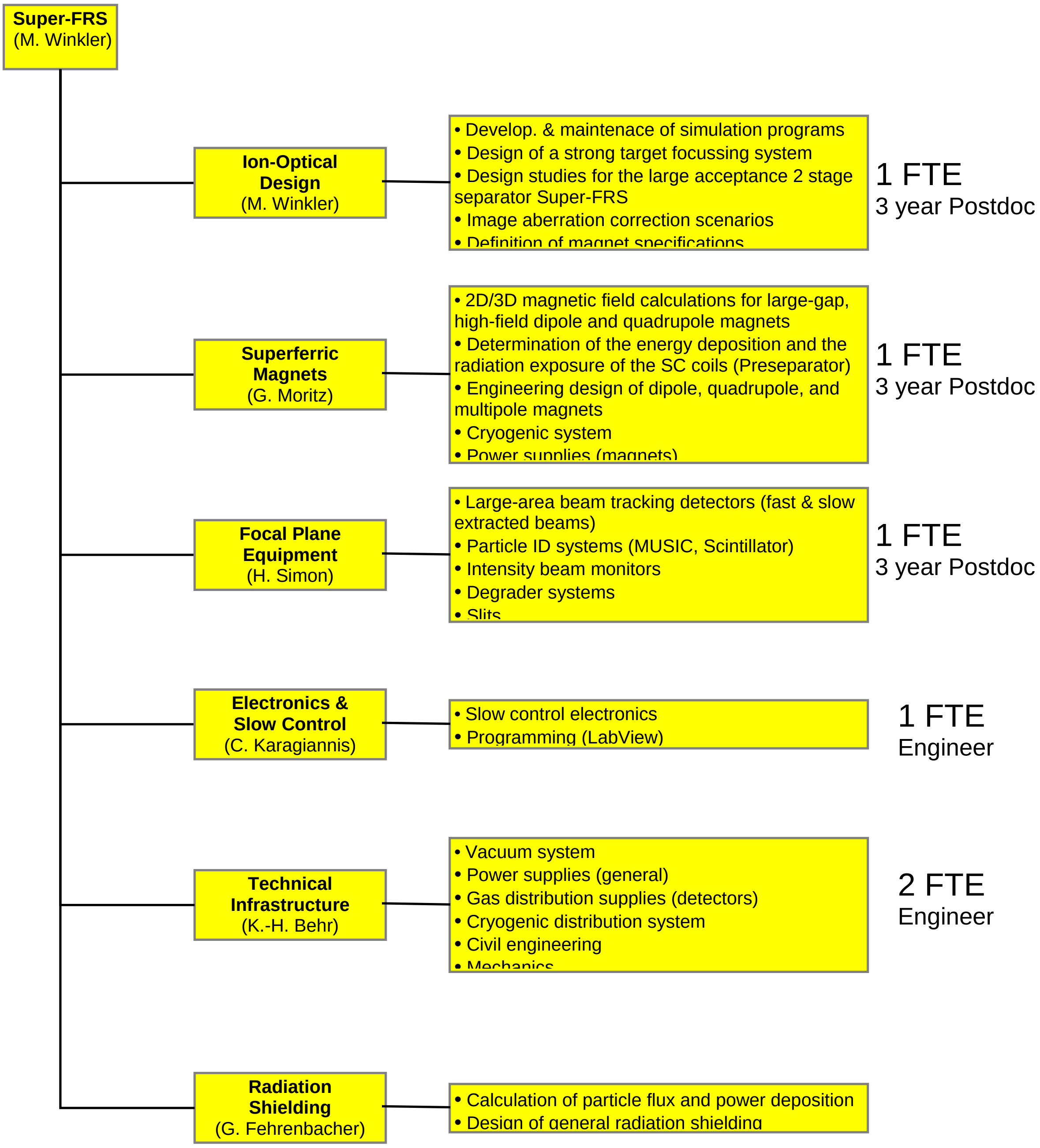

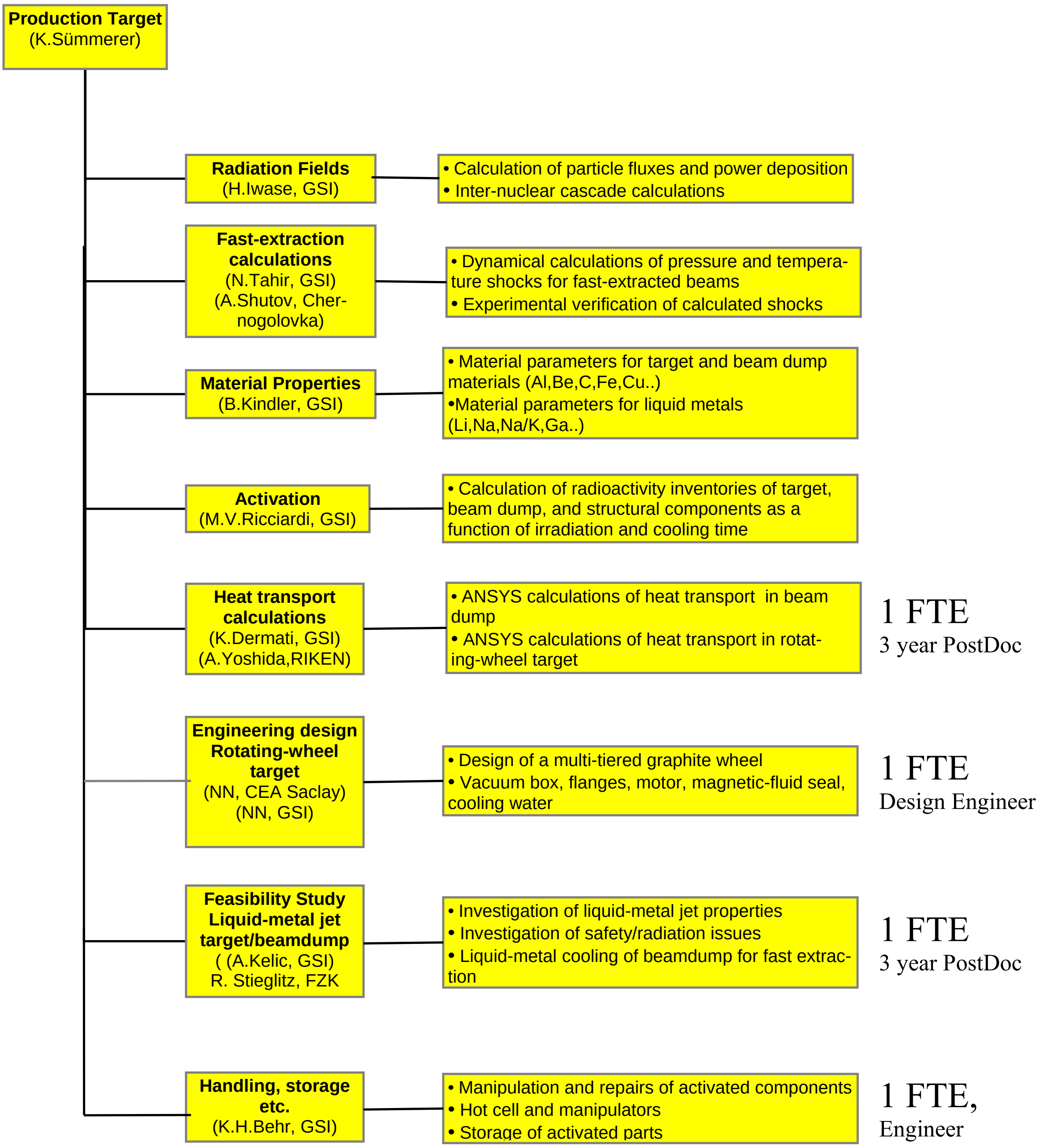

Production Target
(K.Sümmerer)

- **Radiation Fields** (H.Iwase, GSI)
  - Calculation of particle fluxes and power deposition
  - Inter-nuclear cascade calculations
- **Fast-extraction calculations** (N.Tahir, GSI) (A.Shutov, Chernogolovka)
  - Dynamical calculations of pressure and temperature shocks for fast-extracted beams
  - Experimental verification of calculated shocks
- **Material Properties** (B.Kindler, GSI)
  - Material parameters for target and beam dump materials (Al,Be,C,Fe,Cu..)
  - Material parameters for liquid metals (Li,Na,Na/K,Ga..)
- **Activation** (M.V.Ricciardi, GSI)
  - Calculation of radioactivity inventories of target, beam dump, and structural components as a function of irradiation and cooling time
- **Heat transport calculations** (K.Dermati, GSI) (A.Yoshida,RIKEN)
  - ANSYS calculations of heat transport in beam dump
  - ANSYS calculations of heat transport in rotating-wheel target
  - 1 FTE
    3 year PostDoc
- **Engineering design Rotating-wheel target** (NN, CEA Saclay) (NN, GSI)
  - Design of a multi-tiered graphite wheel
  - Vacuum box, flanges, motor, magnetic-fluid seal, cooling water
  - 1 FTE
    Design Engineer
- **Feasibility Study Liquid-metal jet target/beamdump** ((A.Kelic, GSI) R. Stieglitz, FZK
  - Investigation of liquid-metal jet properties
  - Investigation of safety/radiation issues
  - Liquid-metal cooling of beamdump for fast extraction
  - 1 FTE
    3 year PostDoc
- **Handling, storage etc.** (K.H.Behr, GSI)
  - Manipulation and repairs of activated components
  - Hot cell and manipulators
  - Storage of activated parts
  - 1 FTE,
    Engineer

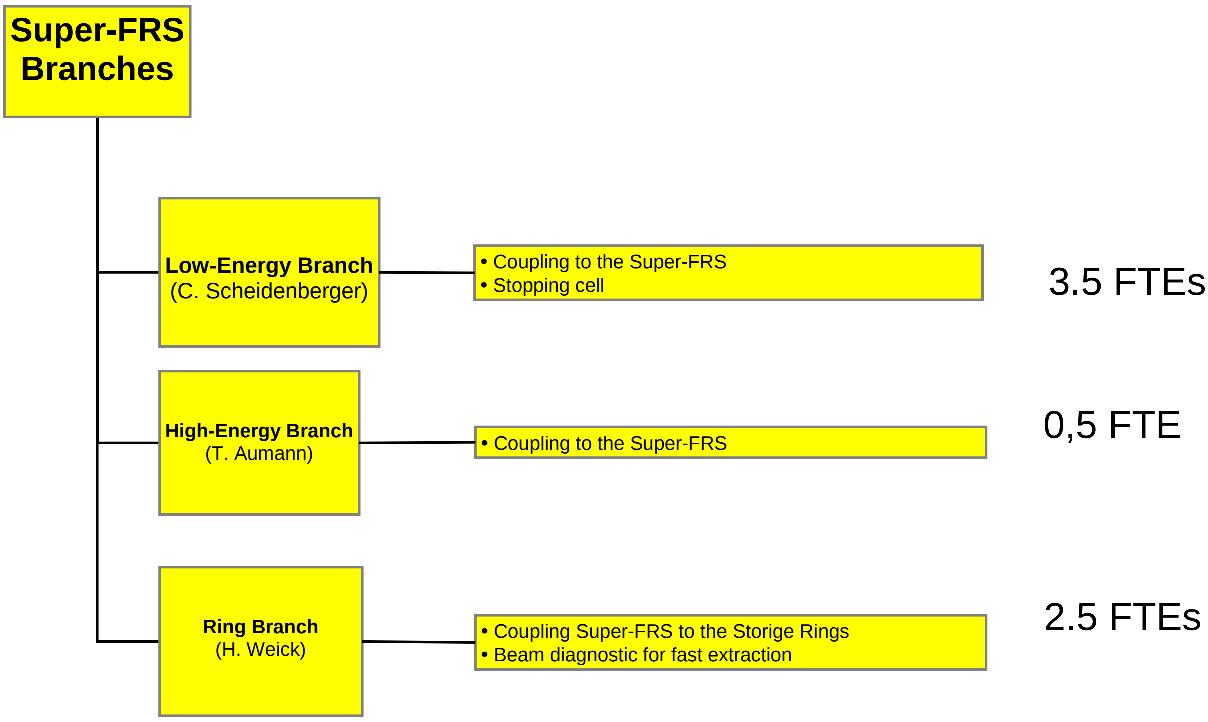

8 Relation to other projects

The Super-FRS will be used as a versatile magnetic system for experiments with exotic nuclei. Already presently the planned research activity with the separator is approved by 12 Letters of Intent.

9 Appendix

A.1 NUSTAR DAQ

The NUSTAR data acquisition (DAQ) concept tries to incorporate and deal with the changes that are related to the discontinuation of production and support of all CAMAC and FASTBUS modules, together with the much increasing number of channels in the different experiments. Dedicated front-end electronics boards are foreseen in most experiments for NUSTAR. The other main issue is to provide a maximum interoperability of the different setups of the NUSTAR facility as many parts of particular setups, detectors systems and their associated DAQ systems. As an example may serve the in-ring instrumentation of the NESR that will be used in parallel by the EXL and ELISe collaborations. The same holds for the combination Super-FRS instrumentation – R^3B setup, or gamma spectroscopy arrays in conjunction with reaction setups. As the communities overlap to a large extent it is favourable to come up with a combined DAQ framework that allows sharing expertise, thus saving manpower and running cost. The GSI MBS [70] system is an example for such a flexible DAQ scheme, that provides a generalized multi-processor environment, suitable for the readout, control and data storage of heterogeneous setups. The necessary extensions of the scheme have to be evaluated and integrated into the developing system by the NUSTAR DAQ group. A major part of this will be the integration of 'foreign' stand-alone DAQ systems or similarly the control and operation of various front-end electronics. System integration should be possible at different stages of the DAQ system.

(a) **"NUSTAR" DAQ systems:** It should be possible to couple different standalone "NUSTAR" DAQ systems, together in a simple way. Typically the individual DAQ systems are used to setup and debug detector groups or experiments. By foreseeing the necessary interconnects for triggers and control signals and by keeping the modularity of the system in mind while building local triggers and event buffer capabilities, such a scheme can be realized. The R^3B/CaveC setup together with the current FRS is an example where the necessary prerequisites are currently specified. Note, that different schemes of coupling might be used here: (i) the systems are synchronized with one common trigger (ii) the DAQ systems run standalone and are synchronized via timestamps (see section A.1.1 Time and trigger distribution systems).

(b) **Front-end electronics (FEE):** For the common NUSTAR DAQ system, specific front-end electronics together with its digitization part is seen as part of the detector. This has the advantage that all analogue signal processing is done by the working groups with the most experience on the particular detector system. Only the control, trigger and data flow will be specified as interface description by the common NUSTAR DAQ system. This includes the necessary trigger types to be implemented, like data, calibration and synchronization triggers together with a prescription how to lock the FEE to realize a clearly defined dead time of the total system. The timestamp-data interface has to be specified and slow control issues like version numbering, firmware revisions, software up/download from e.g. databases to particular FEE boards require R&D work. A first implementation for the digital interface that allows slow control and experiment data transfer from and to FEE boards already exists and is in use; the GTB-BUS a GSI development.

(c) **Inhomogeneous DAQ systems:** From our operating experience we know, that especially the large gamma arrays come with their own customized DAQ systems. As has been seen e.g. for the RISING [71] experiments at the FRS, a certain flexibility of the host (here the NUSTAR) DAQ system is mandatory to couple these systems together. The development and implementation of the TITRIS timestamp module together with the time-ordered writing to mass storage within the MBS framework is an example for such integration efforts.

Implementation: As a first step we want to implement within the years a standardized front-end electronics (e.g. for the R^3B/CAVEC) for fast signals. It will consist of a taquila [72] front-end board that has been developed for the upgrade of the FOPI experiment at GSI. These boards can be used to record 16 channels of time-signals, amplitude- or charge-signals at a moderate channel cost of about 50-60€. As interface to the detector additional FEE (e.g. [73]) boards are used, that are used to amplify, shape and split the signals prior to their input the digitizer board. Such a system can be thought of being already a replacement for a full e.g. NIM based pre-amplifier, discriminator and CAMAC/FASTBUS based digitizer chain. The taquila boards provide also a simple time stamp mechanism. We will study the behaviour of such a system within the next two years at the R^{3}B/CAVEC setup using the LAND neutron-detector readout as reference implementation. Further R&D steps will be accomplished to come to a fully operable FEE environment. The FEE is digitally attached via the GTB bus to a VME based processor board [74] that can be used to control the FEE readout process and to perform online data reduction (see Figure 64).

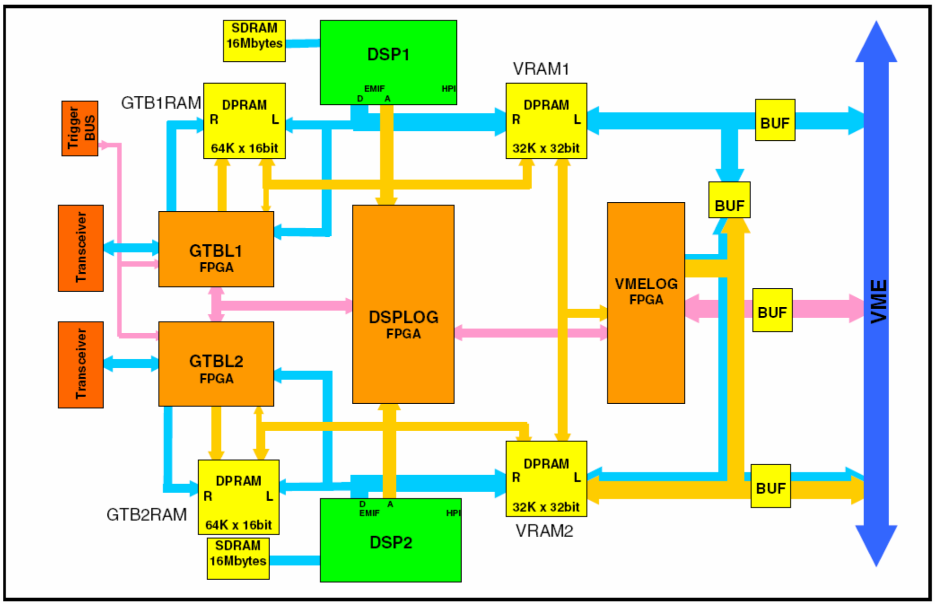

Figure 64: Block diagram of the VME based SAM3 processor board. Two TMS320C6711 digital signal processors running at 100 MHz are used. It is foreseen to provide this module's functionality within the framework of the NUSTAR DAQ system.

Known requests: Apart from the R^{3}B/FAIR experiment that will be the continuation of the R^{3}B/CAVEC experiment the EXL community has already come up with detailed requests to the NUSTAR DAQ group. The EXL front-end electronics which includes the ADC will have its own Time stamp & slow control facilities. The slow control facilities will allow a level of hard and software debugging. The slow control will allow the modification of e.g. the sub-trigger, choice of pre-amplifiers and amplifiers, the shaping, the gain, discriminators, sampling, ADC functions, calibration and test sequences, cable redundancy, high voltage, and bias settings. The structure required to manage the above should, is requested from the NUSTAR DAQ system. Apart from the control aspects, also the data collection chain from the digitized data has to be implemented, where the expected data rates for both experiments are approaching the 100 MBytes/sec limit.

Controls: We foresee two kinds of data from the experiments: event-wise data that is taken with the physics and control triggers and what we call slow control data, like scaler readouts, beam profiles and so on. These data are of interest for the distributed slow control system throughout the NUSTAR facility and the accelerator. For this example, profile data may be taken to generate a feedback loop in order to perform automatic beam steering, whereas scaler data can provide information on the sanity of the particular setups.

A.1.1 Time and trigger distribution systems

As can be seen from the above discussion one of the main infrastructures delivered by the NUSTAR DAQ framework will be a hierarchical time distribution system. Existing architectures for large scale time and trigger distribution systems are given e.g. by the TTC for LHC experiments [75], or the TCS [76,77] build for the COMPASS experiment, both at CERN. The Accelerator Division is currently working on the technical concept of the next generation timing system [78]. This activity was originally prompted by the requirement of the PHELIX experiment to synchronize a laser shot with the arriving pulse to a precision of 100 ps, thus the internal name "BuTiS" for 'Bunchphase Timing System'. This scope has of course widened, the objective is now to provide the timing reference for all FAIR accelerator components, and if there is interest, also the experiments. The current specifications call for a long term stability of 100 ps across the whole GSI site, and a timing jitter of well below 100 ps. The system will provide a campus reference for standard frequencies (current plan is 200 MHz and 10 MHz) and standard time (UTC) which will be derived from a GPS based reference. In addition, auxiliary information channels are foreseen which will provide for example triggers for specific accelerator events. Getting this performance over distances of up to 1 km has a price, the technologies and components used in BuTiS seem to be too expensive to be used in a local time distribution system of an experiment, where several end nodes have to be served over quite short distances. However, it seems prudent to use BuTiS as master clock/time reference for the local time distribution systems of experiments. This would also allow a more modular approach, using a local time distribution system per detector sub-system. This is of particular interest for experiments where parts of the setup are in different locations, like in many Super-FRS experiments.

Local time-stamps: A campus wide synchronisation method allows for common timestamps between different experiments. The common clock is not enough on its own for full synchronisation - one needs to be able to correlate particular clock edges with particular values of the timestamp counters in order to start from the same timestamp value everywhere. Existing local time distribution systems like e.g. the GSI TITRIS [79] modular, which is similar to the CENTRUM built by GANIL [80] and also the proposed AGATA GTS [81], have to be adapted to allow for the synchronization to the BUTiS clock with a defined phase. Different types of FEE will also provide their local clocks. One may consider the following scenarios:

a) Self-made timestamps, where a specification of the latency of the front-end trigger with respect to the timestamps is needed in order to be able to synchronize the particular data to the overall system. The latency can be automatically determined e.g. by using generated synchronization events from the host DAQ system to the particular timestamp generating system. Another question is how to couple local systems to BuTiS. One BuTiS receiver per local timestamping system might be too expensive it is a subject to further R&D whether an additional (experiment-wide) time distribution layer is desirable.
b) For the standardized NUSTAR DAQ one should consider to build a novel “Titris II” module in different form factors, to be used in VME crates or attached to the FEE, which can be coupled to the BuTiS system.

We can mainly base our studies on the already existing techniques, use of time-stamping followed by software filters and triggers which were developed for GREAT. Within GREAT these items are handled by the Metronome and its interface to the ADC cards. Within the next years we need to specify latencies for trigger decisions depending on the physics of the trigger, taking into account the limited pre-processing buffer depths, and their associated acceptance window. Here dedicated input from the different experiments is needed to come up with a generalized and flexible scheme.

A.1.2 Data collection and storage

Data collection and mass storage is another issue. If one deals with 10-100 Mbytes/sec data form the experiments at maximum as estimated for the EXL and R³B setups, the total data produced per day is in the order of 1-10 TBytes. This means, for the NUSTAR experiments we expect not more than 500TB/year of data. The requested band-width for data transfer is in accordance with the expected rates that can be transferred using standard network components.

The demand to run independent NUSTAR DAQ modules that can be combined in a flexible manner poses certain requirements to the transport layer in between the experiments and to the mass storage.

1. Standardized sub-event format; this is favourable in order to facilitate to event building from different data sources.
2. Flexible event builder combinations; one may consider to use different parts of the data stream at different locations to perform different tasks: mass storage; online analysis; slow control feedback.
3. Standardized event format; to be used for a common unpacking scheme for data analysis.

The NUSTAR DAQ system will provide the necessary data collection procedures for standard electronics module (e.g. VME) and collection from FE-boards that follow the conventions for the standardized digital interfaces (e.g. GTB). The necessary R&D work will be done in parallel to the various electronic developments in the NUSTAR community in close collaboration with the respective groups, co-ordinated by the DAQ responsible for the particular experiments.

A.1.3 Slow control and monitoring

The slow control requests for the NUSTAR DAQ system go two ways. First the sub-systems should provide certain information in order to be in the monitoring process of the total experiment specific combination of different DAQ systems at different locations. This functionality exceeds the implemented acquisition controls: a command dispatcher and log message facility, the sense, that also different online scalers providing dead-time and rates should be available. This implies also that there should be an extended way to be able to probe the actual configuration of the setup (this means an extended object with distances between the different parts of several 100 meters) including software revisions on the FE-boards and other related information. Probing means in this context, that the individual sub-systems provide information about the parameters and interlock conditions to be monitored. One may also think of status requests that return FPGA codes, hard- and software-revisions and related information.

The other way is the information that will be provided by the experiments DAQ and analysis stage to:

1. The accelerator; to allow e.g. automatic beam steering [82] like it is done at CERN PSB to continuously adjust experiments settings without manual interference.
2. The general slow controls of the experiment or setup, allowing to define interlock and

warning conditions.
3. Any other item not mentioned here that requires information of the experiments status extracted from the online data.

The advantage of such a scheme is that controls get their information from the different local systems so that the expertise is kept locally also.

The implementation of the above scheme will be an adaptive process, where tests of the method are and can be already done at existing setups, which will lead to a final design, also with the input of the locally existing controls group. The final specification will be provided in the Technical Design report.
The NUSTAR DAQ developments require continuous manpower efforts that should be provided by the collaborators of the individual experiments DAQ groups.

---

[1] H. Geissel et al, Nucl. Instr. and Meth. in Phys. Res B B70 (1992) 286.
[2] H. Geissel et al, Nucl. Instr. and Methods B 204 (2003) 71.
[3] K. L. Brown, SLAC 91, 1977.
[4] N. Iwasa et al., Nucl. Instr. Meth. B126 (1997) 284.
[5] H. Geissel et al., Nucl. Instr. and Methods A282 (1989) 247.
[6] N.A.Tahir et al., Phys. Rev. E 63 (2001) 036407-1.
[7] A. Yoshida private communication.
[8] G. Heidenreich, Proc. 20th ICFA Advanced Beam Dynamics Workshop on High Intensity and High Brightness Hadron Beams, ICFA-HB2002, Batavia Illinois, 2002, Proc. AIP 642 (2002) 122.
[9] Paul Müller Industrie Gmbh, Nürnberg, Germany, http://www.gmn.de
[10] http://www.sglcarbon.com/gs/profile/structure/
[11] Prophysik AG, Industriestrasse 416, 9491 Ruggell, Liechtenstein, E-Mail: prophysik@supra.net, tel: +4233771570, fax: +4233771575
[12] N. A. Tahir et al., “Calculations of a high-power production target for the Super-FRS using a fast extraction scheme”, http://www-land.gsi.de/r3b/EU-R3B/docu/rep02-a4.pdf
[13] J.A. Nolen et al., Nucl. Instr. Meth. B 204 (2003) 293.
[14] A. Fabich and J. Lettry, Nucl. Instr. Meth. A 503 (2003) 336; A. Fabich, PhD Thesis, 2002, TU Wien and CERN, CERN-THESIS-2002-038
[15] http://www.squ1.com/site.html
[16] http://www.webelements.com/index.html
[17] http://environmentalchemistry.com/yogi/periodic/#periodic%20table%20of%20elements
[18] F.E. Fortov et al., Nucl. Sci. Eng. 123 (1996) 169.
[19] D. J. Morrissey et al., Nucl. Instr. and Meth. B126 (1997) 316.
[20] T. Kubo, Nucl. Instr. and Meth. B204 (2003) 97.
[21] B. Sherril, Nucl. Instr. and Meth. B204 (2003) 765.
[22] Opera-2d and Opera-3d/TOSCA, Vector-Field, Ltd, Oxford, England.
[23] A. F. Zeller, J. C. DeKamp, D. Johnson, Adv. in Cryog. Eng., 43 (1998) 245 .
[24] K. Kusaka, T. Kubo, M. Mizoi, IEEE Trans. on Appl. Supercond. 14 (2004) 310.
[25] M. Sawan et al, Fusion Technology 10 (1986) 741.
[26] R. Reed and D. Evans, "Insulation systems for the Muon Colliders", unpublished report (2000).

[27] A. Harvey, S.A. Walker, IEEE Trans. Nucl. Sci. 16 (1969) 611.
[28] A. Zeller, private communication
[29] Principles of GIOS and COSY, H. Wollnik, B. Hartmann and M. Berz, AIP Conference Proceedings; ed. C. Eminhizer, 177 (1988) 74-85.
[30] N. Iwasa et al., Nucl. Instr. and Meth. in Phys Res. B126 (1997) 284.
[31] H. Iwase, K. Niita, and Takashi Nakamura, Journal of Nuclear Science and Technology, Vol. 39, No. 11, pp. 1142-1151, (2002).
[32] A. Fassò, A. Ferrari and P. R. Sala, "Electron-photon transport in FLUKA: status", Proceedings of the MonteCarlo 2000 Conference, Lisbon, October 23-26 2000, A. Kling, F. Barao, M. Nakagawa, L. Tavora, P. Vaz - eds., Springer-Verlag Berlin, p.159-164 (2001). and
A. Fassò, A. Ferrari, J. Ranft and P.R. Sala, "FLUKA: Status and Prospective for Hadronic Applications","Proceedings of the MonteCarlo 2000 Conference, Lisbon, October 23-26 2000, A. Kling, F. Barao, M. Nakagawa, L. Tavora, P. Vaz - eds., Springer-Verlag Berlin, p.955-960 (2001).
[33] http://www-linux.gsi.de/~weick/atima or as described as LS theory in
H. Geissel et al. Nucl. Instr. and Meth. in Phys. Res. B 195 (2002) 3-54.
[34] International Nuclear Safety Center, Materials and Properties Database, “Recommended Graphite, Enthalpy Increments and Heat Capacities”, Argonne Nat. Lab./US-DOE Internet documentation, http://www.ra.anl.gov/INSP/matprop
[35] C. Scheidenberger, Th. Stöhlker, W.E. Meyerhof, H. Geissel, P.H. Mokler, B. Blank, Nucl. Instr. and Meth. in Phys Res. B142 (1998) 441.
[36] ANSYS users manual, version 8.1, SAS IP, Inc. (2004).
[37] W. Kalbreier, W. Middelkoop, P. Sievers, CERN LAB II/BT/74-1, Geneva 1974.
[38] A. Abramov, S. Fillipov, P. Galkin, N. Galyaev, V. Garkusha, A. Kharlamov, E. Lomakin, F. Novoskoltsev, A. Ryabov, V. Zarucheisky, “Advanced Conceptual Design of the NuMI Hadron Beam Absorber Core”, NuMI-B-652, IHEP Protvino (2000).
http://beamdocs.fnal.gov/DocDB/0006/000673/001/numib652.pdf
[39] J. Boscary, M. Araki, J. Schlosser, M. Akiba, F. Escourbiac, Fusion Engineering Design 43 (1998) 147-171.
[40] J. Liu, R. Neumann, C. Trautmann, and C. Mueller, Physical Review B 64, 184115 (2001).
[41] F. Nickel, Nuclear Instruments and Methods, 195 (1982) 457.
[42] M. Argentini, R. Weinreich, “Measurement of radionuclide contents in activated graphite” PSI annual report 2000.
[43] N. Petoussi, M. Zankl, G. Fehrenbacher, G. Drexler, “Dose distributions in the ICRU sphere for monoenergetic photons and electrons and for ca. 800 radionuclides”, GSF-Bericht 7/93, GSF - Forschungszentrum für Umwelt und Gesundheit (1993).
[44] A.L. Conner, H.F. Atword, Elizabeth H. Plassmann, Phys. Rev A3, 539 (1970).
[45] H. Geissel et al., Nucl. Instr. Meth. A282, 247 (1989).
T. Schwab, GSI-Report GSI-91-10, Doctoral Thesis, University of Giessen (1990).
H. Geissel, Nucl. Instr. Meth. B204, 71 (2003).
[46] J. Weckenmann et al., GSI Report 90-13 (1990).
[47] M. Block et el., GSI Scientific Report 2003, 117 (2004).
[48] W. X. Huang et al., Europhys. Lett. 63 (5), 687-693 (2003).
[49] Methods of Beam Profile Measurements at High Current Hadron Accelerators, P. Forck, A. Peters, Conf. Proc of the 33rd ICFA ADVANCED BEAM DYNAMICS WORKSHOP on HIGH INTENSITY & HIGH BRIGHTNESS HADRON BEAMS 2004,

Bensheim, Germany, AIP Conference Proceedings, to be published

[50] The use of CVC-diamond for heavy-ion detection, E. Berderman, K. Blasche, P. Moritz, H. Stelzer, B. Voss, Diamond and Related Materials 10(2001)1770

[51] "New Developments in CVD Diamond Detector Applications", W. Adam and The RD42 Collaboration, EPJ 2003 (to be published).

[52] The RD42 Collaboration, Status Report 1999, CERN/LHCC 2000-011

[53] E. Berdermann et al., Nuclear Physics B (Proc. Suppl.) 78 (1999) 533-539

[54] R. Anne et al., Developement of Beam-Profile Monitors with Gas Amplification and Current Readout for the SIS Projectile-Fragment Separator, GSI Scientific Report (1990) p.257

[55] Herbert Stelzer, "Multiwire chambers with a two-stage gas amplification", Nucl. Instr. and Meth. **A310** (1991) 103.

[56] P. Forck, "Lecture Notes on Beam Instrumentation and Diagnostics", JUAS 2003, p. 77

[57] Current Transformers for GSI's keV/u to GeV/u ion beams – an overview, H. Reeg, N. Schneider, DIPAC 2001 Proceedings - ESRF, Grenoble

[58] A Cryogenic Current Comparator for the Absolute Measurement of nA Beams, A. Peters, H. Reeg, C.H. Schroeder, H. Koch, R. Neubert, W. Vodel, Conf. Proc. of the BEAM INSTRUMENTATION WORKSHOP 1998, Stanford, USA, Eds. R.O. Hettel, S.R. Smith, C.A.; Jennifer D. Masek, AIP Conference Proceedings Volume **451**

[59] B. Jurado, K.-H. Schmidt, K.-H. Behr, 'Application of a secondary-electron transmission monitor for high-precision intensity measurements of relativistic heavy-ion beams', Nucl. Instr. Meth. **A 483** (2002) 603.

[60] NoRHDia is a I3HP-Joint Research Activity, supported by the European Commission

[61] P. Adrich, et al, GSI Scientific Report 2003, GSI Report 2004-1, (2004) 26

[62] M. Pfützner et al., Nucl. Instr. and Meth. in Phys. Res. B86 (1994) 213.

[63] S. Agosteo and G. Fehrenbacher and M. Silari, Attenuation curves in concrete of neutrons from 1 GeV/u C and U ions on a Fe target for the shielding design of RIB in-flight facilities, Nucl. Instr. and Meth. B, (2004), Vol 226, pp 231-242.

[64] K. Gunzert-Marx, Nachweis leichter Fragmente aus Schwerionenreaktionen mit einem BaF2-Teleskop-Detektor, Ph.D.-work, Technical University Darmstadt, Germany (2004).

[65] M.V. Ricciardi, H. Weick, M.Winkler, private communication, (2003).

[66] J.-J. Gaimard and K.-H. Schmidt, Monte Carlo type nuclear reaction code, a modern version of the abrasion-ablation model, Nuclear Physics A, 531 (2003) 709.

[67] E. Hanelt and K.-H. Schmidt, Nucl. Instr. and Meth in Phys. Res. A 321 (1992) 434.

[68] J. Wie, J. Beebe-Wang, M. Blaskiewicz, P. Cameron, G. Danby, C.J. Gardner, J. Jackson, Y.Y. Lee, H. Ludewig, N. Malitsky, D. Raparia, N. Tsoupas, W.T. Wenig, S.Y. Zhang, "Beam-loss driven design optimization for the spallation neutron source (SNS) ring", in Proceedings of the 1999 Particle Accelerators Conference, New York, p.3185.

[69] E. Mustafin, I. Hofmann, H. Weick, Nucl. Instr. and Meth in Phys. Res. A 501 (2003) 553.

[70] The New data Acquisition System at GSI, H.G. Essel, J. Hoffmann, N. Kurz, R.S. Mayer, W. Ott, D. Schall, IEEE Trans. Nucl. Sci. **43** (1996), 132; The General Purpose Data Acquisition System MBS, H.G. Essel, N.Kurz, IEEE Trans. Nucl. Sci. **47** (2000), 337

[71] J. Hoffmann and N. Kurz, RISING Data Acquisition with MBS:Event Synchronization with Time Stamp Modules, GSI Scientific Report, p. 224.,2002

[72] A New TAC Based Multi Channel Front-End Electronics for TOF Experiments with Very High Time Resolution, K.Koch, H.Hardel, R.Schulze, E.Badura, J.Hoffmann (GSI), IEEE

Conf Proc. Nucl. Sci. Symp., Med. Im. Conf., Symp. Nucl. Power Sys. and 14th Int. Workshop on Room Temp. Semic. X- and Gamma- Ray Det., Oct. 16-22, 2004, Rome, Italy, to be published

[73] FOPI-Collaboration, "Upgrading the FOPI detector system", GSI Scientific Report, p. 177, 1998; A.Schüttauf et. al., "Timing Resistive Plate Counters (RPC) in FOPI", GSI Scientific Report, p. 231, 2003

[74] Development of New Readout Processor SAM3, J.Hoffmann, W.Ott, GSI Scientific Report, p. 193, 2002

[75] http://ttc.web.cern.ch/TTC/intro.html

[76] I. Konorov at al., The trigger control system for the COMPASS Experiment. IEEE Nuclear Science Symposium Conference Record (2002)

[77] L. Schmitt et al., The DAQ of the COMPASS Experiment. IEEE Trans. Nucl. Sci. (2004)

[78] P.Moritz (P.Moritz@gsi.de), private Communication.

[79] GSI MBS V.43 release notes,http://www-linux.gsi.de/~mbs/v43/manual/gm_mbs_r.pdf

[80] CENTRUM specifications, http://nnsa.dl.ac.uk/documents/edoc421/edoc421.pdf

[81] http://agata.pd.infn.it/documents/week9152003/MarcoBellato.pdf

[82] 'INTELLIGENT' AUTOMATIC BEAM STEERING AND SHAPING, A. Jansson and M. Lindroos, CERN, Geneva, Switzerland, Proceedings of EPAC 2000 conference.